Master's thesis
Theoretical and Computational Methods

A Theoretical Introduction to Stimulated Resonant Inelastic X-ray Scattering up to the Quadrupole Order

Miika Rasola

September 17, 2020

Tutor: prof. Simo Huotari

Censors: prof. Simo Huotari
prof. Nina Rohringer

UNIVERSITY OF HELSINKI
Department of Physics

PL 64 (Gustaf Hällströmin katu 2)
00014 Helsingin Yliopisto

“I’m smart enough to know that I’m dumb.”

— Richard P. Feynman

HELSINGIN YLIOPISTO — HELSINGFORS UNIVERSITET — UNIVERSITY OF HELSINKI

Tiedekunta — Fakultet — Faculty	Laitos — Institution — Department
Faculty of Science	Department of Physics

Tekijä — Författare — Author
Miika Rasola

Työn nimi — Arbetets titel — Title
A Theoretical Introduction to Stimulated Resonant Inelastic X-ray Scattering up to the Quadrupole Order

Oppiaine — Läroämne — Subject
Theoretical and Computational Methods

Työn laji — Arbetets art — Level	Aika — Datum — Month and year	Sivumäärä — Sidoantal — Number of pages
Master's thesis	September 17, 2020	95 pages

Tiivistelmä — Referat — Abstract

Resonant inelastic X-ray scattering (RIXS) is one of the most powerful synchrotron based methods for attaining information of the electronic structure of materials. Novel ultra-brilliant X-ray sources, X-ray free electron lasers (XFEL), offer new intriguing possibilities beyond the traditional synchrotron based techniques facilitating the transition of X-ray spectroscopic methods to the nonlinear intensity regime. Such nonlinear phenomena are well known in the optical energy range, less so in X-ray energies. The transition of RIXS to the nonlinear region could have significant impact on X-ray based materials research by enabling more accurate measurements of previously observed transitions, allowing the detection of weakly coupled transitions on dilute samples and possibly uncovering completely unforeseen information or working as a platform for novel intricate methods of the future.

The nonlinear RIXS or stimulated RIXS (SRIXS) on XFEL has already been demonstrated in the simplest possible proof of concept case. In this work a comprehensive introduction to SRIXS is presented from a theoretical point of view starting from the very beginning, thus making it suitable for anyone with the basic understanding of quantum mechanics and spectroscopy. To start off, the principles of many body quantum mechanics are revised and the configuration interactions method for representing molecular states is introduced. No previous familiarity with X-ray matter interaction or RIXS is required as the molecular and interaction Hamiltonians are carefully derived, based on which a thorough analysis of the traditional RIXS theory is presented. In order to stay in touch with the real world, the basic experimental facts are recapped before moving on to SRIXS. First, an intuitive picture of the nonlinear process is presented shedding some light onto the term *stimulated* while introducing basic terminology and some X-ray pulse schemes along with futuristic theoretical examples of SRIXS experiments. After this, a careful derivation of the Maxwell-Liouville-von Neumann theory up to quadrupole order is presented for the first time ever. Finally, the chapter is concluded with a short analysis of the experimental status quo on XFELs and some speculation on possible transition metal samples where SRIXS in its current state could be applied to observe quadrupole transitions advancing the field remarkably.

Avainsanat — Nyckelord — Keywords
nonlinear X-ray spectroscopy, RIXS, Stimulated RIXS, XFEL, SASE

Säilytyspaikka — Förvaringsställe — Where deposited

Muita tietoja — övriga uppgifter — Additional information

Contents

1. Introduction

Since the discovery of X-rays in 1895 they have become one of the most important tools in materials research and in little more than hundred years the number of applications of X-rays has grown immensely. Medical imaging applications of X-rays were immediately discovered by Wilhelm Röntgen himself soon followed by the work of Max von Laue and the Braggs (father and son) showing unequivocal evidence on the nature of X-rays as electromagnetic radiation. They also showed that since the wavelength of X-rays is of the order of atomic structures it could be used to investigate matter on an atomic level. This was a gigantic leap in materials research. Even though the early X-ray tubes yielded many ground breaking results, they were unable to provide radiation for more complicated studies, since the radiation from an X-ray tube is isotropic and incoherent. Further, only few high intensity spectral peaks called characteristic lines were produced apart from the considerably weaker background produced by bremsstrahlung. The difficulty of tuning the characteristic lines and polarization, the lacking of coherence, high brilliance and the ability of producing extremely short pulses all drove the evolution towards a more powerful, versatile source. The shortcomings of an X-ray tube were finally overcome by synchrotron radiation sources, even though electron storage rings were initially solely built for particle accelerator purposes and the produced radiation was considered a nuisance. In the 1960's it was however realized that synchrotron radiation emitted by the bending magnets of the storage rings has a number of properties far supe-

rior compared to X-ray tubes – tunable wavelength, directed emission and a huge increase in brilliance. This ultimately lead to the paradigm changing development of synchrotron radiation sources. This further lead to the still ongoing development of various methods for investigating matter on an atomic scale utilizing synchrotron X-ray sources. A multitude of Nobel prizes for discoveries related to X-rays have been awarded after the very first Noble prize in physics in 1901 awarded to Wilhelm Röntgen for the discovery of X-rays [1]. This underlines the importance of X-ray based methods in numerous fields of natural sciences.

Similar to the development of the synchrotron radiation source we are witnessing the dawn of a new X-ray source – first X-ray free electron lasers (XFEL) are already operational and producing results [2–4]. XFELs are capable of producing ultra brilliant, ultra short X-ray pulses with laser-like properties. This enables new experimental methods unraveling electronic structure of matter down to electronic spacial and temporal scales [5, 6]. Because of extreme intensities, XFELs facilitate the transfer of nonlinear spectroscopic methods, well known in the optical regime [7], to the X-ray spectral domain. Many of these methods are time-resolved utilizing the ultra short pulses from XFELs. For instance x-ray spectroscopy [8–10], resonant inelastic x-ray scattering (RIXS) [11, 12] and photoelectron [13] or Auger spectroscopies [14] can all be time-resolved and are powerful complementary methods for deciphering structural and chemical dynamics. The transfer of nonlinear methods from the optical regime to the X-ray domain not only makes these methods even more powerful but can also reveal completely unforeseen phenomena. For example, dilute samples with naturally low scattering intensities often appear in biologically interesting settings and could benefit from such methods.

One extremely promising method for realizing nonlinear X-ray spectroscopy is stimulated resonant inelastic X-ray scattering (SRIXS) [5]. Due to the resonant enhancement, traditional RIXS is one of the most powerful tools for attaining infor-

mation on the valence electron structure of matter [15–18], therefore vivid research is going on in order to upgrade the method to the nonlinear regime utilizing the power of an XFEL. Multiple nonlinear pump and probe spectroscopy schemes have been theorized based on SRIXS: simulations give evidence on the possibility of initiating and probing valence electron packets [19], tracking charge transfer in molecules [20] and observing electron hole dynamics [21]. Several, even more complicated, nonlinear spectroscopic schemes related to RIXS have been theoretically transferred to the X-ray spectroscopic regime [6]. Vast array of theoretical and simulational examples is, however, not met with experimental verification as many of these schemes require rather elaborate X-ray multi-pulse constructions with controllable pulse duration, time-delay and spectral features. Even more complicated requirements, such as phase control between pulses, have also been proposed [22], but current XFELs cannot, however, fulfill such specifications, and thus, only the simplest imaginable single-pulse stimulated RIXS scheme on atomic neon has been demonstrated so far [23, 24]. Enormous potential of the proposed methods is, nevertheless, indisputable.

In order to render stimulated RIXS and other nonlinear spectroscopies from being novelties into useful tools, systematic theoretical and experimental work is required. An interesting following step would be to demonstrate SRIXS on transition metals following in the foot steps of stimulated X-ray emission spectroscopy in transition metals [25]. This work is motivated by these considerations and aims to give a solid, self-contained and thorough introduction into the theoretical aspects of stimulated RIXS. The work is directed to anyone interested in the theoretical considerations behind nonlinear X-ray spectroscopy but also traditional RIXS. Therefore it assumes a minimal previous knowledge of the field and gives a complete description starting from first principles. In order to guide the reader to the subject, a full theoretical treatment of the traditional RIXS, the Kramers-Heisenberg approach, is

presented. Indeed, the reader does not need to be familiar even with the traditional method. Another reason for representing Kramers-Heisenberg theory is to obtain a well known point of comparison for the new nonlinear theory. The theory describing SRIXS, Maxwell-Liouville-von Neumann theory, is derived carefully. Especially, we will derive the equations describing SRIXS including electric quadrupole transitions taking the first step on the road to demonstrating SRIXS in transition metals. This is noteworthy, because before SRIXS has only been considered up to the dipole order in simple atomic samples and quadrupole transitions can be of importance in transition metals. Utilizing the traditionally weak quadrupole allowed transitions acting as direct probes of the 3d or 4f orbitals, for example in the Ni 1s-3d and Ga 2p-4f transitions, RIXS could be enhanced considerably by a stimulated process. Expanding SRIXS to cover quadrupole transitions can have significant applications for instance in 3d transition metal investigations in biologically relevant samples, where the naturally weak quadrupole transition and dilute sample together yield poorly observable scattering intensities. In order to produce an illuminating example of stimulated quadrupole RIXS, we shall theoretically investigate a model scheme of 1s2p SRIXS where nd orbitals are probed by exciting 1s electrons. Even though the present work is mainly theoretical, experimental side is not forgotten either. We shall provide an overlook of the most important experimental aspects regarding both traditional and stimulated RIXS in order to give a wholesome picture of the field to the reader.

More specifically the current text is constructed as follows. In the second chapter we introduce standard quantum mechanical machinery for dealing with many-particle systems. The configuration interaction expansion will be one of our most valued tools. The third chapter introduces generalities of X-ray matter interaction, most importantly the interaction Hamiltonian used throughout the rest of the work. Dipole and quadrupole approximations are also derived here. The next, fourth,

chapter contains the derivation of the Kramers-Heisenberg theory interpreted in the light of single particle-hole transitions utilizing the configuration interaction series. The fifth chapter is devoted to stimulated RIXS, it will first give an intuitive picture before delving into the theoretical considerations finally completing the comprehensive description into a synopsis and interpretation of the main results. The final chapter concludes the work with an outlook into the future.

2. Principles of Many-body Quantum Mechanics

In this work we will solely be dealing with systems consisting of more than just one or two quantum mechanical particles. Generally, even classical many body systems are impossible to solve exactly, which is why it is inevitable to arrive at some complications on the way. There are, however, some methods for dealing with quantum mechanical many-body systems, and here we shall present two. First we will give a quick recap on occupation number representation leading the way to second quantization, both quite general principles of quantum field theory. After this we will introduce a powerful method for describing many-electron states in molecules and atoms called the configuration interaction method. This method is inherently compatible with the occupation number representation allowing for a useful description of the molecular states utilizing single-particle states called spin orbitals. In addition to the molecular ground state configuration interaction method enables handling excited states. Thus, it gives us the opportunity to interpret excitations in the light of the single-particle spin orbitals and their occupations.

Before delving right in, let us introduce the unit system to be utilized. In the atomic units the electron mass, unit charge, reduced Planck constant and the speed of light are given, respectively, $m_e = 1$, $|e| = 1$, $\hbar = 1$, $c = 1/\alpha$, where the fine structure constant is $\alpha = \frac{e^2}{\hbar c} \approx 1/137$. The rest of the units are derived accordingly.

2.1 Second quantization

When dealing with many-particle systems in quantum mechanics the standard method of writing the relevant equations in first quantization poses an inconvenience. The system of equations will have an explicit dependence on the particle number, which becomes particularly troublesome when the particle number changes during the processes being described. This problem is usually resolved by occupation number representation or second quantization [26, 27]. It is a powerful formalism, regularly used to describe many body quantum systems. Especially interesting for us are the applications in the field of quantum chemistry and matter-radiation interaction. Second quantization allows us to describe both electromagnetic radiation fields and electronic states under the same strategy, which turns out to be extremely useful when investigating the interactions between the two.

The occupation number representation for identical particles is constructed via the Hermitian conjugates creation and annihilation operators $\hat{b}_\mu^\dagger$ and $\hat{b}_\mu$ satisfying the commutation relations

$$[\hat{b}_\mu^\dagger, \hat{b}_\nu^\dagger] = [\hat{b}_\mu, \hat{b}_\nu] = 0, \qquad [\hat{b}_\mu^\dagger, \hat{b}_\nu] = \delta_{\mu,\nu} \tag{2.1.1}$$

for bosons and the anti-commutation relations

$$\{\hat{a}_\mu^\dagger, \hat{a}_\nu^\dagger\} = \{\hat{a}_\mu, \hat{a}_\nu\} = 0, \qquad \{\hat{a}_\mu^\dagger, \hat{a}_\nu\} = \delta_{\mu,\nu} \tag{2.1.2}$$

for fermions. In both cases the creation operator $\hat{a}_\mu^\dagger$ ($\hat{b}_\mu^\dagger$) creates a particle in the single particle state $|\mu\rangle$, and respectively the annihilation operator $\hat{a}_\mu$ ($\hat{b}_\mu$) annihilates a particle from the same state. Here the single index μ is thought to contain all the information about the state. In the following we use the fermionic operators, but the results apply for bosons also. The number operator $\hat{n}_\mu = \hat{a}_\mu^\dagger \hat{a}_\mu$ gives the number of particles in the state $|\mu\rangle$. Due to the anti-commutation relations we have $\hat{n}_\mu^2 = \hat{n}_\mu$ for fermions, which is to be understood as the Pauli exclusion principle.

The quantum state is now created separately for bosons or fermions by consecutive operations of the respective creation operator to the vacuum $|0\rangle$:

$$|\{n_\mu\}\rangle = |n_1 n_2 \cdots\rangle = \sqrt{\frac{1}{n_1! n_2! \cdots}} (\hat{a}_1^\dagger)^{n_1} (\hat{a}_2^\dagger)^{n_2} \cdots |0\rangle \,, \tag{2.1.3}$$

where one would replace $\hat{a}_\mu^\dagger$ with $\hat{b}_\mu^\dagger$ for a bosonic state. The vacuum satisfies $\hat{a}_\mu |0\rangle = 0$ and $\langle 0|0\rangle = 1$. Note that for fermions the number of particles in a state is always either 1 or 0, i.e. $n_\mu \in \{0, 1\}$, therefore the square root always equals unity in the fermionic case. One also notes that the fermionic state will be completely antisymmetric, as it should, due to the anti-commutation. The total number of particles in a state defined by 2.1.3 can be calculated as

$$\hat{N} = \sum_\mu \hat{n}_\mu. \tag{2.1.4}$$

We should be able to write any operator in the language of occupation number representation in order to calculate anything in it. This turns out to be relatively simple. Using the creation and annihilation operators $\hat{a}_\mu^\dagger$ and $\hat{a}_\mu$ any one-body operator $\hat{\mathcal{O}}^{(1)}$ can be written as a series:

$$\mathcal{O}_{occ}^{(1)} = \sum_{\mu\nu} \langle \mu | \, \hat{\mathcal{O}}^{(1)} \, | \nu \rangle \, \hat{a}_\mu^\dagger \hat{a}_\nu. \tag{2.1.5}$$

Similarly, a two-body operator $\hat{\mathcal{O}}^{(2)}$ is given as:

$$\mathcal{O}_{occ}^{(2)} = \sum_{\mu\mu'\nu\nu'} \mathcal{O}^{(2)}_{\mu\mu'\nu\nu'} \hat{a}_{\mu'}^\dagger \hat{a}_\mu^\dagger \hat{a}_\nu \hat{a}_{\nu'}, \tag{2.1.6}$$

where $\mathcal{O}^{(2)}_{\mu\mu'\nu\nu'} = \langle \mu\mu' | \, \hat{\mathcal{O}}^{(2)} \, | \nu\nu' \rangle$. The sums here extend over all the single-particle states, not just the occupied ones. In principle, an N-body operator can be written similarly, but there are very few situations when anything beyond two-body operator is needed.

We will now focus on the second quantization of fermions. Let us now define the second quantized field operators inspired by the occupation number representation:

$$\hat{\psi}^\dagger(\xi) = \sum_\mu \psi_\mu^*(\xi)\hat{a}_\mu^\dagger \qquad \text{and} \qquad \hat{\psi}(\xi) = \sum_\mu \psi_\mu(\xi)\hat{a}_\mu. \tag{2.1.7}$$

Here $\xi = (\boldsymbol{x}, \sigma)$ contains both spatial spin degrees of freedom. The operator $\hat{\psi}(\boldsymbol{x})$ annihilates a particle at $\boldsymbol{x}$ with spin σ, whereas the conjugate $\hat{\psi}^\dagger(\boldsymbol{x})$ creates one. The $\psi_\mu^*(\xi)$ and $\psi_\mu(\xi)$ are first quantization wave functions used as expansion coefficients. These field operators clearly satisfy the same commutation or anti-commutation relations as before. Written explicitly for fermions:

$$\left\{\hat{\psi}(\xi), \hat{\psi}(\xi')\right\} = \left\{\hat{\psi}^\dagger(\xi), \hat{\psi}^\dagger(\xi')\right\} = 0 \tag{2.1.8}$$

$$\left\{\hat{\psi}(\xi), \hat{\psi}^\dagger(\xi')\right\} = \delta(\xi - \xi') = \delta_{\sigma,\sigma'}\delta(\boldsymbol{x} - \boldsymbol{x}'). \tag{2.1.9}$$

We can define all the required first quantized operators in second quantization similarly as before:

$$\begin{aligned} \mathcal{O}_{sq}^{(1)} &= \int d^3\xi \hat{\psi}^\dagger(\xi)\hat{\mathcal{O}}^{(1)}(\xi)\hat{\psi}(\xi) \\ \mathcal{O}_{sq}^{(2)} &= \int d^3\xi \int d^3\xi' \hat{\psi}^\dagger(\xi)\hat{\psi}^\dagger(\xi')\hat{\mathcal{O}}^{(2)}(\xi,\xi')\hat{\psi}(\xi')\hat{\psi}(\xi). \end{aligned} \tag{2.1.10}$$

In this representation the number density operator is given by

$$\hat{n}(\xi) = \hat{\psi}^\dagger(\xi)\hat{\psi}(\xi). \tag{2.1.11}$$

Consequently, the number of particles is calculated as:

$$\hat{N} = \int d\xi \hat{\psi}^\dagger(\xi)\hat{\psi}(\xi). \tag{2.1.12}$$

When dealing with electrons the field operators 2.1.7 are often written in the spinor representation:

$$\hat{\psi}^\dagger(\boldsymbol{x}) = \begin{pmatrix} \hat{\psi}_{+1/2}^\dagger(\boldsymbol{x}) \\ \hat{\psi}_{-1/2}^\dagger(\boldsymbol{x}) \end{pmatrix} \qquad \text{and} \qquad \hat{\psi}(\boldsymbol{x}) = \begin{pmatrix} \hat{\psi}_{+1/2}(\boldsymbol{x}) \\ \hat{\psi}_{-1/2}(\boldsymbol{x}) \end{pmatrix}, \tag{2.1.13}$$

where the spin coordinate is moved to the sub index.

There are a couple of benefits using second quantization. Second quantization inherently allows using the same Hamiltonian for systems with different number of particles in them. This is the main reason for it being the de facto representation when handling many-body systems in the quantum regime. The number of particles is strictly a property of the system, not the Hamiltonian. Another useful derivative property is that second quantization forms an intrinsic foundation for the particle-hole formalism to be used in the future while discussing excitations.

It is noteworthy that these definitions and results are not trivial. It requires quite a bit more justification to prove them correct unequivocally. The underlying statement here is that any N-body wave function can be created by operating with N independent creation operators into a unique vacuum state. Even though not trivial, this is the standard method, and so, more involved presentation will be overlooked here.

2.2 Configuration interaction method

In this section we shall develop a powerful method for representing molecular quantum mechanical states. The configuration interaction (CI) [28] method will allow us to write molecular states using single particle spin orbitals which, in turn, enables the interpretation of our results in terms of single particle-hole transitions. Configuration interaction method can be written in second quantization right from the start yielding a suitable framework for many of our calculations. CI is a so called post Hartree-Fock method, as it aims for improving on the traditional Hartree-Fock approximation [29], and is suitable for a range of systems and produces relatively accurate results. In the full CI scheme one can, in principle, give an exact expression to an arbitrary many-particle molecular quantum state. However, as one can guess, this is not a theory of everything that makes many-particle quantum mechanics utterly blissful. As we will soon see, the expressions become computationally way too

intense in practice, and an approximation has to be implemented.

Consider an N-electron molecular system, described by the standard molecular Hamiltonian (see 3.1.10). We are interested in the quantum state of the electrons in the molecule under the Born-Oppenheimer approximation [30], so we shall only take the electronic part of the Hamiltonian. Let us begin our inspection with a ground state Slater determinant produced by some mean field approximation, for example the Hartree-Fock or Kohn-Sham method [27, 29]:

$$|\Phi_0\rangle = |\varphi_1\varphi_2\cdots\varphi_N\rangle\,. \tag{2.2.1}$$

The Slater determinant consists of N spin-orbitals $|\varphi_p\rangle$, where $p = (n_i, l_i, m_i, m_s)$ is a composite index containing all the information required to describe an electronic state. The spin orbitals are found by minimizing the expectation value $\langle\Phi_0|\hat{H}_{el}|\Phi_0\rangle$ using linear variational principle [29], where

$$\hat{H}_{el} = -\frac{1}{2}\sum_i \nabla_i^2 - \sum_{n,i}\frac{Z_n}{|\boldsymbol{x}_i - \boldsymbol{R}_n|} + \frac{1}{2}\sum_{i\neq j}\frac{1}{|\boldsymbol{x}_i - \boldsymbol{x}_j|} \tag{2.2.2}$$

is the electronic Hamiltonian describing electronic states within an atom. The electronic Hamiltonian is discussed more in 3.1.2. Minimizing the expectation value of the energy yields an infinite set of eigenequations for the spin orbitals:

$$\hat{h}\,|\varphi_p\rangle = \varepsilon_p\,|\varphi_p\rangle\,, \tag{2.2.3}$$

where $\hat{h}$ is the one electron mean field Hamiltonian. These equations could be for instance the Hartree-Fock or Kohn-Sham equations. The method for solving this set of equations is not of importance to our analysis, so let's just assume a solution. Solving them yields, in principle, an infinite set of orthonormal spin orbitals $\{|\varphi_p\rangle\}$, which would then span the Hilbert space of states. Computationally we are, however, forced to solve only a finite dimensional subspace of the whole infinite dimensional Hilbert space. Let the number of obtained spin orbitals thus be restricted to $2K$. The factor 2 is to remind that there are two spatially equivalent spin orbitals with

opposite spins when discussing electronic degrees of freedom, assuming Kohn-Sham or restricted Hartree-Fock method for solving the set. From the set of $2K$ spin orbitals $\{|\varphi_p\rangle\}$ we choose N with the lowest energies to be occupied in the ground state Slater determinant $|\Phi_0\rangle$. We then have a set of $2K-N$ spin orbitals with higher energies that remain unoccupied. These shall be called the virtual orbitals. Let us establish a labelling system for the different orbital sets. The occupied orbitals in $|\Phi_0\rangle$ shall be labelled with indices from the set $\{i, j, k, l, ..\}$, whereas the virtual orbitals shall be labelled by $\{a, b, c, d, ..\}$. Orbitals that are general, in the sense that they can fall into either of the categories, are labelled by $\{p, q, r, s, ..\}$.

The lowest order of approximation is to assume that the obtained ground state Slater determinant equals the exact molecular ground state $|\Psi_0\rangle$:

$$|\Psi_0\rangle \approx |\Phi_0\rangle = |\varphi_1\varphi_2\cdots\varphi_i\varphi_j\cdots\varphi_N\rangle\,. \tag{2.2.4}$$

In addition, the virtual spin orbitals can be used to form exited determinants. We replace one or more of the N lowest energy spin orbitals in $|\Phi_0\rangle$ with a virtual orbital to obtain a higher energy states:

$$|\Phi_i^a\rangle = |\varphi_1\varphi_2\cdots\varphi_a\varphi_j\cdots\varphi_N\rangle \qquad \text{singly excited,} \tag{2.2.5}$$

$$\left|\Phi_{ij}^{ab}\right\rangle = |\varphi_1\varphi_2\cdots\varphi_a\varphi_b\cdots\varphi_N\rangle \qquad \text{doubly excited,} \tag{2.2.6}$$

and so on. These are given as a reference to the ground state determinant $|\Phi_0\rangle$. In general, one can always expand an arbitrary completely antisymmetric function of N variables in the complete orthonormal basis of functions $\{\varphi_p\}$ as:

$$f(x_1, x_2, ..., x_N) = \sum_{i_1<i_2<\cdots<i_N} \alpha_{i_1 i_2\cdots i_N}\varphi_{i_1}\varphi_{i_2}\cdots\varphi_{i_N}. \tag{2.2.7}$$

The antisymmetry of the function f is applied by the conditions

$$\alpha_{i_1 i_2\cdots i_j i_k\cdots i_N} = -\alpha_{i_1 i_2\cdots i_k i_j\cdots i_N} \qquad \text{and} \qquad \alpha_{i_1 i_2\cdots i_j i_k\cdots i_N}\delta_{i_j i_k} = 0. \tag{2.2.8}$$

Applying this to the excited Slater determinants we can write an arbitrary exact

state of an N-electron molecular system as:

$$|\Psi\rangle = \alpha_0 |\Phi_0\rangle + \sum_{ia} \alpha_i^a |\Phi_i^a\rangle + \sum_{j<k,b<c} \alpha_{jk}^{bc} \left|\Phi_{jk}^{bc}\right\rangle + \cdots . \tag{2.2.9}$$

This is the configuration interaction expansion [28, 29]. Note, that when we say that any N-electron state can be written exactly in CI we are assuming an infinite, orthonormal set $\{|\varphi_p\rangle\}$. This gives the infinite set of N-electron determinants $\{|\Phi_0\rangle, |\Phi_i^a\rangle, \left|\Phi_{jk}^{bc}\right\rangle, ...\}$ used to write the state $|\Psi\rangle$ as a series expansion. As mentioned before, this is computationally rather impossible, and we are forced to work with a finite basis rendering the above representation to an approximation. With a finite set of $2K$ spin orbitals $\{|\varphi_p\rangle\}$ one can form $\binom{2K}{N}$ N-electron determinants. Using all of these in the expansion 2.2.9 is called full CI, even though it is not "full" in the sense of the infinite basis. Full CI is, however, exact in the one-electron subspace spanned by the $2K$ spin orbitals. Often one has to further approximate and truncate the full CI series. In fact, one can see that the amount of determinants large quite quickly along with growing number of spin orbitals and electrons. This stands to say that the CI is not a method that makes everything easy in regards of many-particle quantum mechanics. In our analytical calculations we will only use the first two terms in the expansion 2.2.9, which is often called the CI singles (CIS) theory as it only takes into account singly excited states in addition to the ground state.

As a final remark, let us note that CI is readily compatible with the occupation number representation of quantum mechanics [29]. We can take the fermionic ladder operators satisfying the anti-commutation relations:

$$\{\hat{c}_p, \hat{c}_q\} = \{\hat{c}_p^\dagger, \hat{c}_q^\dagger\} = 0, \qquad \{\hat{c}_p, \hat{c}_q^\dagger\} = \delta_{pq}, \tag{2.2.10}$$

and use these to create or annihilate electrons in spin orbitals:

$$\hat{c}_p^\dagger |0\rangle = |\varphi_p\rangle , \qquad \hat{c}_p |\varphi_p\rangle = |0\rangle . \tag{2.2.11}$$

Here we use the letter c to denote the operator instead of a since from now on we will be using a as an index abundantly. The vacuum state $|0\rangle$ is annihilated by $\hat{c}_p$, as always, and the indices here denote both spatial and spin degrees of freedom. Care has to be taken while performing the computations since the operators cannot operate outside of their respective index set. For instance, one cannot annihilate an electron in an orbital that is not occupied to begin with: $\hat{c}_a |\Phi_0\rangle = 0$. Now we may construct the ground state by operating with the creation operators consecutively:

$$|\Phi_0\rangle = |\varphi_1 \varphi_2 \cdots \varphi_N\rangle = \hat{c}_1^\dagger \hat{c}_2^\dagger \cdots \hat{c}_N^\dagger |0\rangle = \prod_{i=1}^{N} \hat{c}_i^\dagger |0\rangle . \tag{2.2.12}$$

We obtain the excited determinants just as easily:

$$|\Phi_i^a\rangle = \hat{c}_a^\dagger \hat{c}_i |\Phi_0\rangle = |\varphi_1 \varphi_2 \cdots \varphi_a \varphi_j \cdots \varphi_N\rangle . \tag{2.2.13}$$

It is evident that all of the determinants in the CI expansion 2.2.9 can be constructed in this manner. Further, one immediately notes that due to the anti-commutation relations the antisymmetry of the determinants is imminent. We can also write any operator in the occupation number representation by using the spin orbitals and their ladder operators. As an example the single particle Hamiltonian is written as

$$\hat{H} = \sum_{pq} \langle \varphi_p | \hat{h} | \varphi_q \rangle \hat{c}_p^\dagger \hat{c}_q = \sum_p \varepsilon_p \hat{c}_p^\dagger \hat{c}_p \tag{2.2.14}$$

yielding the expression

$$\hat{H} |\Phi_0\rangle = \left(\sum_p \varepsilon_p \right) |\Phi_0\rangle = E_0 |\Phi_0\rangle . \tag{2.2.15}$$

This is of course completely analogous to the occupation number representation introduced in 2.1. Now we just have three sets of ladder operators and consider the occupation of spin-orbitals instead of particles. In the following chapters we shall use the methods presented here abundantly.

3. Radiation-Matter Interaction

In this chapter we will lay out the grounds on which a vast number of methods probing the atomic and electronic structure of matter with X-rays is based on. For a start we make a remark about the ratio of the masses of electrons and nuclei in atoms. To a very good approximation, the X-rays only interact with the electrons in matter [31]. The ratio of the electron mass compared to the proton mass is of order $\sim 10^{-4}$, thus, the nucleus is simply too heavy, in comparison with the electron, to undergo significant oscillations under the high frequency electromagnetic field. Consequently, we will focus on describing the interaction of electrons with the field. In order to do this, we will utilize non-relativistic quantum electrodynamics. As long as the electron mass (511 keV) is large compared to the photon energy, relativistic effects are negligible, further, relativistic electronic structure effects, such as spin-orbit coupling, are ignored here. A covariant theory is not required, so a Hamiltonian approach will be utilized. We shall begin with the minimal coupling Hamiltonian and extend that to the full Hamiltonian describing all the processes in the interaction of X-rays and matter. This Hamiltonian will serve as a foundation to the rest of the work, therefore it is educational to inspect its origins, but most importantly, the interaction Hamiltonian derived here will be the theoretical starting point of all our future computations.

3.1 The Matter-field Hamiltonian

In order to describe complicated quantum mechanical systems perturbation theory [26] is often utilized: The idea is to describe a complicated system as an expansion of a simpler system. Especially in the time-dependent perturbation theory one divides the system into a time-independent and time-dependent contributions. Thus, using perturbation theory requires the Hamiltonian in a form where the dominant contribution is included in the unperturbed time-independent Hamiltonian $\hat{H}_0$, and the perturbation is described by the time-dependent interaction Hamiltonian $\hat{H}_{int}(t)$:

$$\hat{H} = \hat{H}_0 + \hat{H}_{int}(t). \tag{3.1.1}$$

In the following we shall explicitly produce both parts of the above Hamiltonian along with justification or derivation. The starting point will be the minimal coupling Hamiltonian of a single charged particle:

$$\begin{aligned} \hat{h}_i &= \frac{\left[\hat{\boldsymbol{p}}_i - \alpha q_i \boldsymbol{A}(\boldsymbol{x}_i)\right]^2}{2m_i} + q_i \Phi(\boldsymbol{x}_i) \\ &= \frac{\hat{\boldsymbol{p}}_i^2 + [\alpha q_i \boldsymbol{A}(\boldsymbol{x}_i)]^2 - \alpha q_i [\hat{\boldsymbol{p}}_i \cdot \boldsymbol{A}(\boldsymbol{x}_i) + \boldsymbol{A}(\boldsymbol{x}_i) \cdot \hat{\boldsymbol{p}}_i]}{2m_i} + q_i \Phi(\boldsymbol{x}_i), \end{aligned} \tag{3.1.2}$$

where $\hat{\boldsymbol{p}}_i$, q_i, $\boldsymbol{x}_i$ and m_i are the momentum, charge, position and mass of the i'th particle, respectively. The terms independent of the vector potential $\boldsymbol{A}$ will constitute the molecular Hamiltonian covering the standard interactions in atomic matter. The middle terms will form the interaction Hamiltonian $\hat{H}_{int}$ in 3.1.1 that accounts for the interaction of the matter with the external field. The minimal coupling Hamiltonian is obtained using the principle of minimal coupling. Mathematically the statement of the principle is simply

$$\hat{\boldsymbol{p}} \to \hat{\boldsymbol{p}} - q\boldsymbol{A}. \tag{3.1.3}$$

The vector potential $\boldsymbol{A}(\boldsymbol{x}_i)$ and the scalar potential $\Phi(\boldsymbol{x}_i)$ are related to the electric

and magnetic fields in the standard way:

$$\begin{aligned} \boldsymbol{E} &= -\nabla\Phi - \alpha\frac{\partial \boldsymbol{A}}{\partial t} \\ \boldsymbol{B} &= \nabla \times \boldsymbol{A}. \end{aligned} \tag{3.1.4}$$

Before moving forward we are going to discuss about gauge fixing. Fixing a gauge can greatly simplify forthcoming calculations.

3.1.1 Coulomb Gauge

Coulomb gauge [32] is one of the most commonly used gauges in quantum chemistry and condensed matter physics. Historically, electromagnetic radiation was first quantized in Coulomb gauge. There is a major advantage in using Coulomb gauge. A natural Hamiltonian formulation of the equations of motion of the electromagnetic field is attained using Coulomb gauge. Thus, as we are seeking for a Hamiltonian description, we shall use Coulomb gauge throughout this work. The gauge condition is, quite simply,

$$\nabla \cdot \boldsymbol{A} = 0. \tag{3.1.5}$$

By Maxwell's laws, magnetic field is always purely transverse, $\nabla \cdot \boldsymbol{B} = 0$. Adapting the Coulomb gauge separates the electric field in longitudinal and transverse parts:

$$\boldsymbol{E} = \boldsymbol{E}^{\parallel} + \boldsymbol{E}^{\perp}, \tag{3.1.6}$$

where, using 3.1.4 and standard vector calculus identities:

$$\begin{aligned} \boldsymbol{E}^{\parallel} &= -\nabla\boldsymbol{\Phi}, \qquad & \nabla \times \boldsymbol{E}^{\parallel} &= \boldsymbol{0} \\ \boldsymbol{E}^{\perp} &= -\alpha\frac{\partial \boldsymbol{A}}{\partial t}, \qquad & \nabla \cdot \boldsymbol{E}^{\perp} &= 0. \end{aligned} \tag{3.1.7}$$

We can quickly verify that the gauge produces the standard Coulomb electrostatic potential. We use Gauss's law and plug in 3.1.6 and 3.1.7 in order to

obtain

$$\nabla \cdot \boldsymbol{E} = \nabla \cdot \boldsymbol{E}^{\parallel} = -\nabla^2 \Phi = 4\pi \sum_i q_i \delta(\boldsymbol{x} - \boldsymbol{x}_i). \tag{3.1.8}$$

Solving for Φ yields the standard result

$$\Phi = 4\pi \sum_i \frac{q_i}{|\boldsymbol{x} - \boldsymbol{x}_i|}. \tag{3.1.9}$$

Applying this result on 3.1.2 and taking a sum over all relevant particles we are able to write down the Hamiltonian describing internal interactions in matter. This is what is done in the following section.

Before moving on to the actual matter at hand, the Hamiltonian, let us address one drawback of the Coulomb gauge. As mentioned before, the gauge is not Lorentz covariant [33]. Thus, it is not used in modern covariant perturbation theory calculations in relativistic quantum field theory. A rather similar gauge, namely, Lorentz gauge $\partial_\mu A^\mu = 0$, is often the choice in relativistic calculations. If one is to make a Lorentz transformation into a new inertial frame, an additional gauge transformation needs to be performed in order to retain Coulomb gauge condition. These properties of the Coulomb gauge will, however, not be a hindrance to us, as we will ignore all relativistic effects.

3.1.2 The Molecular Hamiltonian

The standard molecular Hamiltonian describes the motion of the nuclei as well as the Coulomb interaction between the nuclei. Furthermore, it accounts for the momenta and the interactions of the electrons, both, with the nuclei and the other electrons. The molecular Hamiltonian describes atomic matter in the absence of any external fields: $\boldsymbol{A} = 0$. We will write the Hamiltonian in the standard for as a sum of three terms [31]:

$$\hat{H}_{mol} = \hat{T}_N + \hat{V}_{NN} + \hat{H}_{el}. \tag{3.1.10}$$

These three terms follow almost trivially from the terms that are independent of $\boldsymbol{A}$ (first and last term) in the Hamiltonian 3.1.2 by plugging in the Coulomb electrostatic potential 3.1.9 to the last term in the Hamiltonian. The first term in 3.1.10 is the kinetic energy of the nuclei, given by

$$\hat{T}_N = \sum_n \frac{\hat{\boldsymbol{p}}_n^2}{2M_n} = -\frac{1}{2}\sum_n \frac{\nabla_n^2}{M_n}, \tag{3.1.11}$$

whereas the second term describes the nucleus-nucleus Coulomb interaction:

$$\hat{V}_{NN} = \sum_{n<n'} \frac{Z_n Z_{n'}}{|\boldsymbol{R}_n - \boldsymbol{R}_{n'}|}. \tag{3.1.12}$$

Here M_n, Z_n and $\boldsymbol{R}_n$ are the mass, atomic number and position of the n'th nucleus, respectively.

The electronic Hamiltonian $\hat{H}_{el}$ collects the kinetic energy terms of the electrons as well as the nucleus-electron and electron-electron Coulomb interactions. Explicitly, in respective order, it is written as:

$$\hat{H}_{el} = -\frac{1}{2}\sum_i \nabla_i^2 - \sum_{n,i} \frac{Z_n}{|\boldsymbol{x}_i - \boldsymbol{R}_n|} + \frac{1}{2}\sum_{i\neq j} \frac{1}{|\boldsymbol{x}_i - \boldsymbol{x}_j|}. \tag{3.1.13}$$

The sums extend over all the electrons i, j and the nuclei n. In addition to previous definitions, $\boldsymbol{x}_i$ is the position of the i'th electron. The Hamiltonian 3.1.10 is exact apart from relativistic effects and small corrections, such as spin-orbit coupling. Ignoring spin-dependent terms is a standard approximation as they are $\hbar/mc^2$ smaller than the rest of the terms [34]. Note, that while 3.1.2 depends on mass and charge, in this subsection and from here on the electron charge and mass are, respectively $|q_e| = 1$ and $m_e = 1$.

3.1.3 The Interaction Hamiltonian

In the previous subsection we expanded the terms independent of the vector potential in the Hamiltonian 3.1.2 into their final form. Now we are going to deal with

the middle terms in 3.1.2 that do depend on the vector potential $\boldsymbol{A}$. First, let us modify the $\hat{\boldsymbol{p}}_i \cdot \boldsymbol{A}(\boldsymbol{x}_i)$ terms. We have:

$$\begin{aligned}(\hat{\boldsymbol{p}}_i \cdot \boldsymbol{A}(\boldsymbol{x}_i) + \boldsymbol{A}(\boldsymbol{x}_i) \cdot \hat{\boldsymbol{p}}_i) &= -i\left(\nabla \cdot \boldsymbol{A}(\boldsymbol{x}_i) + \boldsymbol{A}(\boldsymbol{x}_i) \cdot \nabla\right) \\ &= -i\left[(\nabla \cdot \boldsymbol{A}(\boldsymbol{x}_i)) + \boldsymbol{A}(\boldsymbol{x}_i) \cdot \nabla + \boldsymbol{A}(\boldsymbol{x}_i) \cdot \nabla\right] \\ &= -2i(\boldsymbol{A}(\boldsymbol{x}_i) \cdot \nabla).\end{aligned} \tag{3.1.14}$$

Here we note that, as a Hamiltonian is an operator, we can imagine it operating on some state and then use the product rule for divergence on the first term. Under the Coulomb gauge condition 3.1.5 the first term in the second line vanishes. Plugging this result back into 3.1.2 and taking the sum over all N_{el} electrons we obtain the interaction Hamiltonian [31, 35]:

$$H_{int} = \sum_{i}^{N_{el}} \left(\frac{\alpha^2}{2} \boldsymbol{A}^2(\boldsymbol{x}_i) - i\alpha \boldsymbol{A}(\boldsymbol{x}_i) \cdot \nabla_i \right). \tag{3.1.15}$$

The sum above extends over all the electrons in the system. As discussed before, the interactions of the nuclei with the external field are excluded. This approximation is justified by the vastly larger mass of the nucleus compared to an electron and the high frequency of the radiation used. The nuclei will simply not "move" anywhere near as much as the electrons.

The first term on the right hand side of 3.1.15 is commonly referred to as the $\boldsymbol{A}^2$ term whereas the second is called the $\boldsymbol{p} \cdot \boldsymbol{A}$ term. The $\boldsymbol{A}^2$ term is often ignored in visible spectrum range [35], but in the X-ray region it is responsible for elastic Thomson and inelastic Compton scattering [36]. For us the second term is more interesting as it the dominating term in resonant scattering. Therefore, through out the rest of this work we shall mainly direct our interest to the $\boldsymbol{p} \cdot \boldsymbol{A}$ term. Further, it is accountable for photoabsorption [37] and anomalous scattering [38] but these effects are not in the scope of this work.

Looking back at the beginning of this section, we now have the interaction part of the Hamiltonian 3.1.1, as defined above. The molecular Hamiltonian 3.1.10

constitutes to the unperturbed part $\hat{H}_0$ in 3.1.1. We still require a Hamiltonian description of the free electromagnetic field towards the full unperturbed Hamiltonian of the system at hand.

3.1.4 The Electromagnetic Field Hamiltonian

In quantum electrodynamics the electromagnetic field is quantized. Here we shall not present a detailed derivation of the quantized electromagnetic field, but rather collect the needed results in a concise manner. In the Coulomb gauge the electric field is divided into longitudinal and transverse parts given by 3.1.7. In free space there are no sources of electric field. Thus, in the case of electromagnetic radiation, the electric field is purely transverse, $\nabla \cdot \boldsymbol{E} = \nabla \cdot \boldsymbol{E}^{\perp} = 0$. Classically, the energy of a free electromagnetic field is now given as:

$$\begin{aligned} E_{EM} &= \frac{1}{8\pi} \int d^3x \left(\boldsymbol{E}^2 + \boldsymbol{B}^2 \right) \\ &= \frac{1}{8\pi} \int d^3x \left(\alpha^2 \left[\frac{\partial \boldsymbol{A}}{\partial t} \right]^2 + [\nabla \times \boldsymbol{A}]^2 \right). \end{aligned} \tag{3.1.16}$$

Fourier expanding the vector potential $\boldsymbol{A}$ in plane waves is the standard way of proceeding. This expansion can be found in many advanced quantum mechanics or quantum field theory books (e.g. [26, 39]):

$$\hat{\boldsymbol{A}}(\boldsymbol{x}) = \sum_{\boldsymbol{k},\lambda} \sqrt{\frac{2\pi}{V \omega_{\boldsymbol{k}} \alpha^2}} \left(\hat{a}_{\boldsymbol{k},\lambda} \boldsymbol{\epsilon}_{\boldsymbol{k},\lambda} e^{i\boldsymbol{k}\cdot\boldsymbol{x}} + \hat{a}^{\dagger}_{\boldsymbol{k},\lambda} \boldsymbol{\epsilon}^{*}_{\boldsymbol{k},\lambda} e^{-i\boldsymbol{k}\cdot\boldsymbol{x}} \right). \tag{3.1.17}$$

The expansion is carried out in a box volume V. The polarization vectors $\boldsymbol{\epsilon}_{\boldsymbol{k},\lambda}$ satisfy $\boldsymbol{k}\cdot\boldsymbol{\epsilon}_{\boldsymbol{k},\lambda} = 0$ and $\boldsymbol{\epsilon}^{*}_{\boldsymbol{k},\lambda}\cdot\boldsymbol{\epsilon}_{\boldsymbol{k},\alpha} = \delta_{\lambda,\alpha}$. These conditions are nothing but the Coulomb gauge condition in momentum space. The wave vector $\boldsymbol{k}$ and the frequency $\omega_{\boldsymbol{k}} = |\boldsymbol{k}|/\alpha$ are standard. Polarization λ can have values 1 or 2. This expression is already quantized by replacing the expansion coefficients of the Fourier expansion with the bosonic ladder operators $\hat{a}_{\boldsymbol{k},\lambda}$ and $\hat{a}^{\dagger}_{\boldsymbol{k},\lambda}$ from the section 2.1. The raising operator $\hat{a}^{\dagger}_{\boldsymbol{k},\lambda}$ creates a photon in the mode $(\boldsymbol{k}, \lambda)$, whereas the lowering operator $\hat{a}_{\boldsymbol{k},\lambda}$ annihilates

a photon, respectively. Electromagnetic radiation will be described as a collections of harmonic oscillators.

By plugging the Fourier expanded vector potential into 3.1.16 and applying some algebra one arrives at

$$\hat{H}_{EM} = \sum_{\boldsymbol{k},\lambda} \omega_{\boldsymbol{k}} \hat{a}^{\dagger}_{\boldsymbol{k},\lambda} \hat{a}_{\boldsymbol{k},\lambda}. \tag{3.1.18}$$

The vacuum energy term $\omega_{\boldsymbol{k}}/2$ is ignored here. We can always renormalize the theory as we are only able to observe the changes in energy anyhow [31].

We now have all the pieces of the puzzle. We can explicitly write down the full Hamiltonian capturing all relevant physical phenomena occurring in matter-radiation interaction. The Hamiltonian, written in the format suitable for perturbation theory, is

$$\hat{H} = \underbrace{\hat{H}_{mol} + \hat{H}_{EM}}_{=\hat{H}_0} + \hat{H}_{int}. \tag{3.1.19}$$

Next, we shall use this Hamiltonian to derive the scattering cross section of the RIXS process. In order to do this we will first adopt a scheme called second quantization.

Using the results from section 2.1 we will be able to write down the electronic Hamiltonian 3.1.13 in second quantization:

$$\begin{aligned} \hat{H}_{el} = \int d^3x \hat{\psi}^{\dagger}(\boldsymbol{x}) \left[-\frac{1}{2}\nabla^2 - \sum_n \frac{Z_n}{|\boldsymbol{x} - \boldsymbol{R}_n|} \right] \hat{\psi}(\boldsymbol{x}) \\ + \frac{1}{2} \int d^3x \int d^3x' \frac{\hat{\psi}^{\dagger}(\boldsymbol{x}) \hat{\psi}^{\dagger}(\boldsymbol{x}') \hat{\psi}(\boldsymbol{x}') \hat{\psi}(\boldsymbol{x})}{|\boldsymbol{x} - \boldsymbol{x}'|}. \end{aligned} \tag{3.1.20}$$

We will also transfer the interaction Hamiltonian 3.1.15 into the second quantized form:

$$\hat{H}_{int} = -i\alpha \int d^3x \hat{\psi}^{\dagger}(\boldsymbol{x}) \left[\hat{\boldsymbol{A}}(\boldsymbol{x}) \cdot \nabla \right] \hat{\psi}(\boldsymbol{x}) + \frac{\alpha^2}{2} \int d^3x \hat{\psi}^{\dagger}(\boldsymbol{x}) \hat{\boldsymbol{A}}^2(\boldsymbol{x}) \hat{\psi}(\boldsymbol{x}). \tag{3.1.21}$$

Note that here we are using the spinor representation 2.1.13.

We now have the Hamiltonian assembled and written in the modern quantum field theoretical setting of second quantization. We can now move on to derive

the Kramers-Heisenberg formula giving the traditional explanation for the RIXS process.

3.2 Dipole and quadrupole approximations

As we will see, matrix elements of the form $\langle\Psi|\,\hat{H}_{int}\,|\Phi\rangle$, with $\langle\Psi|$ defined as the final state and $|\Phi\rangle$ as the initial state, arise when calculating observables in perturbation theory. The interaction Hamiltonian $\hat{H}_{int}$ contains an exponential operator that appears in the vector potential 3.1.17. This exponential coupled to other operators renders an exact calculation of the matrix elements rather impossible, which is why a further approximation has to be implemented. Let us derive an approximation for the matrix elements and argue that, consequently, the interaction Hamiltonian can be written in a simpler form. We will work in first quantization and look at the $\boldsymbol{p}\cdot\boldsymbol{A}$ term in 3.1.15. Further, we shall focus on single particle-hole states, thus, omitting the $\boldsymbol{A}^2$ term and plugging in the vector potential 3.1.17 the interaction Hamiltonian reads:

$$\hat{H}_{int}(\boldsymbol{x},t) = -i\alpha\sum_{\boldsymbol{k},\lambda}\sqrt{\frac{2\pi}{V\omega_{\boldsymbol{k}}\alpha^2}}\left(\hat{a}_{\boldsymbol{k},\lambda}\boldsymbol{\epsilon}_{\boldsymbol{k},\lambda}e^{-i(\omega_{\boldsymbol{k}}t-\boldsymbol{k}\cdot\boldsymbol{x})}+\hat{a}^{\dagger}_{\boldsymbol{k},\lambda}\boldsymbol{\epsilon}^{*}_{\boldsymbol{k},\lambda}e^{i(\omega_{\boldsymbol{k}}t-\boldsymbol{k}\cdot\boldsymbol{x})}\right)\cdot\nabla. \quad (3.2.1)$$

The position dependent exponent is Taylor expanded in the usual way:

$$e^{\pm i\boldsymbol{k}\cdot\boldsymbol{x}} = 1 \pm i\boldsymbol{k}\cdot\boldsymbol{x} + \frac{(\pm i\boldsymbol{k}\cdot\boldsymbol{x})^2}{2} + \cdots \quad (3.2.2)$$

Plugging in the first two terms of this expansion, the Hamiltonian is separated into the dipole and quadrupole contributions, respectively:

$$\begin{aligned}\hat{H}_{int}(\boldsymbol{x},t) \approx& -i\alpha\sum_{\boldsymbol{k},\lambda}\sqrt{\frac{2\pi}{V\omega_{\boldsymbol{k}}\alpha^2}}\left(\hat{a}_{\boldsymbol{k},\lambda}\boldsymbol{\epsilon}_{\boldsymbol{k},\lambda}e^{-i\omega_{\boldsymbol{k}}t}+\hat{a}^{\dagger}_{\boldsymbol{k},\lambda}\boldsymbol{\epsilon}^{*}_{\boldsymbol{k},\lambda}e^{i\omega_{\boldsymbol{k}}t}\right)\cdot\nabla \\ &+\alpha\sum_{\boldsymbol{k},\lambda}\sqrt{\frac{2\pi}{V\omega_{\boldsymbol{k}}\alpha^2}}(\boldsymbol{k}\cdot\boldsymbol{x})\left(\hat{a}_{\boldsymbol{k},\lambda}\boldsymbol{\epsilon}_{\boldsymbol{k},\lambda}\cdot\nabla e^{-i\omega_{\boldsymbol{k}}t}-\hat{a}^{\dagger}_{\boldsymbol{k},\lambda}\boldsymbol{\epsilon}^{*}_{\boldsymbol{k},\lambda}\cdot\nabla e^{i\omega_{\boldsymbol{k}}t}\right) \quad (3.2.3)\\ =&H_D(t)+H_Q(\boldsymbol{x},t).\end{aligned}$$

Higher order terms are neglected here. A more general way of proceeding is the multipole expansion but as the scope of this work is restricted to the quadrupole transitions this approach is adequate [15].

In quantum mechanics the Hamiltonian is an operator corresponding to an observable. Due to this nature of quantum mechanics the Hamiltonian, as is, won't tell us anything, rather, we are interested in the expectation values or more generally the matrix elements of the Hamiltonian. In this work we are interested in resonant scattering events meaning that there are radiation induced transitions involved in the atoms of the sample. In order to calculate a scattering cross section, describing how the incoming radiation scatters from the sample, we must be able calculate transition amplitudes $\langle F|\,\hat{H}_{int}\,|I\rangle$ related to the probabilities observing radiation induced transitions between the initial state $|I\rangle$ and the final state $|F\rangle$ in the system. To this end, let us calculate the transition amplitudes of the approximate Hamiltonian we have in the hopes of simplifying the expression. Let us define product states describing the joint state of the atom or a molecule and the radiation field containing N photons:

$$|I\rangle = |\Psi_0\rangle\,|N_{\boldsymbol{k},\lambda}\rangle \qquad \text{and} \qquad |F\rangle = |\Psi_f\rangle\,|N_{\boldsymbol{k},\lambda}-1\rangle\,, \tag{3.2.4}$$

where the initial state $|I\rangle$ contains one more photon in the electromagnetic field than the final state $|F\rangle$. Therefore the transition from $|I\rangle$ to $|F\rangle$ is clearly related to photoabsorption and the opposite transition to photoemission. The matrix elements for photoabsorption are

$$\begin{aligned}\langle F|\,\hat{H}_{int}\,|I\rangle =& \langle F|\,\hat{H}_D\,|I\rangle + \langle F|\,\hat{H}_Q\,|I\rangle \\ =& \alpha\sqrt{\frac{2\pi N_{\boldsymbol{k},\lambda}}{V\omega_{\boldsymbol{k}}\alpha^2}}\,\langle\Psi_f|\,\boldsymbol{\epsilon}_{\boldsymbol{k},\lambda}\cdot\boldsymbol{p}\,|\Psi_0\rangle\,e^{-i\omega_{\boldsymbol{k}}t} \\ &+ i\alpha\sqrt{\frac{2\pi N_{\boldsymbol{k},\lambda}}{V\omega_{\boldsymbol{k}}\alpha^2}}\,\langle\Psi_f|\,(\boldsymbol{k}\cdot\boldsymbol{x})(\boldsymbol{\epsilon}_{\boldsymbol{k},\lambda}\cdot\boldsymbol{p})\,|\Psi_0\rangle\,e^{-i\omega_{\boldsymbol{k}}t}.\end{aligned} \tag{3.2.5}$$

Here the scalar products of the photon number states are readily calculated using their orthogonality. Also we recalled that in quantum mechanics the momentum is

given as $\boldsymbol{p} = -i\nabla$.

Let us focus on the dipole term first. Using a standard quantum mechanics commutation relation,

$$\left[\boldsymbol{x}, \hat{H}_0\right] = i\boldsymbol{p}, \tag{3.2.6}$$

one can rewrite the matrix element as:

$$\langle F|\, \hat{H}_D\, |I\rangle = i\alpha\sqrt{\frac{2\pi N_{\boldsymbol{k},\lambda}}{V\omega_{\boldsymbol{k}}\alpha^2}}\omega_{f0}\boldsymbol{\epsilon}_{\boldsymbol{k},\lambda}\cdot\langle\Psi_f|\, \boldsymbol{x}\, |\Psi_0\rangle\, e^{-i\omega_{\boldsymbol{k}}t}. \tag{3.2.7}$$

Where $\omega_{f0} = E_f - E_0$. Next, we take on the quadrupole term in 3.2.5. Omitting the constants we can rewrite the term dividing it into an antisymmetric and symmetric part, respectively:

$$\begin{aligned}&\langle\Psi_f|\, (\boldsymbol{k}\cdot\boldsymbol{x})(\boldsymbol{\epsilon}_{\boldsymbol{k},\lambda}\cdot\boldsymbol{p})\, |\Psi_0\rangle = \langle\Psi_f|\, k_i x_i p_j (\epsilon_{\boldsymbol{k},\lambda})_j\, |\Psi_0\rangle \\ &= \frac{1}{2}k_i(\epsilon_{\boldsymbol{k},\lambda})_j\, \langle\Psi_f|\, x_i p_j - x_j p_i\, |\Psi_0\rangle + \frac{1}{2}k_i(\epsilon_{\boldsymbol{k},\lambda})_j\, \langle\Psi_f|\, x_i p_j + x_j p_i\, |\Psi_0\rangle\,,\end{aligned} \tag{3.2.8}$$

where one sums over the repeated indices. The first, antisymmetric, part is the so called magnetic dipole [26] revealed by its regular form $(\boldsymbol{k}\times\boldsymbol{\epsilon}_{\boldsymbol{k},\lambda})\cdot\langle\Psi_f|\, \boldsymbol{x}\times\boldsymbol{p}\, |\Psi_0\rangle$. We shall ignore the magnetic dipole here, since we are only only looking at electric transitions and it is small compared to the electric transitions anyway. The second part can be reduced by first using the quantum mechanical commutator of position and momentum, $[x_i, p_j] = i\delta_{ij}$, and then writing momentum using 3.2.6 again. We obtain:

$$\begin{aligned}\langle\Psi_f|\, (\boldsymbol{k}\cdot\boldsymbol{x})(\boldsymbol{\epsilon}_{\boldsymbol{k},\lambda}\cdot\boldsymbol{p})\, |\Psi_0\rangle &\approx \frac{1}{2}k_i(\epsilon_{\boldsymbol{k},\lambda})_j\, \langle\Psi_f|\, x_i p_j + x_j p_i\, |\Psi_0\rangle \\ &= \frac{1}{2}k_i(\epsilon_{\boldsymbol{k},\lambda})_j\, \langle\Psi_f|\, x_i p_j + p_i x_j + i\delta_{ji}\, |\Psi_0\rangle \\ &= \frac{i}{2}\omega_{0f}k_i(\epsilon_{\boldsymbol{k},\lambda})_j\, \langle\Psi_f|\, x_i x_j\, |\Psi_0\rangle\,,\end{aligned} \tag{3.2.9}$$

where $\omega_{0f} = E_0 - E_f$ and the δ_{ij} term on the second line vanishes due to the condition $\boldsymbol{k}\cdot\boldsymbol{\epsilon}_{\boldsymbol{k},\lambda} = 0$. Here $x_i x_j$ is often replaced by the quadrupole operator

$$Q_{ij} = x_i x_j - \frac{1}{3}x^2\delta_{ij}, \tag{3.2.10}$$

as the second term will never contribute due to $\boldsymbol{k} \cdot \boldsymbol{\epsilon}_{\boldsymbol{k},\lambda} = 0$. The final form for the quadrupole matrix elements is thus given:

$$\langle F| \hat{H}_Q |I\rangle = -\frac{\alpha}{2}\sqrt{\frac{2\pi N_{\boldsymbol{k},\lambda}}{V\omega_{\boldsymbol{k}}\alpha^2}}\omega_{0f}k_i(\epsilon_{\boldsymbol{k},\lambda})_j \langle \Psi_f| Q_{ij} |\Psi_0\rangle e^{-i\omega_{\boldsymbol{k}}t}. \tag{3.2.11}$$

In the results 3.2.7 and 3.2.11 the energy difference ω_{f0} appears. In order for the absorption to take place, this energy must be the same as that of the annihilated photon, conversely, the same applies in emission, therefore we can remark $\omega_{f0} \approx \omega_{\boldsymbol{k}}$. Comparing these results with the definition of the electric field operator of the free electromagnetic field (see appendix A) one can deduce that, in the sense of matrix elements, the following approximations can be used:

$$\begin{aligned} \hat{H}_D(\boldsymbol{x}, t) &= \boldsymbol{E}(t) \cdot \boldsymbol{x} \\ \hat{H}_Q(\boldsymbol{x}, t) &= \frac{i}{2}k_i E_j(t) Q_{ij}. \end{aligned} \tag{3.2.12}$$

Checking the emission case, where one looks at $\langle I| \hat{H}_{int} |F\rangle$ transitions, is an identical calculation to the preceding one.

4. Traditional Resonant Inelastic X-ray Scattering

We have so far reviewed the generalities of radiation matter interaction and as a result obtained the interaction Hamiltonian. Next we shall turn our scope to the particular method at hand — Resonant Inelastic X-ray Scattering (RIXS). Even though our final description of the stimulated RIXS process relies on a fundamentally different approach, it is beneficial to take a look at the traditional Kramers-Heisenberg approach and to try and understand the physics of the process.

The traditional method presented here will utilize the machinery of perturbation theory in order to produce the differential cross section of the traditional RIXS process. The basis of this approach is the interaction Hamiltonian 3.1.21 derived in the previous chapter. Starting from the interaction Hamiltonian shall derive the traditional RIXS cross section hoping that it will shed some light into the process and will give perspective in the future when dealing with the theory of stimulated RIXS. We shall also try and give a physical interpretation of the theory as we go. We will introduce some samples and situations where RIXS will prove useful and review the standard experimental methods.

4.1 Theoretical model

4.1.1 Transitions rates

In this section we shall derive the the RIXS cross-section starting from the Hamiltonian 3.1.19. The Hamiltonian consists of two parts, the $\hat{H}_0$ describing the unperturbed system and the perturbation $\hat{H}_{int}$ describing the interaction. Let us write a general state in the interaction picture [26] as

$$|\Psi, t\rangle_I = e^{i\hat{H}_0 t} |\Psi, t\rangle , \tag{4.1.1}$$

accompanied with an initial condition $\lim_{t\to-\infty} |\Psi, t\rangle_I = |\Psi, t\rangle = |I\rangle$. This can be enforced by adiabatic switching, i.e. adding an exponential that guarantees the condition [31, 35]. Let us apply this to the Schrödinger equation, also transformed to the interaction picture:

$$i\frac{\partial}{\partial t} |\Psi, t\rangle_I = \underbrace{e^{i\hat{H}_0 t} \hat{H}_{int} e^{-\epsilon|t|} e^{-i\hat{H}_0 t}}_{=H_I(t)} |\Psi, t\rangle_I . \tag{4.1.2}$$

The above equation is solved in the perturbation theory using the time evolution operator $U(t, t_0)$ that evolves a state from the time t_0 to t:

$$|\Psi, t\rangle_I = U(t, t_0) |\Psi, t_0\rangle_I . \tag{4.1.3}$$

Plugging this back into the Schrödinger equation the form of time evolution operator is solved to be

$$U(t, t_0) = \mathcal{T} e^{-i\int_{t_0}^{t} dt' \hat{H}_I(t')}, \tag{4.1.4}$$

where $\mathcal{T}$ is the time ordering operator. The expansion of the above exponential is called the Dyson series [26].

We are interested in calculating the transition amplitude mediated by $\hat{H}_I$ from a completely unperturbed initial state of the atomic system to an arbitrary state long after the perturbation. From there we can easily derive any observable of interest,

most importantly the scattering cross section. Thus, the initial state $|I\rangle$ is chosen to be the far in the past limit of any state $|\Psi, t\rangle_I$, as defined before using adiabatic shifting. Then the initial state is a product state

$$|I\rangle = |N_{EM}\rangle \otimes \left|\Psi_0^{N_{el}}\right\rangle, \tag{4.1.5}$$

where $|N_{EM}\rangle$ is the number state describing the electromagnetic field containing N_{EM} photons in the mode $(\boldsymbol{k}_{in}, \lambda_{in})$ and $\left|\Psi_0^{N_{el}}\right\rangle$ is the ground state of the atom or a molecule containing N_{el} electrons. Note that we have chosen to consider the ground state here but the initial state is actually arbitrary. This is the state before the interaction, which according to perturbation theory, is assumed to be an eigenstate of the unperturbed Hamiltonian: $\hat{H}_0 |I\rangle = E_I |I\rangle = (E_{EM} + E_0^{N_{el}}) |I\rangle$. The final state will be defined more carefully later, but for now, let $|F\rangle$ be an arbitrary state with the constraint $|F\rangle \neq |I\rangle$ [35]. We can now calculate the scattering matrix (S-matrix) of the scattering process. The S-matrix is a mapping from initially asymptotically free particles to the finally asymptotically free particles, i.e. it connects the initial and final states mathematically. We take the limit $t_0 \to -\infty$ in the Dyson series 4.1.4 in accordance with the initial state. The S-matrix is the limit of transition amplitude at large times implemented as a limit $t \to \infty$. We have up to second order in Dyson series:

$$\begin{aligned} S_{FI} = &\lim_{t\to\infty} \langle F| U(t, -\infty) |I\rangle \\ &- i \int_{-\infty}^{\infty} dt e^{i(E_F - E_I)t} \langle F| \hat{H}_{int} |I\rangle \\ &- \int_{-\infty}^{\infty} dt \sum_M e^{i(E_F - E_M)t} \langle F| \hat{H}_{int} |M\rangle \times \int_{-\infty}^{t} dt' e^{i(E_M - E_I - i\epsilon)t'} \langle M| \hat{H}_{int} |I\rangle . \end{aligned} \tag{4.1.6}$$

Here $|M\rangle$ is a intermediate state introduced into the calculation as a unity $|M\rangle \langle M| = \mathbb{1}$. Here E_X is the energy of the state $|X\rangle$ calculated implicitly using operator exponentials. Next, using the definition of the Dirac delta [40] on the first term, performing the dt' integration on the second and using the Dirac delta again for the

dt integral we obtain:

$$S_{FI} = -2\pi i\delta(E_F - E_I)\left[\langle F|\,\hat{H}_{int}\,|I\rangle + \sum_M \frac{\langle F|\,\hat{H}_{int}\,|M\rangle\,\langle M|\,\hat{H}_{int}\,|I\rangle}{E_M - E_I - i\epsilon}\right]. \tag{4.1.7}$$

Note that the limit $\epsilon \to 0$ is also taken appropriately.

The transition rate is defined via the transition amplitude by the Fermi's golden rule [26]. Mathematically this reads:

$$\Gamma_{FI} = \lim_{T\to\infty} \frac{|S_{FI}|^2}{T}, \tag{4.1.8}$$

where T is the time. Here we have a problematic term where the Dirac delta is squared. In the sense of distributions it is not well defined to do the multiplication [41], but there exists a somewhat heuristic workaround that we shall employ here [42]. Let us write the square as a product using the integral definition of the delta function:

$$\delta(E_F - E_I)^2 = \lim_{T\to\infty} \delta(E_F - E_I)\int_{-T/2}^{T/2} \frac{dt}{2\pi} e^{i(E_F - E_i)t}. \tag{4.1.9}$$

Now, one can argue that, due to the delta function before the integral, the above is equal zero unless $E_F - E_I = 0$, accordingly, we set $E_F - E_I = 0$ in the exponential in the integral. The integral then reduces to a very simple result and we are left with

$$\delta(E_F - E_I)^2 = \lim_{T\to\infty} \delta(E_F - E_I)\frac{T}{2\pi}. \tag{4.1.10}$$

Although seemingly irrational, the result perfectly coincides with the definition of the transition rate and nicely removes the time dependence with the limit. We obtain the result:

$$\Gamma_{FI} = 2\pi\delta(E_F - E_I)\left|\langle F|\,\hat{H}_{int}\,|I\rangle + \sum_M \frac{\langle F|\,\hat{H}_{int}\,|M\rangle\,\langle M|\,\hat{H}_{int}\,|I\rangle}{E_M - E_I - i\epsilon}\right|^2. \tag{4.1.11}$$

Here we have two terms within the $|\cdots|^2$. The terms shall be referred to as the first order perturbation term and the second order perturbation term, respectively.

4.1.2 The cross section

The previous result 4.1.11 is a relatively general one. In order to proceed we must specify the system more carefully along with all the states that are relevant to the process under investigation. The initial state has already been specified before in 4.1.5 as the state way before the interaction is regularly the desired onset. The final state and all the possible intermediate states need to be figured out and the sum of those contributions calculated. Next, we are going to do this in the case of RIXS. We shall separate the processes arising from the $\boldsymbol{A}^2$ and $\boldsymbol{p}\cdot\boldsymbol{A}$ components of the interaction Hamiltonian 3.1.21 and see that the latter gives rise to resonant scattering.

Before doing this, however, a word about the initial photon state in 4.1.5 is in order. There we assumed a pure state with only one photon mode. This is a sufficient simplification as we only look at single photon absorptions and emissions at a time and are dealing with a low order process. In general, an arbitrary radiation field has mixed states and is represented correctly only by a density matrix [31, 43].

Let us first specify the final state we are interested in. RIXS is an inelastic scattering event meaning that one photon is absorbed from the initial state $|I\rangle$ and another is emitted in a different mode $(\boldsymbol{k}_F, \lambda_F) \neq (\boldsymbol{k}_{in}, \lambda_{in})$. The atomic or molecular state is modified accordingly in the process. Therefore the final state is given as [35]:

$$|F\rangle = \left|\Psi_F^{N_{el}}\right\rangle \hat{a}^\dagger_{\boldsymbol{k}_F,\lambda_F} |N_{EM} - 1\rangle\,, \tag{4.1.12}$$

where we dropped the tensor product sign. Now, the intermediate state $|M\rangle$ can be one of two possibilities [35]. Intuitively, the absorption of the incoming photon happens before the emission. Then the intermediate state is exactly what you expect:

$$|M\rangle = \left|\Psi_M^{N_{el}}\right\rangle |N_{EM} - 1\rangle\,. \tag{4.1.13}$$

However, there is nothing in the theory that prevents the apparent time-reversal of

these events. Then the emission takes place before the absorption and, consequently, the intermediate state is

$$|M\rangle = \left|\Psi_M^{N_{el}}\right\rangle \hat{a}^\dagger_{\boldsymbol{k}_m,\lambda_m} |N_{EM}\rangle \,. \tag{4.1.14}$$

Now, all that is left is to plug these into 4.1.11 and use the brute force algorithm to find out the result. This is a relatively simple but tedious calculation so let us simply write down the result accompanied with some explanation of the terms. As one can guess, there will be altogether three terms: One from the first order perturbation term in 4.1.11, and two from the second order term utilizing the different intermediate states. It is evident that with the defined initial and final states only the $\boldsymbol{A}^2$ contribution in the interaction Hamiltonian 3.1.21 can produce a finite result in first order perturbation. This will be the first term. In second order perturbation theory, on the other hand, we only get contribution from the $\boldsymbol{p}\cdot\boldsymbol{A}$ term in $\hat{H}_{int}$ using the intermediate states defined above. With these definitions the transition rate is given by [35]:

$$\begin{aligned}
\Gamma_{FI} =& 2\pi\delta(E_F^{N_{el}} - \omega_F - E_0^{N_{el}} - \omega_{in})\alpha^4 \\
&\times \left| \frac{1}{2}\int d^3x \left\langle \Psi_F^{N_{el}}\right| \langle N_{EM}-1|\, \hat{a}_{\boldsymbol{k}_F,\lambda_F}\hat{\psi}^\dagger(\boldsymbol{x})\hat{\boldsymbol{A}}^2(\boldsymbol{x})\hat{\psi}(\boldsymbol{x}) \left|\Psi_0^{N_{el}}\right\rangle |N_{EM}\rangle \right. \\
&- \int d^3x d^3x' \sum_M \left(\left\langle \Psi_F^{N_{el}}\right| \langle N_{EM}-1|\, \hat{a}_{\boldsymbol{k}_F,\lambda_F}\hat{\psi}^\dagger(\boldsymbol{x})\hat{\boldsymbol{A}}(\boldsymbol{x})\cdot\nabla\hat{\psi}(\boldsymbol{x}) \right. \\
&\times \frac{\left|\Psi_M^{N_{el}}\right\rangle |N_{EM}-1\rangle \langle N_{EM}-1| \left\langle \Psi_M^{N_{el}}\right|}{E_0^{N_{el}} - E_M^{N_{el}} + \omega_{in} + i\epsilon} \hat{\psi}^\dagger(\boldsymbol{x}')\hat{\boldsymbol{A}}(\boldsymbol{x}')\cdot\nabla'\hat{\psi}(\boldsymbol{x}') \left|\Psi_0^{N_{el}}\right\rangle |N_{EM}\rangle \Big) \\
&- \int d^3x d^3x' \sum_{M,m} \left(\left\langle \Psi_F^{N_{el}}\right| \langle N_{EM}-1|\, \hat{a}_{\boldsymbol{k}_F,\lambda_F}\hat{\psi}^\dagger(\boldsymbol{x})\hat{\boldsymbol{A}}(\boldsymbol{x})\cdot\nabla\hat{\psi}(\boldsymbol{x}) \right. \\
&\left. \left. \times \frac{\left|\Psi_M^{N_{el}}\right\rangle \hat{a}^\dagger_{\boldsymbol{k}_m,\lambda_m} |N_{EM}\rangle \langle N_{EM}| \hat{a}_{\boldsymbol{k}_m,\lambda_m} \left\langle \Psi_M^{N_{el}}\right|}{E_0^{N_{el}} - E_M^{N_{el}} + \omega_m + i\epsilon} \hat{\psi}^\dagger(\boldsymbol{x}')\hat{\boldsymbol{A}}(\boldsymbol{x}')\cdot\nabla'\hat{\psi}(\boldsymbol{x}') \left|\Psi_0^{N_{el}}\right\rangle |N_{EM}\rangle \Big) \right|^2 .
\end{aligned} \tag{4.1.15}$$

The physical interpretation of the three terms in the formula 4.1.15 contained within the $|\cdots|^2$ is diagrammatically represented in figure 4.1. These diagrams are

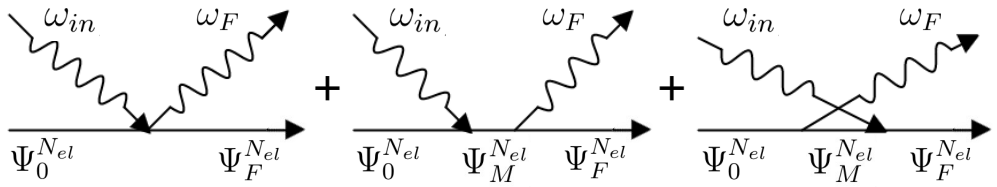

Figure 4.1: Diagrammatic representation of the terms in 4.1.15. The first term on the left describes simultaneous absorption and emission without an intermediate state, whereas the last two have core-excited intermediate states but are time reversed versions of each other.

similar to, but not exactly, Feynman diagrams. In respective order, we have the first order perturbation theory term describing simultaneous absorption and emission plus the two terms arising from second order perturbation theory. The second order terms have a short lived core-excited intermediate state $\left|\Psi_M^{N_{el}}\right\rangle$ in the middle. These terms are time reversed in the sense that in the last term the emission takes place before the absorption. Physically this arises from the fact that the intermediate product state $|M\rangle$ is actually a virtual state, thus, we cannot exactly know the time of absorption or emission [18].

The first order term is responsible for X-ray Thomson scattering [18,36], which offers information about the electron densities and excitations caused by charge fluctuations [16]. For our purposes, the second order term with regular time ordering is the one of interest however. A RIXS experiment is arranged so that the incident photon energy is close to an absorption edge: $E_0^{N_{el}} - E_M^{N_{el}} + \omega_{in} \approx 0$, thus, the second term in 4.1.15 dominates over the other two [16]. From now on we will direct our interest solely on this term. It is, however, important to recognise the fact that these three terms are, in fact, inseparable. Looking at the formula 4.1.15 makes this mathematically obvious: All the terms are under the same square. Possible interferences may have affects in the line shape of the spectrum, in most cases however, we can neglect the first and the last term in 4.1.15 close to a strong resonance [18].

Being finally able to justify the leading order term in the transition rate formula, we can move forward. Let us write the dominant second order term again and plug in the vector potential 3.1.17. Allowing for the ladder operators to operate on the photon number states and using orthogonality we find the non-zero terms in the vector potential expansion. We acquire [35]:

$$\begin{aligned}\Gamma_{FI} =& \frac{(2\pi)^3 N_{EM}}{V^2 \omega_F \omega_{in}} \delta(E_F^{N_{el}} + \omega_F - E_0^{N_{el}} - \omega_{in}) \\ & \times \left| \int d^3x d^3x' \sum_M \left\langle \Psi_F^{N_{el}} \right| \hat{\psi}^\dagger(\boldsymbol{x}) e^{-i\boldsymbol{k}_F \cdot \boldsymbol{x}} \boldsymbol{\epsilon}^*_{\boldsymbol{k}_F, \lambda_F} \cdot \nabla \hat{\psi}(\boldsymbol{x}) \right. \\ & \left. \times \frac{\left| \Psi_M^{N_{el}} \right\rangle \left\langle \Psi_M^{N_{el}} \right|}{E_0^{N_{el}} - E_M^{N_{el}} + \omega_{in} + i\epsilon} \hat{\psi}^\dagger(\boldsymbol{x}') e^{i\boldsymbol{k}_{in} \cdot \boldsymbol{x}'} \boldsymbol{\epsilon}_{\boldsymbol{k}_{in}, \lambda_{in}} \cdot \nabla' \hat{\psi}(\boldsymbol{x}') \left| \Psi_0^{N_{el}} \right\rangle \right|^2 .\end{aligned} \tag{4.1.16}$$

Next we expand the field operators according to 2.1.7 using spin-orbitals as the coefficients. Plugging these expansions in and separating the operators between correct bra-kets will produce:

$$\begin{aligned}\Gamma_{FI} =& \frac{(2\pi)^3 N_{EM}}{V^2 \omega_F \omega_{in}} \delta(E_F^{N_{el}} + \omega_F - E_0^{N_{el}} - \omega_{in}) \\ & \times \left| \sum_{M,a,i,p,q} \langle \varphi_p | e^{-i\boldsymbol{k}_F \cdot \boldsymbol{x}} \boldsymbol{\epsilon}^*_{\boldsymbol{k}_F, \lambda_F} \cdot \nabla | \varphi_q \rangle \langle \varphi_a | e^{i\boldsymbol{k}_{in} \cdot \boldsymbol{x}'} \boldsymbol{\epsilon}_{\boldsymbol{k}_{in}, \lambda_{in}} \cdot \nabla' | \varphi_i \rangle \right. \\ & \left. \times \frac{\left\langle \Psi_F^{N_{el}} \right| \hat{c}_p^\dagger \hat{c}_q \left| \Psi_M^{N_{el}} \right\rangle \left\langle \Psi_M^{N_{el}} \right| \hat{c}_a^\dagger \hat{c}_i \left| \Psi_0^{N_{el}} \right\rangle}{E_0^{N_{el}} - E_M^{N_{el}} + \omega_{in} + i\epsilon} \right|^2 .\end{aligned} \tag{4.1.17}$$

Here the two integrals over $\boldsymbol{x}$ an $\boldsymbol{x}'$ have already been written in the bra-ket notation on the second line. We were also smart in advance and chose the indices of the orbitals conveniently. In order to obtain an interpretation in single particle-hole transitions we will rely on configuration interaction method from section 2.2. In principle, all reachable intermediate states are contained within the sum at this point. This contains all the correlated states. The intermediate states can be off shell in the sense that the sub-processes may not conserve energy, only the total process must [35]. The delta function ensures this. Thus, RIXS probes electron correlations, even though the process seemingly appears as a couple of photon in / photon out single particle-hole transitions. In addition to elementary excitations,

collective modes are probed. These include quasi-particles such as phonons and magnons, charge transfer modes etc. [15–18]. Let us, however, view the process from the point of view of the photoabsorption and emission in the light of single particle-hole transitions. Photoabsorption excites a state and creates a core hole whereas the emission is observed due to de-excitation and filling of the core hole.

Let us assume that the initial state can be approximated by the first Slater determinant from the 2.2.9 and that the intermediate and final states can be approximated by singly excited determinants. We restrict our description to single excitations. Let us allow for multiple intermediate states but fix the final state. This way we are able to take into account for the possibility of multiple intermediate states up to single particle-hole order. In principle, a truly monochromatic source can promote an electron only to a specific state. This is almost never the case, but there are states very close in energy and the spectrum of the source has a finite width. We shall use the following approximations for the exact states:

$$\left|\Psi_0^{N_{el}}\right\rangle \approx \left|\Phi_0\right\rangle, \quad \left|\Psi_M^{N_{el}}\right\rangle \approx \left|\Phi_i^a\right\rangle \quad \text{and} \quad \left|\Psi_F^{N_{el}}\right\rangle \approx \left|\Phi_j^b\right\rangle, \tag{4.1.18}$$

where $j \neq i$. The intermediate and final states are singly excited determinants as oppose to the ground state. Note that in the intermediate state the orbital j must be an occupied one. The final state is a specific determinant whereas the indices in the intermediate state are chosen on purpose to consider the sum over correlations. By plugging these into 4.1.17 we obtain [35]

$$\begin{aligned}\Gamma_{FI} =& \frac{(2\pi)^3 N_{EM}}{V^2 \omega_F \omega_{in}} \delta(E_j^b + \omega_F - E_0^{N_{el}} - \omega_{in}) \\ &\times \left| \sum_{a,i,p,q} \left\langle \varphi_p \right| e^{-i\boldsymbol{k}_F \cdot \boldsymbol{x}} \boldsymbol{\epsilon}^*_{\boldsymbol{k}_F,\lambda_F} \cdot \nabla \left| \varphi_q \right\rangle \left\langle \varphi_a \right| e^{i\boldsymbol{k}_{in} \cdot \boldsymbol{x}'} \boldsymbol{\epsilon}_{\boldsymbol{k}_{in},\lambda_{in}} \cdot \nabla' \left| \varphi_i \right\rangle \right. \\ &\times \left. \frac{\left\langle \Phi_j^b \right| \hat{c}_p^\dagger \hat{c}_q \left| \Phi_i^a \right\rangle \left\langle \Phi_i^a \right| \hat{c}_a^\dagger \hat{c}_i \left| \Phi_0 \right\rangle}{E_0^{N_{el}} - E_i^a + \omega_{in} + i\epsilon} \right|^2 .\end{aligned} \tag{4.1.19}$$

The matrix elements on the last line can be calculated using the definitions from the section 2.2 and produce a set of Kronecker deltas. Performing these calculations

and applying the results finally yields:

$$\begin{aligned}\Gamma_{FI} =& \frac{(2\pi)^3 N_{EM}}{V^2 \omega_F \omega_{in}} \delta(\varepsilon_a - \varepsilon_j + \omega_F - \omega_{in}) \\ &\times \left| \frac{\langle \varphi_i | \, e^{-i\boldsymbol{k}_F \cdot \boldsymbol{x}} \boldsymbol{\epsilon}^*_{\boldsymbol{k}_F, \lambda_F} \cdot \nabla \, | \varphi_j \rangle \, \langle \varphi_a | \, e^{i\boldsymbol{k}_{in} \cdot \boldsymbol{x}'} \boldsymbol{\epsilon}_{\boldsymbol{k}_{in}, \lambda_{in}} \cdot \nabla' \, | \varphi_i \rangle}{\varepsilon_i - \varepsilon_a + \omega_{in} + i\epsilon} \right|^2 .\end{aligned} \tag{4.1.20}$$

Note that this is the contribution of one scattering channel, in an experiment, however, there might be multiple channels which need to be accounted for in a similar fashion.

We have now the final form of the transition rate 4.1.20. All that is left to do is to calculate the scattering cross section based on this. We define the photon flux as

$$J = \frac{N_{EM}}{\alpha V}, \tag{4.1.21}$$

and the total scattering cross section follows:

$$\sigma = \frac{\Gamma_{FI}}{J}. \tag{4.1.22}$$

Thus, the differential scattering cross section can be written as a derivative with respect to spatial solid angle Ω and energy of the scattered photon ω_F [31]:

$$\frac{d^2\sigma}{d\Omega d\omega_F} = \frac{V\alpha^3}{(2\pi)^3} \omega_F^2 \frac{\Gamma_{FI}}{J}, \tag{4.1.23}$$

finally yielding the differential scattering cross section:

$$\begin{aligned}\frac{d^2\sigma}{d\Omega d\omega_{out}} =& \alpha^4 \frac{\omega_{out}}{\omega_{in}} \delta(\varepsilon_a - \varepsilon_j + \omega_{out} - \omega_{in}) \\ &\times \left| \frac{\langle \varphi_i | \, e^{-i\boldsymbol{k}_{out} \cdot \boldsymbol{x}} \boldsymbol{\epsilon}^*_{\boldsymbol{k}_{out}, \lambda_{out}} \cdot \nabla \, | \varphi_j \rangle \, \langle \varphi_a | \, e^{i\boldsymbol{k}_{in} \cdot \boldsymbol{x}'} \boldsymbol{\epsilon}_{\boldsymbol{k}_{in}, \lambda_{in}} \cdot \nabla' \, | \varphi_i \rangle}{\varepsilon_i - \varepsilon_a + \omega_{in} + i\frac{\Gamma}{2}} \right|^2 .\end{aligned} \tag{4.1.24}$$

Note that we changed the ω_F to ω_{out} and interpreted the adiabatic shifting constant ϵ as the spectral broadening due to the life time of the core hole Γ, not to be confused with the transition rate Γ_{FI}. We assume that the lifetime broadening here contains both Auger and radiative decay, further, Γ is also assumed constant (independent of the intermediate state) [16].

What does the formula 4.1.24 tell us? It is the differential scattering cross section of the RIXS process, by definition, it describes the probability of finding the scattered photon within a certain, infinitesimal, solid angle region $d\Omega$ and energy range $d\omega_{out}$. Now, because spectrum is defined as the intensity as a function of energy or frequency, the differential cross section directly translates to a spectrum detected in a certain solid angle area. Therefore, given the solid angle of the detector and a model for calculating the transitions in the sample system, one can estimate the intensity, or amount of radiation, detected within a certain energy range using 4.1.24. Measuring this gives a direct path for cross referencing the scattering properties of the theoretical model and the sample, thus allowing the comparison of the model and actual structure of material. This is the standard process of obtaining information of material structures via scattering methods.

On a more fundamental physical level this result is to be interpreted as transition of an electron from the single particle orbital φ_i to a virtual orbital φ_a which corresponds to the excitation of the ground state into an excited state. This is followed by an inseparable transition from an orbital φ_j to the orbital φ_i which corresponds to the filling of the core hole. Once again we note that RIXS is a coherent process that consists of, but cannot be separated into, an absorption and an emission of a photon. We note a couple of characteristic properties to RIXS here. The first is the earlier mentioned resonant amplification of the cross section. In an experiment the incident energy ω_{in} is scanned over the resonance energy $\varepsilon_a - \varepsilon_i$. Close to the resonance energy the cross section will grow strongly. The other striking property of RIXS is that the spectral features obtained in RIXS can be sharper than the core hole life time broadening Γ [17, 44, 45]. This is because the line width of the emitted radiation is linearly proportional to the incident due to the energy conservation between the initial an final states.

The theoretical model derived here is the traditional Kramers-Heisenberg ap-

proach to RIXS readily embedded with the configuration interaction theory. This model works for most of the transitions and samples as long as one is able to calculate the orbitals and the result approximates the system well enough. There are also other models for resolving the underlying electron structure or band structure. For strongly correlated d and f electron systems, such as rare-earth metal compounds or transition metal compounds, the Anderson impurity model could be utilized [16].

As a final note in this section let us mention that the derivation of the cross section 4.1.24 presented here does not contain approximating the interaction Hamiltonian: The exponential that was expanded in the section 3.2 can be seen in the numerator of the cross section formula. In that sense this result is exact. It is, however, often the case that dipole and quadrupole interaction dominate over the higher order transitions. Therefore, applying dipole and quadrupole approximations here is computationally sensible and allows estimating their relative spectral strengths, which might be highly relevant to an experiment. Keep in mind, however, that strictly speaking in the sense of the cross section the dipole and quadrupole contributions are inseparable similar to what was discussed before. In an experiment one can separate between the two to a certain degree relying on selection rules [46–48]. They also usually produce peaks in the spectra that are well separated from each other in energy. Applying either one of the approximations to the formula 4.1.24 follows exactly the same steps taken in section 3.2 where the transition amplitudes were calculated.

4.2 Experimental overview

Now that we have derived the traditional theory describing RIXS, we are going to take a quick look into the experimental perspective. Even though this is a theoretical review, it is good to have an idea about the experimental side and generalities of the field.

In a RIXS experiment there are multiple parameters that can be adjusted [17], of which the absorption edge is possibly the most important as RIXS measurements are made in the vicinity of absorption edges, since the resonances occur there. Usual choices of absorption edges are the K and L-edges which offer complementary information with different emphasis on different features. Thus, one has to consider the obtainable information and the type of the transition, for instance, considering 3d transition metals, at the K-edge 1s-3d is a quadrupole transition and thus relatively weak. On the other hand 3d-transition metal L-edge 2p-3d is a dipole transition and probes the 3d states directly via dipole transition but moves the energy region to soft X-rays in contrast to the hard X-ray K-edge. Considering rare earth metals, the quadrupole allowed 2p-4f transition is a sensitive probe of the magnetically important 4f orbitals and can be reached via L-edge RIXS. Further, one might have to consider that at different edges different excitations can be created. Once the edge has been selected one must think about the incident energy ω_{in} as the choice of incident energy can emphasize some features while diminishing others [15]. On a more technical note experiment-wise, the elastic scattering intensity must be considered and minimized as well as the self absorption of the sample considered in data normalization. The choice of incident energy and the recorded emission energy ω_{out}, or energy transfer $\omega_{in} - \omega_{out}$, are the key parameters, so let us discuss their role a bit more in depth in the next subsection via an illustrative example.

4.2.1 RIXS plane

Although our discussion has been general and material-independent so far, it is useful to review RIXS by visualizing it through a concrete example. For the sake of argument, we will use a theoretical model, depicted in figure 4.2, as an example of so called 1s2p quadrupole transition RIXS in transition metals [17]. In this model we assume that the initial state $|\Psi_0\rangle$ (here also the ground state) is coupled to two

intermediate states $|\Psi_{M1}\rangle$ and $|\Psi_{M2}\rangle$ via radiation induced quadrupole transitions and that the intermediate states are coupled to three final states $|\Psi_{F1}\rangle$, $|\Psi_{F2}\rangle$ and

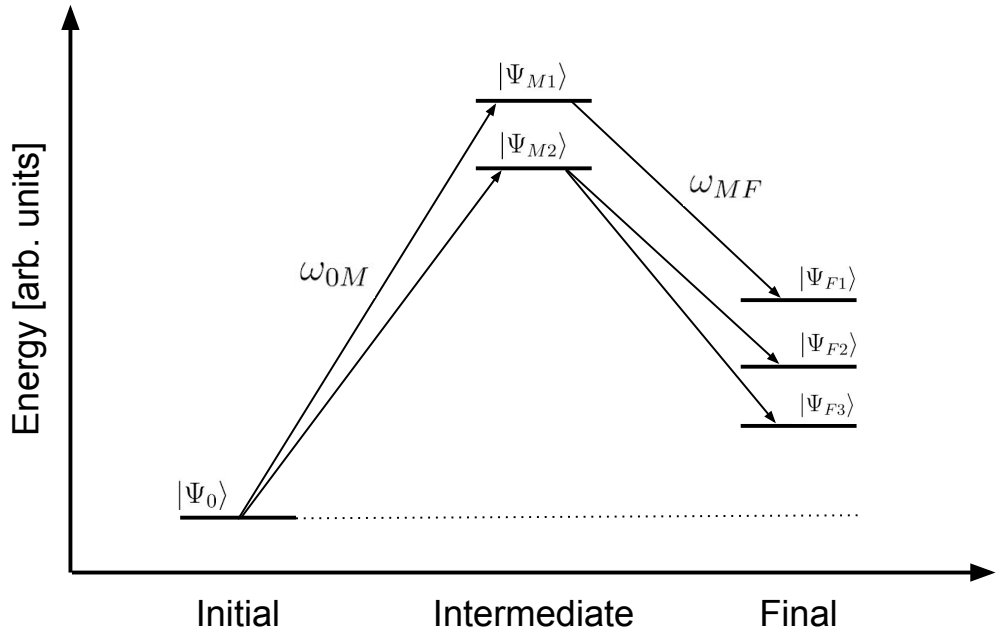

Figure 4.2: An energy level scheme showing the transitions in the model considered here. The arrows indicate the possible couplings or transitions: The initial state is coupled only to the intermediate states which are coupled to the final states according to the arrows. ω_{0M} and ω_{MF} are the energies of the transitions. Transition rates or relative energies are arbitrary and not in scale.

$|\Psi_{F3}\rangle$ via spontaneous dipole transitions. This model could describe e.g. transition metal RIXS with excitation $1s^2nd^m \rightarrow 1s^1nd^{m+1}$, where $n = 3, 4$, followed by the filling of the core hole from the p-orbitals: $1s^12p^63d^{m+1} \rightarrow 1s^22p^53d^{m+1}$ and $1s^13p^64d^{m+1} \rightarrow 1s^23p^54d^{m+1}$. Here the 2p spin-orbit splitting into $2p_{3/2}$ and $2p_{1/2}$ could be the reason for the $1s^13d^{m+1}$ state to decay into two states. We shall, however, discuss this model in a more general level without assigning specific orbitals or states, for further discussion see [17, 49].

Let us first discuss the information obtainable by RIXS, best illustrated by a concept called RIXS plane. As one can see by looking at the result 4.1.24 in a RIXS

experiment it is possible to vary both the incident photon energy ω_{in} as well as the emitted energy ω_{out}, therefore, the total spectrum that can be recorded is plotted as a two dimensional surface or a contour. A contour plot is often more useful, as seen in the bottom left corner of the figure 4.3. The standard convention of plotting the intensity against incident energy ω_{in} and energy transfer (or final state energy) $\omega_{in} - \omega_{out}$ is used. The spectrum featured here represents a RIXS process detailed above and is calculated based on the model energy level scheme in figure 4.2 with a different life time broadening for the intermediate and final states. The final state life time is possible to incorporate into the theory by using the fact that a the Dirac delta function in 4.1.24 can be written as a Lorentzian (or Cauchy) distribution [17,18,50]. Also note that in the schematic 4.2 relative transition energies and transition rates are not in scale and are taken to be arbitrary, therefore one should not interpret the relation of the schematic and the presented spectra too far. We shall not go into more detail on how these results are obtained, but rather just use them as an example of RIXS, for more details and the calculations see [17].

Let us point out few important features from the contour plot 4.3. First we note that there are two 1s resonances on the diagonal at incident energies 6542 and 6544 eV. The third peak vertically above the 6542 eV resonance peak is not a resonance, but an effect due to the splitting of the emission channel of the second intermediate state $|\Psi_{M2}\rangle$ de-exciting to $|\Psi_{F2}\rangle$ and $|\Psi_{F2}\rangle$ as seen in the schematic 4.2 [17,44]. Now, having the RIXS plane (bottom left corner 4.3) one can do several different types of line cuts or integrations in order to obtain line plot spectra. There are two integrated spectra and one line cut in the figure 4.3 that all emphasize different features. The left upper corner presents a spectrum obtained by integrating the intensity over the energy transfer $\omega_{in} - \omega_{out}$ in a narrow section around the resonances. Taking the integration limits to the same value produces a line cut with constant energy transfer, the constant energy transfer (CET) spectrum, whereas integrating over all

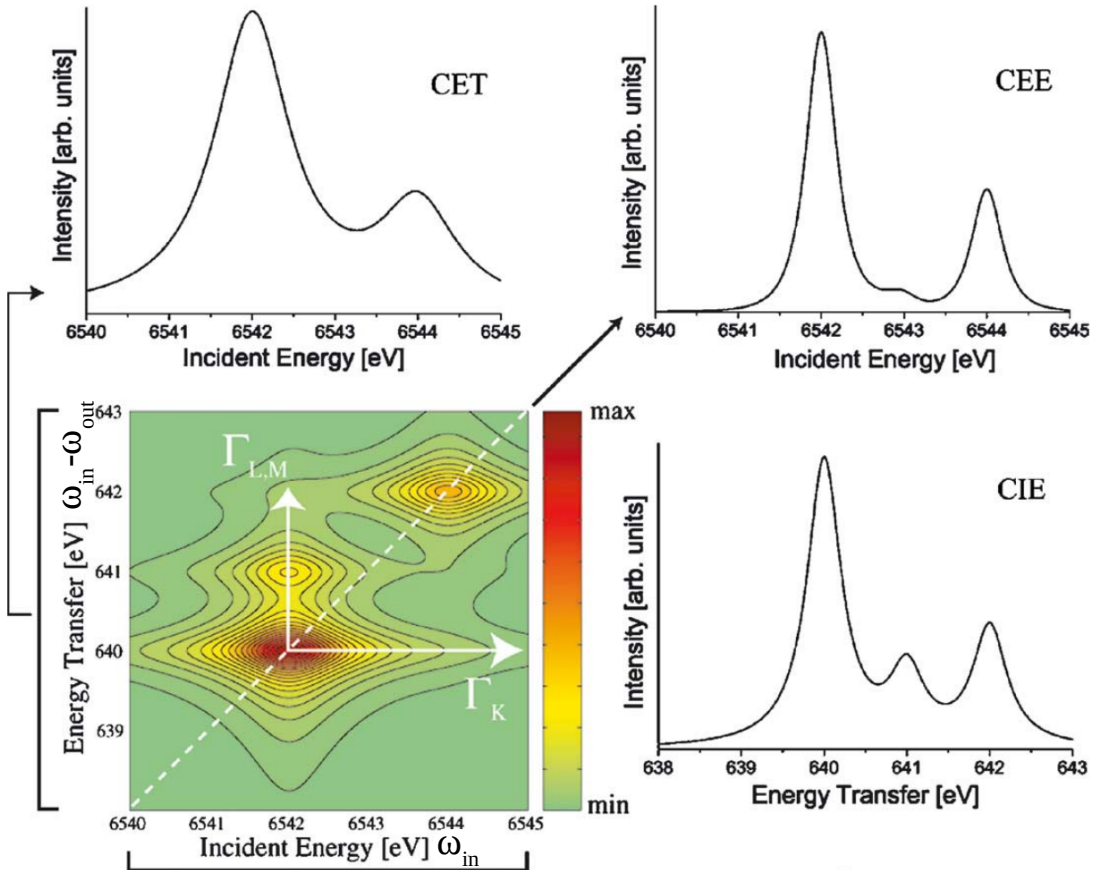

Figure 4.3: Contour plot of a RIXS plane (bottom left) accompanied by integrated line plots (top left and bottom right) and a diagonal slice. Adapted here from [17] with the permission of Elsevier.

the final states this spectrum becomes equivalent to regular X-ray Absorption Near Edge Structure (XANES) spectrum [17]. Measurements of this type correspond to scanning the incident energy while keeping the final state energy in a constant range or value. Integrating over a narrow section in the incident energy ω_{in} yields the spectrum in the bottom right corner of 4.3. Here the line cut limit taken at a single incident energy value is called a constant incident energy (CIE) spectrum. This correspond to keeping the intermediate state energy in a constant range or a single value while scanning the transferred energy. In the CET scan intermediate state features are pronounced whereas the CIE focuses on the final states. The final

line spectrum at top right corner is a diagonal line cut of the RIXS plane, which correspond to constant emission energy (CEE). Since mapping the whole RIXS plane experimentally is rather cumbersome, CEE scans are often utilized [44]: The spectrometer records at a constant emission energy ω_{out} and the incident is scanned over the resonances. Note that the third small feature between the main peaks in the CEE plot is the earlier mentioned feature due to the splitting of the emission channel of the intermediate state $|\Psi_{M2}\rangle$. In an experiment this could be accidentally interpreted as a weak resonance that was revealed by a RIXS (compared to regular X-ray absorption) [17, 44]. A look at the RIXS plane, however, reveals the true nature of this peak. This puts emphasis on the fact that it is important to be able to measure the whole RIXS plane instead of just cuts through it. However, for example in dilute systems, the signal may be weak in standard RIXS and measurement times may become prohibitively large. In those cases stimulated RIXS would be very desirable.

4.2.2 Instrumentation

Let us quickly describe a standard RIXS instrument. There are two required devices in any spectroscopy measurement. The first is the radiation source. In a modern RIXS experiment the de facto source is a synchrotron, but in fine-resolved pump-probe experiments X-ray free electron laser (XFEL) are utilized. The second device is, of course, the spectrometer. Spectrometers can be further divided in two: a soft X-ray spectrometer or a hard X-ray spectrometer.

X-ray sources

Let's first take a look at the X-ray sources. For advanced RIXS experiments storage-ring based X-ray sources are most common. In a storage-ring based synchrotron facility electrons (or positrons) are driven around a circular storage ring at a speed

very close to the speed of light. Magnets are used to turn the electron bunch and straight parts are equipped with electromagnetic cavities for accelerating to compensate the energy lost in radiation. The simplest device in the storage ring for producing radiation is the bending magnet. Bending magnets steer the electron bunch so that radiation is released due to the acceleration of charged particles. These days bending magnets are mainly used for keeping the electrons in the storage ring, since there are more powerful solutions, namely wigglers and undulators, for radiation production [18]. Both of these devises are placed in the straight parts of the storage ring. A wiggler consists of a row of strong superconducting magnets with alternating directions so that the electron bunch will undergo a wiggling motion inside [18]. Thus, compared to the bending magnet, many sharp turns release a lot more radiation than one gentle turn. The structure of a wiggler is schematically represented in figure 4.4, along with the other insertion devices. Undulator is a wiggler that is tuned so that interference effects amplify some of the frequencies and kill off others [18].

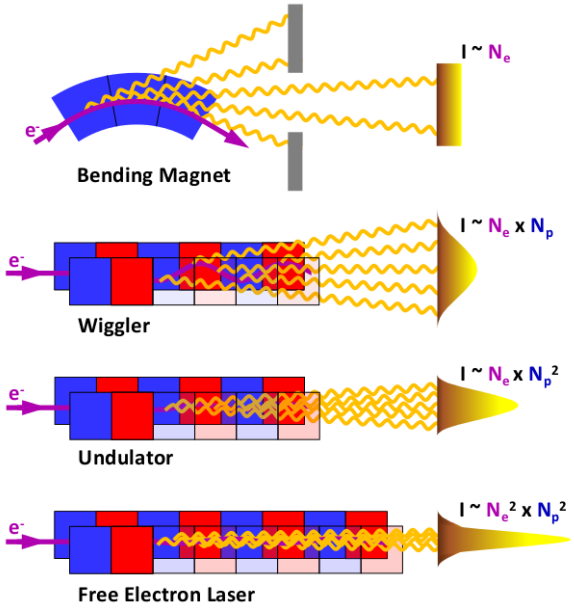

Figure 4.4: A schematic of the insertion devices [51]. The figure also shows the dependence of the intensity on number of electrons, N_e, and the number poles in the magnetic field, N_p.

Thus, an undulator produces high intensity peaks at certain frequencies, whereas the spectrum of a wiggler is wider and continuous, similar to a bending magnet [52]. The spectra of these insertion devices are compared in figure 4.5. Both wiggler and undulator radiation is tunable by varying the magnetic field strength [18].

Even though we haven't but mentioned stimulated RIXS yet, let us describe the required source for such an experiment, the X-ray free electron lasers (XFEL), here. XFEL is basically a very long undulator – the length of a regular undulator is up to five meters whereas the length of an XFEL can be over a hundred meters [2]. This is because unlike in a regular optical laser, mirrors cannot be utilized. Therefore, all the amplification must be achieved with a single pass. In an XFEL a phenomenon called self amplified spontaneous emission (SASE) occurs [53, 54]. This refers to the emitted radiation interacting with the electron inside the undulator [54]. As a consequence of SASE the initial electron bunch starts microbunching into smaller bunches separated by one radiation wavelength. The process originates from the random noise in the initial bunch. Microbunching causes the produced radiation to superimpose favoring certain wavelengths to others. This, in turn, strengthens microbunching which leads to exponential growth of intensity. This is however a relatively random process, and thus, pulses with extremely bright intensity spikes with random phases and heights are produced adding up to spectra of stochastic noise. Since microbunching reduces the phase space available for photons, the radiation shows some laser like features, despite of randomness. The pulses are transversely coherent, but temporal and spectral coherence is limited [53]. An XFEL pulse produced by SASE is shown

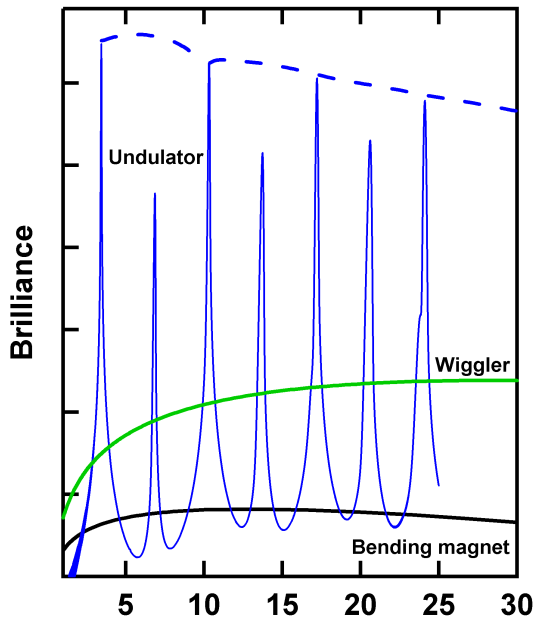

Figure 4.5: Comparison between spectra of different insertion devices [52].

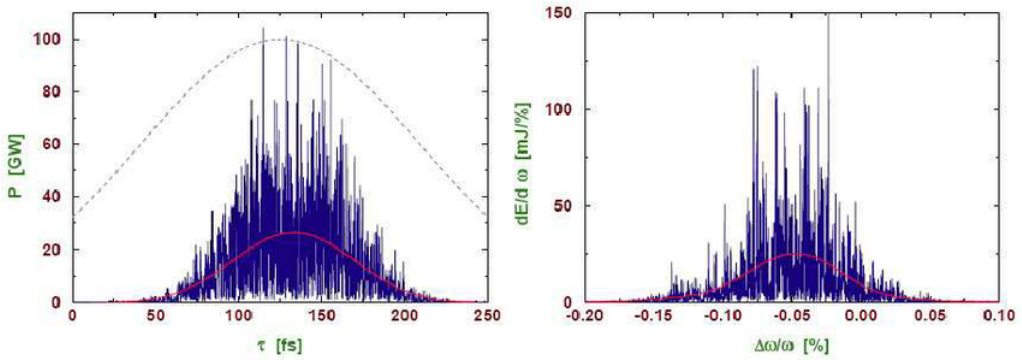

Figure 4.6: Typical XFEL SASE pulse spectrum both in time (left) and energy domain (right) [52].

in figure 4.6. All in all, using an XFEL has its pros and cons, further, one must remember that XFELs are a relatively new innovation, and new techniques are being developed all the time. We shall discuss a bit more about them in section 5.3 while considering stimulated RIXS experiments.

Spectrometers

Now that we have a suitable source for the experiment we can worry about measuring. For soft X-rays (well below 5 keV in energy) one uses a diffraction grating spectrometer, since Bragg crystal optics fail at large wavelengths [15, 18]. Such a grating is typically a line grating operated at a grazing incidence where the radiation is diffracted from the lines and the resolution is determined by the line density. The advantage of diffraction grating optics is easy tunability over a wide energy range, on the other hand, grazing incidence geometry causes low solid angle acceptance calling for precise alignment. Further, low grating reflectivities (typically few percent) require bright sources [18]. The grating can be an even plane, when a separate collection mirror has to be used, or a concave one [15]. The grating disperses the radiation to a detection device, a CCD camera, for instance, and the emitted energy is scanned by tuning the angle of the grating. A soft X-ray spectrometer is schemati-

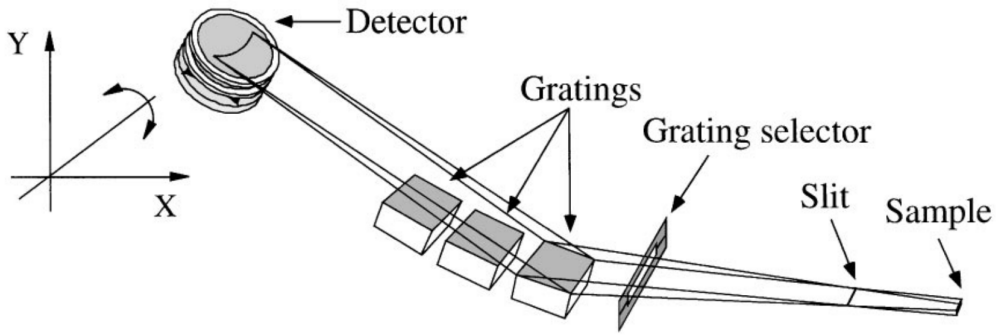

Figure 4.7: A soft X-ray spectrometer schematic. Adapted here from [18] with the permission of Elsevier.

cally picture in figure 4.7. The resolution of the detector adds up to the total resolution of the set up. In a modern RIXS instrument the whole spectrometer-detector set up can be rotated around the sample in the horizontal plane and adjusted vertically. A full description of a modern soft X-ray RIXS instrument (European Synchrotron Radiation Facility (ESRF) ID32) can be found in [55].

A hard X-ray instrument is based on crystal optics. A very high quality crystal lattice is used to Bragg reflect the signal from a sample to the detector [15]. The lattice spacing is chosen to match the used wavelengths, typically germanium or silicon is used. As in the case of soft X-ray grating concave crystals are often used to avoid separate collimation optics. Spherically bent crystals are most common. Usual set up with a spherically bent crystal uses the Rowland circle geometry. Here the sample, Bragg crystal and detector are always on a same circle of diameter R. The optimal performance is obtained in Johann geometry when the diameter R is equal to the bending radius of the crystal [15]. There are many parameters in a Bragg crystal spectrometer affecting the resolution, and the optimization of such a device is not a trivial task. The whole spectrometer set up is often built into a movable detector arm capable of moving in horizontal and vertical direction. Usually the scattering angle, i.e., the angle between the straight incoming beam path and

the position of detection, is fixed at 90° in order to minimize elastic scattering which is $\boldsymbol{\epsilon}_{in} \cdot \boldsymbol{\epsilon}_{out}$ dependent [15]. A hard X-ray spectrometer is depicted in the figure 4.8. A more complete description of hard RIXS instruments can be found for instance in refs. [34, 56].

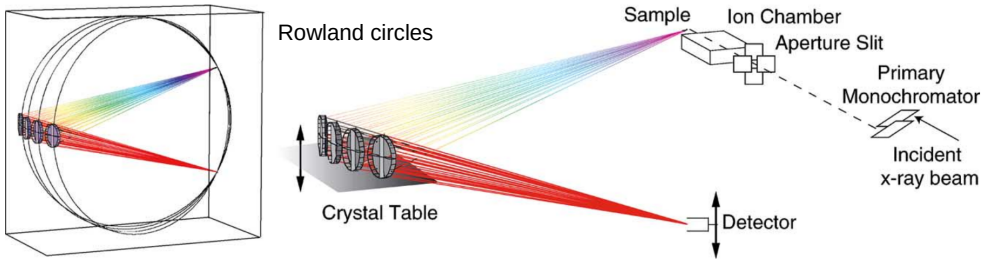

Figure 4.8: A hard X-ray spectrometer schematic. Adapted here from [15] with the permission of APS.

5. Stimulated Resonant Inelastic X-ray Scattering

Now we shall turn our focus on stimulated RIXS. We saw in the previous chapter the traditional theoretical description of the RIXS process, the Kramers-Heisenberg picture. In SRIXS we shall, however, move from the linear intensity range to the nonlinear and the traditional theory becomes inadequate: The considered intensities are so high that the response of the matter to the applied electric field is no longer linear. Therefore the theoretical description illuminating stimulated RIXS is very different from the traditional, even though the fundamental physics stays same in the sense that the interaction Hamiltonian still governs everything. First we shall introduce the basic concepts and paint an intuitive picture of the process. We will also present different X-ray pulse schemes and possible applications that have been theorized. The current state of the art is illustrated and further development of the method is motivated followed by a careful derivation of the theory. The theoretical model relies on quantum mechanical description of matter but the electric field will be assumed classical due to the extremely high intensities. Once we are done with the detailed derivation of the theory we shall collect the results into a synopsis with an illuminating explanation on the interpretation and meaning of the equations. Finally, we shall also give a short overview of the SRIXS experiment utilizing SASE pulses from X-ray free electron lasers.

5.1 Introduction

In order to obtain an intuitive picture of the process as compared to traditional RIXS, let us introduce the standard idea behind the method before jumping into the theoretical model. Stimulated RIXS is intuitively understood as a similar process to the production of laser [57]. Although different from traditional optical laser, inner-shell X-ray lasers [58–60] have actually paved the way for nonlinear X-ray spectroscopy, both theoretically and experimentally. Population inversion between the 1s and valence shell is the key to obtaining magnification of the RIXS signal by stimulation of the emissive transitions. Population inversion refers to a state where most of the atoms or molecules in the sample media are in an excited state rather than ground state. In stimulated RIXS population inversion is achieved by pumping the sample with an extremely brilliant X-ray source, namely, an X-ray free electron laser. When talking about population inversion it should be recognised that the phenomena described here are no longer in the linear region of polarization response to the applied electric field [61], i.e. we cannot assume that the polarization of the sample reacts linearly to change in intensity. Rather, we are talking about nonlinear X-ray spectroscopy. Once population inversion is achieved, the transitions to the final states are stimulated by some source of external radiation on a suitable freq-

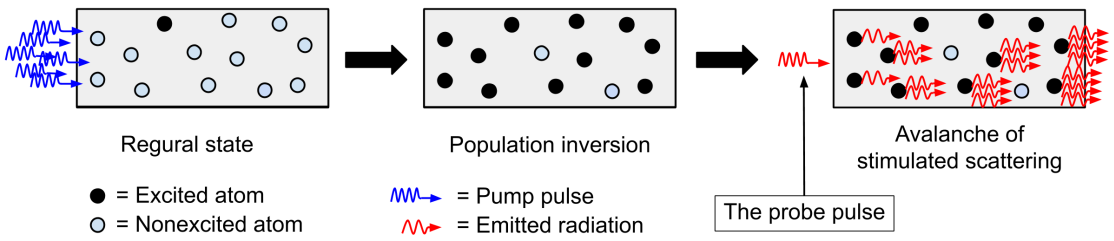

Figure 5.1: Schematic description of the SRIXS process. On the left practically all the atoms are in the ground state. In the middle a strong population inversion is present. On the right the population inversion is relaxed by a possible probe pulse leading to an avalanche of stimulated scattering events.

uency so that the desired final states are reached. Note that due to population inversion only a few seed photons with suitable energy suffice to drive an avalanche of stimulated scattering events resulting in an exponential amplification of the RIXS signal [23]. The stimulated RIXS process is schematically described in the figure 5.1. Note that there a probe pulse is depicted, even though it may not always be present: The spectral tails of the pump pulse may be enough to act as a seed. Different pulse schemes are discussed in the following section 5.1.1.

The role of stimulated emission [39] must be emphasized here. It is crucial to the process the same way as population inversion. From rudimentary analysis with Einstein coefficients one can derive the result for exponential amplification once population inversion is present [62]. This requires, however, the key property of stimulated emission. Once an atom or a molecule in an excited state interacts with a radiation field an emission of a photon in the exact same mode as the field can be stimulated [39, 57]. Therefore, all the photons that are emitted due to stimulated emission stimulate more emissions in the same mode while passing through the sample where population inversion is present. This is the intuitive picture for the exponential growth. The exponential amplification and growth in photon number is schematically depicted on the right of the above figure 5.1. We note that when stimulating with an external source we can, in principle, choose the transitions to be stimulated and therefore the final states in RIXS. Numerous schemes utilizing this process have been presented through out the last years, some more viable than others [6].

5.1.1 Pulse schemes

Let us quickly describe the possible schemes for realizing SRIXS. They can be crudely divided into two categories: the multi-colour and single-colour schemes. The multi-colour scheme uses two or more temporally separated pulses with different frequen-

cies for pumping and probing the system, whereas the single-colour scheme uses one wide bandwidth pulse that reaches both pump and probe energy regions. Probing can also be referred to as dumping. This refers to dumping electrons into the core holes that were created by pumping. Probing often refers to observing a process initiated by the pump pulse when regarding more complicated schemes. Different pump and dump schemes are presented in the figure 5.2.

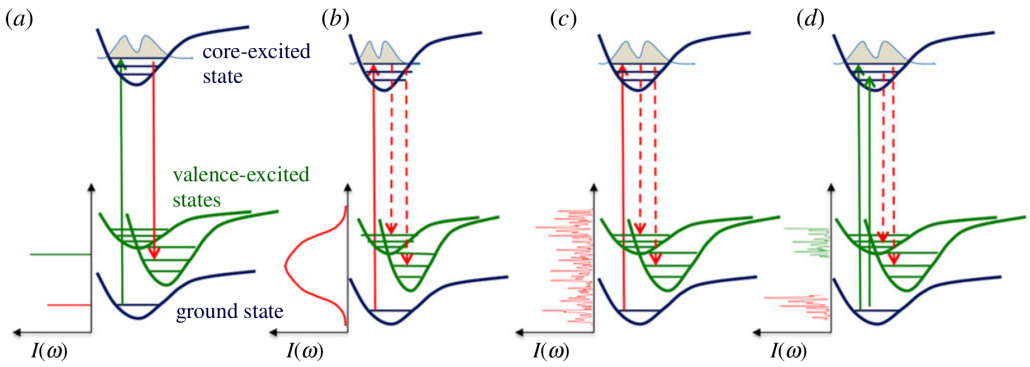

Figure 5.2: Different SRIXS pulse schemes illustrated. (a) Well defined pump and dump pulses. (b) A well defined temporally short pulse has enough bandwidth to serve as pump and dump. (c) A wide bandwidth SASE pulse has stochastic nature and changes from shot to shot. (d) Two-colour SASE. Separate but incoherent pulses. Adapted here from [6] with the permission of The Royal Society.

The ideal realization would be a multi-colour scheme using well defined X-ray pulses with highly stable and tunable duration, bandwidth, frequency and time delay [6]. For example in a simple two-colour scheme, the sample is first resonantly pumped into a population inversion followed by a time-delayed dump pulse to stimulate the transition of an electron to fill the core hole. This corresponds to the case (a) in figure 5.2. The spectrum is obtained as the difference of the incoming and transmitted dump pulse. If the pulses are completely tunable one can imagine various schemes for utilizing such a set up. Many quite complex nonlinear X-ray spectroscopy pump and probe schemes have been theorized over the recent years. These include methods for initiating and probing valence electron wave packets [19],

probing charge transfer in molecules [20] and observing electron-hole entanglement dynamics [6,21]. Even though there is theoretical evidence of these ambitious applications, the quality of currently available ultrabrilliant X-ray pulses renders experimental implementations rather impossible. As explained in section 4.2.2 the XFEL pulses produced by SASE are far from ideal. First two-colour SRIXS experiments with SASE pulses have been made but they proved unsuccessful due to suboptimal experimental conditions. These correspond to the case (d) in figure 5.2. More details can be found in [24,63]. SRIXS experiments are discussed in more depth in section 5.3.

The single-colour scheme is the simplest possible realization of SRIXS. A single wide band pulse is used for pumping and stimulating the emissive transitions to final states. Single-colour schemes are illustrated in the pictures (b) and (c) of figure 5.2. The latter describes the state of the art, a single SASE pulse. So far SRIXS has only been demonstrated using single-pulse scheme with SASE pulses [6,23]. There an XFEL pulse was tuned over the $1s^2 3p^0 \rightarrow 1s^1 3p^1$ resonance in neon. A strongly amplified emission was observed at the transition $1s^1 3p^1 \rightarrow 1s^2 2p^5 3p^1$. The high pulse intensity of XFEL achieves strong population inversion between the core and valence levels in a time comparable to the life-time of the core hole. Therefore only few photons at the frequency of the emissive transition $1s^1 3p^1 \rightarrow 1s^2 2p^5 3p^1$ suffices to initiate the avalanche of stimulated emissions. The lower energy tail of the XFEL pulse provides the seed photons for stimulating the dump transition. The spectra is recorded as the difference between incoming and transmitted pulse. In the experiment [23] a magnification of seven to nine orders of magnitude in the RIXS signal was recorded as compared to traditional spontaneous RIXS process. This is a significant improvement and stands to emphasize the fact that samples well below the limit of observation with traditional methods can be measured via stimulated RIXS.

5.2 Theoretical model

In here we shall derive the theoretical model for predicting spectra produced by SRIXS. The theoretical model presented here is quite general and can be adapted to suit many experimental conditions with minor modifications. It is a generalization of Maxwell-Bloch formalism used to describe optical stimulated Raman spectroscopy [64], and similar theories are used for describing many phenomena occurring at high X-ray pulse intensities at XFELs [65–68]. We shall, however, focus on viewing the model from the point of view of SRIXS giving a detailed derivation up to quadrupole order in interaction Hamiltonian.

In the following we shall assume one dimensional experimental geometry and utilize the paraxial approximation. This is a reasonable assumption as the sample volume is often considerably longer than the spot size of the beam, since the length of the sample is matched to the focal depth of the beam, whereas the X-ray beam is usually focused to few micrometer spot [23]. Therefore, a long but thin population inversion channel is formed within the sample, and since population inversion is the requirement for amplification, everything interesting happens within this narrow channel. We shall describe the electric field classically under slowly varying envelope approximation [39] and the sample medium by the quantum mechanical density matrix obtained by representing the states in configuration interaction theory (see 2.2). The evolution of the electric field is governed by the Maxwell equations, whereas the evolution of the density matrix is given by the Liouville-von Neumann equation [39]. The exact form of the Liouville-von Neumann equations is derived from the Schrödinger equation and coupled to the applied electric field via the nonlinear polarization response [61].

Since theoretical considerations up to dipole transitions have been presented and experimentally investigated before [5, 23, 69, 70], for the first time ever, we shall consider quadrupole transition within this framework. This is hoped to be the first

step on the road to realizing SRIXS in transition metals and making it an accessible and valuable tool for analyzing samples beyond synchrotron based methods. The Maxwell-Liouville-von Neumann equations are somewhat more system dependent than the Kramers-Heisenberg cross section, therefore, it is difficult to write down a useful final form of the equations on the same level of generality as before. Thus, in order to give an illuminating description of the theory, let us define a simple example system that still captures the essential features one might find in an actual sample in a real-life experiment. To this end we assume a similar setting as in [69], but instead of dipole transitions, we shall consider quadrupole transitions in the vicinity of some K-edge, relevant to RIXS investigations in transition metals. This scheme also resembles the one we had before in the section 4.2. Our model will describe so called 1s2p RIXS, observed in many transition metals, where a quadrupole excitation is followed by emission due to dipole transition, because the quadrupole emission channels might be too weak for current SASE pulse set ups. Ideally the XFEL pulse would only excite the exact states under investigation, but as explained in the previous section, currently such extremely narrow band gap experiments are rather impossible. Rather, the SASE pulse covers a manifold of transitions all the way up to continuum. Therefore, we must further include the possibility of competing processes into our description dividing the theoretical investigation in two parts, one covering the actual SRIXS process we are interested in, the other accounting for the possible competing processes. With this in mind, let us start investigating a SRIXS process with resonant quadrupolar excitations from the 1s orbital to the d-shell followed by stimulated dipolar emissions from the 2p orbital filling the 1s core hole:

$$\begin{aligned} &\text{Excitations:} \quad 1s^2 nd^m \to 1s^1 nd^{m+1} \\ &\text{Emissions:} \quad\ 1s^1 nd^{m+1} \to 1s^2 2p^5 nd^{m+1}. \end{aligned} \tag{5.2.1}$$

Here $n = 3, 4, 5$ and $m \in [0, 9]$ depending on the transition metal. Note that only

the relevant orbitals are displayed in the notation. Note that we have not explicitly included orbital splitting into the states here, but the theoretical model derived here allows for discrimination by angular momentum.

Now, the XFEL pulse can either cause one of the resonant excitations defined above or ionize atoms or molecules in the system. The two main processes are resonant excitations and single ionizations by promotion of 1s electron to the continuum. Even though valence electrons can also be ionized, we shall only incorporate it as a loss term rather than track the time evolution of such states. We will include the time evolution of both neutral and singly core ionized constituents into the theory by introducing two separate density matrices $\rho(t)$ and $\rho^+(t)$, describing the two in respective order. The transitions 5.2.1 are the ones between the states contained by the neutral density matrix. We will also take into account the evolution of the ions, as they have a relevant emission channel

$$\text{Emission:} \qquad 1s^1 2p^6 \rightarrow 1s^2 2p^5, \tag{5.2.2}$$

effectively leading to stimulated fluorescence in the same frequency domain as the actual SRIXS process, thus important to account for. We shall further divide the X-ray flux into two parts in energy, one below the K-edge of interest and one above, giving the total flux as a sum of the respective parts: $J = J_b + J_a$. This is because the two parts are responsible for different phenomena, excitations and ionizations, within this framework. Further, a step like absorption such as the K-edge is difficult to implement into a numerical solution. In the following two sections we will derive the time-evolution equations for the two density matrices containing the states reachable via the above defined transitions coupled to the evolution of the electric field.

5.2.1 Evolution of the neutral density matrix

Here we shall derive the equation governing the evolution of the electric field flux J_b below the K-edge, coupled with the equations governing the evolution of the density

matrix elements $\rho_{ij}(t)$ describing the SRIXS process of neutral atoms or molecules. Once again we shall begin our analysis with the matter-field Hamiltonian, this time however, we are going to start out with the approximated version of the interaction right away. Based on section 3.2 we may write the Hamiltonian, up to quadrupole order, as:

$$\begin{aligned}\hat{H} &= \hat{H}_0 + \hat{H}_{int} = \hat{H}_0 + \hat{H}_D + \hat{H}_Q \\ &= \hat{H}_0 + \boldsymbol{E}(t) \cdot \boldsymbol{x} + \frac{i}{2} k_i E_j(t) \hat{Q}_{ij}.\end{aligned} \tag{5.2.3}$$

Due to SRIXS experimental geometry, we shall immediately reduce this to one dimension. We define the coordinates so that the X-ray pulse travels in y-direction and assume a linearly polarized field in z-direction. Therefore, the Hamiltonian reads

$$\hat{H} = \hat{H}_0 + \hat{z}E(t) + \frac{i}{2} k_y E_z(t) \hat{Q}_{yz}. \tag{5.2.4}$$

From hereon the electric field will be treated classically. This is adequate since even the tails of XFEL pulses are considerably more intense than any vacuum fluctuations [69]. The dipole part of the above, fully quantum, interaction Hamiltonian is readily transformed into a semi-classical form by treating the electric field as a multiplicative constant or a dot product in one dimension. As for the quadrupole term, we have a direct relationship between momentum and position through the Fourier transform, therefore we essentially perform a Fourier transform back into the position space in order to define a classical counterpart of the quadrupole term containing photon momentum. The semi-classical Hamiltonian then reads

$$\hat{H} = \hat{H}_0 + \hat{z}E(t) + \frac{1}{2} \hat{Q} \partial_y E(t). \tag{5.2.5}$$

This result can, of course, be derived completely classically too, see for instance [71]. We note that the dipole term is related to the direct coupling of the field with matter whereas the quadrupole gives the coupling to the field derivatives of the

field. Further, we shall apply the slowly varying envelope approximation to the electric field [39, 69]:

$$E(t) = \mathcal{E}_0(t,y)e^{-i\omega_0 t} + \mathcal{E}_0^*(t,y)e^{i\omega_0 t}, \tag{5.2.6}$$

where ω_0 is the frequency of the incident field and $\mathcal{E}_0$ a slowly varying complex envelope. The wave equation describing the evolution of the envelope below the K-edge thus becomes (see appendix B):

$$\frac{\partial \mathcal{E}_0}{\partial y} + \frac{1}{c}\frac{\partial \mathcal{E}_0}{\partial t} = -i\frac{2\pi N}{c\omega_0}\mathcal{P} \tag{5.2.7}$$

under the slowly varying envelope approximation [5, 39, 69]. Here N is the particle density and $\mathcal{P}$ the macroscopic polarization of the sample medium. The source term on the right hand side describes coupling to resonances and is connected to the system via the density matrix dependent formula:

$$\mathcal{P} = \sum_{i\neq j} \rho_{ij}\mathcal{T}_{ij}\omega_{ji}e^{i(\omega_{ji}-\omega_0)t} + \sum_{i\neq j} \rho^+_{ij}\mathcal{T}_{ij}\omega_{ji}e^{i(\omega_{ji}-\omega_0)t} \tag{5.2.8}$$

defining nonlinear polarization. Here i, j are composite indices describing atomic states. The atoms that are ionized due to the part of the X-ray pulse above the K-edge also evolve in the system, therefore contributing to the polarization, and thus, must be included in the above formula. Accordingly, ρ_{ij} are the components of the neutral atom and ρ^+_{ij} the components of the ionized atom density matrix, further, $\mathcal{T}_{ij}$ are the components of the transition operator corresponding to the transition $i \leftrightarrow j$. In this theory the transition operator can be either the dipole or the quadrupole operator, so far we have not made any separation between the two. The transition frequency is the difference of orbital energies $\omega_{ji} = \varepsilon_j - \varepsilon_i$. Now, everything we need to do, is to find out how the electric field evolves in the sample medium. In order to do this the exact form of the density matrix is required. Note, however, that in this section we only deal with the equations related to the primary process of interest, the SRIXS of the neutral atoms, even though we had to include

the density matrix of the ions, $\rho^{+}(t)$, into the above formula. The following section 5.2.2 will introduce the derivation of the ionic density matrix.

In order to find the form of the neutral atom density matrix $\rho(t)$ we are going to derive the master equations describing time evolution of the density matrix [5,69, 70,72–74]. First we must describe the atomic or molecular states within the sample system. Once again, we shall use configuration interactions method from section 2.2 for this purpose by expanding a general quantum state according to 2.2.9:

$$|\Psi(t)\rangle = \alpha_0(t)e^{-iE_0t}|\Phi_0\rangle + \sum_{i,a}\alpha_i^a(t)e^{-iE_i^at}|\Phi_i^a\rangle\,, \tag{5.2.9}$$

where we have introduced the time dependence in the standard way [26,75]. Since we are only going to look at single excitations we truncate the series as above. Moving into the interaction picture by using $|\Psi(t)\rangle_I = e^{i\hat{H}_0t}|\Psi(t)\rangle$ gives

$$|\Psi(t)\rangle_I = \alpha_0(t)|\Phi_0\rangle + \sum_{i,a}\alpha_i^a(t)|\Phi_i^a\rangle\,. \tag{5.2.10}$$

The Schrödinger equation in the interaction picture reads

$$i\frac{\partial}{\partial t}|\Psi(t)\rangle_I = \hat{H}_I(t)|\Psi(t)\rangle_I\,, \tag{5.2.11}$$

where the Hamiltonian operator 5.2.3 is transformed into the interaction picture in the usual way operators are transformed:

$$\hat{\mathcal{O}}_I = e^{i\hat{H}_0t}\hat{\mathcal{O}}e^{-i\hat{H}_0t}. \tag{5.2.12}$$

Thus, the form of the Schrödinger equation will be

$$i\frac{\partial}{\partial t}|\Psi(t)\rangle_I = e^{i\hat{H}_0t}\hat{H}_{int}e^{-i\hat{H}_0t}|\Psi(t)\rangle_I\,. \tag{5.2.13}$$

From now on we will work in the interaction picture but drop the subscript I. Plugging in the expansion 5.2.10 to the above equation yields

$$i\left(\dot{\alpha}_0(t)|\Phi_0\rangle + \sum_{i,a}\dot{\alpha}_i^a(t)|\Phi_i^a\rangle\right) = e^{i\hat{H}_0t}\hat{H}_{int}e^{-i\hat{H}_0t}\left(\alpha_0(t)|\Phi_0\rangle + \sum_{i,a}\alpha_i^a(t)|\Phi_i^a\rangle\right). \tag{5.2.14}$$

We are interested in the time evolution of the expansion coefficients $\alpha_i^a(t)$, so let us isolate the time derivatives by projecting this equation onto $\langle\Phi_0|$ and $\left\langle\Phi_j^b\right|$. This yields, in respective order,

$$\begin{aligned} i\dot{\alpha}_0(t) &= \alpha_0(t)\left\langle\Phi_0\right|\hat{H}_{int}\left|\Phi_0\right\rangle + \sum_{i,a}\alpha_i^a(t)e^{i\omega_{ia}t}\left\langle\Phi_0\right|\hat{H}_{int}\left|\Phi_i^a\right\rangle, \\ i\dot{\alpha}_j^b(t) &= \alpha_0(t)e^{i\omega_{bj}t}\left\langle\Phi_j^b\right|\hat{H}_{int}\left|\Phi_0\right\rangle + \sum_{i,a}\alpha_i^a(t)e^{i(E_j^b-E_i^a)t}\left\langle\Phi_j^b\right|\hat{H}_{int}\left|\Phi_i^a\right\rangle - i\frac{\Gamma_j}{2}\alpha_j^b(t), \end{aligned} \tag{5.2.15}$$

where $\omega_{ij} = \varepsilon_i - \varepsilon_j$ and $E_i^a = E_0 + \varepsilon_a - \varepsilon_i$ are calculated according to the section 2.2. Here we also introduced a phenomenological decay rate Γ_j to take into account the spontaneous decay of the core excited states j, for example via Auger decay [69,70].

Let us briefly turn our focus to the matrix elements containing the interaction Hamiltonian $\hat{H}_{int}$ in the above formulae. In order to calculate these, recall that the Hamiltonian 5.2.5 contains two separate interaction terms describing the dipole and quadrupole interactions, and that both of these terms contain a transition operator that can be written in second quantization as shown in the section 2.2:

$$\hat{\mathcal{T}} = \sum_{pq}\mathcal{T}_{pq}\hat{c}_p^\dagger\hat{c}_q, \quad \text{where} \quad \mathcal{T}_{pq} = \left\langle\varphi_p\right|\mathcal{T}\left|\varphi_q\right\rangle. \tag{5.2.16}$$

Then the matrix elements are calculated according to the principles presented in section 2.2 and [29]:

$$\begin{aligned} \left\langle\Phi_0\right|\hat{\mathcal{T}}\left|\Phi_0\right\rangle &= \sum_i \mathcal{T}_{ii}, \\ \left\langle\Phi_0\right|\hat{\mathcal{T}}\left|\Phi_i^a\right\rangle &= \mathcal{T}_{ia}, \\ \left\langle\Phi_j^b\right|\hat{\mathcal{T}}\left|\Phi_i^a\right\rangle &= \mathcal{T}_{ba}\delta_{ij} - \mathcal{T}_{ij}\delta_{ba} + \delta_{ba}\delta_{ij}\sum_k \mathcal{T}_{kk}. \end{aligned} \tag{5.2.17}$$

As explained earlier, we are trying to formulate a theory describing 1s2p SRIXS, where the XFEL pulse couples to quadrupole excitations and dipole de-excitations or emissions in our model system. Therefore, in order to capture this whole system within single theory, we must consider both dipole and quadrupole transitions. Let us, however, continue with the general transition operator $\mathcal{T}$ for now and replace the

appropriate operator in when necessary. Plugging the above results back into 5.2.15 and replacing the electric field dependent multiplicative coefficient in the interaction Hamiltonian with a generalized coefficient

$$E^{\mathcal{T}}(t) = \begin{cases} E(t), \text{ for dipole transitions, } \mathcal{T} = z \\ \frac{1}{2}E'(t), \text{ for quadrupole transitions, } \mathcal{T} = Q, \end{cases} \tag{5.2.18}$$

we obtain the generalized final form of the time evolution of the time dependent coefficients in the expansion 5.2.10. Note that here we denote $\partial_y E(t) = E'(t)$. Further, by ignoring transitions between virtual orbitals ($Q_{ab} = 0$) and transitions between same single particle orbitals, i.e. the term $\mathcal{T}_{kk}$ in 5.2.17, the equations 5.2.15 take the form:

$$\begin{aligned} \dot{\alpha}_0(t) &= -iE^{\mathcal{T}}(t) \sum_{i,a} \alpha_i^a(t) e^{i\omega_{ia}t} \mathcal{T}_{ia}, \\ \dot{\alpha}_i^a(t) &= -iE^{\mathcal{T}}(t) \left[\alpha_0(t) e^{i\omega_{ai}t} \mathcal{T}_{ai} - \sum_j \alpha_j^a(t) e^{i\omega_{ji}t} \mathcal{T}_{ji} \right] - \frac{\Gamma_i}{2} \alpha_i^a(t), \end{aligned} \tag{5.2.19}$$

So far out discussion has been on a very general level. We, however, need to describe atomic or molecular states more carefully than just with occupied and unoccupied orbitals in order to properly characterize the resonant excitations by X-ray field in the theory. To this end, let us define a new composite index describing atomic or molecular states so that one of these composite indices contains three indices describing an electronic state where an electron is excited from an orbital i to an orbital a forming a state with total angular momentum J. Denoting this index as J_i^a and applying this to the above formulae we obtain

$$\begin{aligned} \dot{\alpha}_0(t) &= -iE^{\mathcal{T}}(t) \sum_{i,a,J} \alpha_{J_i^a}(t) e^{i\omega_{ia}t} \mathcal{T}_{0,J_i^a}, \\ \dot{\alpha}_{J_i^a}(t) &= -iE^{\mathcal{T}}(t) \left[\alpha_0(t) e^{i\omega_{ai}t} \mathcal{T}_{J_i^a,0} - \sum_{j,J'} \alpha_{J_j^a}(t) e^{i\omega_{ji}t} \mathcal{T}_{J_i^a,J'^a_j} \right] - \frac{\Gamma_i}{2} \alpha_{J_i^a}(t). \end{aligned} \tag{5.2.20}$$

These equations capture the time evolution of the atomic or molecular states instead of the evolution of occupation or unoccupation of some single orbital.

At this point one could solve for $\alpha_{J_i^a}(t)$ directly from the above equations and obtain the time evolution of the states, but let us analyse the equations further by defining the elements of a truncated density matrix [29,43,70] of a Slater determinant for the states of the neutral atom in the new index system:

$$\rho_{J_i^a,K_j^b}(t) = \left|\Phi_{J_i^a}\right\rangle \left\langle\Phi_{J_j^b}\right| = \alpha_{J_i^a}(t)\alpha_{K_j^b}{}^*(t). \tag{5.2.21}$$

The diagonal density matrix elements describe the populations in the system of the neutral atoms, whereas the non-diagonal elements describe the coherences. Both are directly coupled to the evolution of the electric field in the sample, therefore the SRIXS process is also encoded in the evolution of these elements. The time derivative of the density matrix elements is given as

$$\dot{\rho}_{J_i^a,K_j^b}(t) = \dot{\alpha}_{J_i^a}(t)\alpha_{K_j^b}{}^*(t) + \alpha_{J_i^a}(t)\dot{\alpha}_{K_j^b}{}^*(t), \tag{5.2.22}$$

from which we quickly note that the time evolution of the diagonal elements can be written as separate equation:

$$\dot{\rho}_{J_i^a,J_i^a}(t) = 2\,\mathrm{Re}[\dot{\alpha}_{J_i^a}(t)\alpha_{J_i^a}{}^*(t)]. \tag{5.2.23}$$

Now we can plug in the equations 5.2.20 in order to obtain the time evolution equations for the density matrix elements. For instance, for the ground state we have:

$$\begin{aligned}\dot{\rho}_0 &= -2\,\mathrm{Im}\left[E^{\mathcal{T}}(t)\sum_{i,a,J}\alpha_{J_i^a}(t)e^{i\omega_{ia}t}\mathcal{T}_{0,J_i^a}\alpha_0^*(t)\right] \\ &= -2\,\mathrm{Im}\left[E^{\mathcal{T}}(t)\sum_{i,a,J}\rho_{J_i^a,0}(t)e^{i\omega_{ia}t}\mathcal{T}_{0,J_i^a}\right],\end{aligned} \tag{5.2.24}$$

where we reuse the definition of the density matrix elements 5.2.21. Now, in order to plug in the electric field $E^{\mathcal{T}}(t)$ explicitly, we must segregate between the two possible transitions. As explained earlier, in the 1s2p RIXS we assume that the excitations are due to quadrupole coupling. Therefore, as the ground state is depleted by

quadrupolar excitations to the d-shell, we plug in the the field derivative and invoke the rotating wave approximation, which yields

$$\begin{aligned}\dot{\rho}_0 &= -\operatorname{Im}\sum_{i,a,J}\rho_{J_i^a,0}(t)\mathcal{E}_0'(t,y)e^{i(\omega_{ia}-\omega_0)t}\mathcal{T}_{0,J_i^a}\\ &= -\operatorname{Im}\sum_{i,a,J}R^Q_{0,J_i^a}(t)\rho_{J_i^a,0}(t).\end{aligned} \tag{5.2.25}$$

Here we define the generalized Rabi frequencies:

$$R^{\mathcal{T}}_{ij}(t,y) = \begin{cases}\mathcal{E}_0'(t,y)e^{i(\omega_{ij}-\omega_0)t}Q_{ij}, & \text{when } \mathcal{T}=Q\\ \mathcal{E}_0(t,y)e^{i(\omega_{ij}-\omega_0)t}z_{ij}, & \text{when } \mathcal{T}=z.\end{cases} \tag{5.2.26}$$

In our experimental geometry the transition operators are explicitly written as:

$$\begin{aligned}z_{pq} &= \langle\varphi_p|\, z\,|\varphi_q\rangle = \int d\boldsymbol{x}\varphi_p(\boldsymbol{x})z\varphi_q(\boldsymbol{x}),\\ Q_{pq} &= \langle\varphi_p|\, yz\,|\varphi_q\rangle = \int d\boldsymbol{x}\varphi_p(\boldsymbol{x})yz\varphi_q(\boldsymbol{x}).\end{aligned} \tag{5.2.27}$$

Recalling the transitions we specified in 5.2.1, and checking which states are coupled to the ground state via quadrupole transition, we can write down the final equation for the evolution of the ground state population:

$$\dot{\rho}_0(t) = -\left[\sigma_{1s}J_a + \sigma_v(J_b+J_a)\right]\rho_0(t) - \operatorname{Im}\sum_n R^Q_{0,J^{nd}_{1s}}(t)\rho_{J^{nd}_{1s},0}(t), \tag{5.2.28}$$

where we denote $a = nd$ and $i = 1s$ according to the specified system of transitions. Notice, that here we have phenomenologically added an ionization term to the ground state equation describing the ionization of an electron from the 1s and valence orbitals to continuum with the cross sections σ_{1s} and σ_v, respectively, in order to take into account the depletion of ground state population via ionization. The valence ionization loss term takes into account all ionization channels above the 1s ionization. We shall discuss the ionized states more in depth and derive the ionization cross sections in the next section. Taking similar steps as above and carefully checking the correct transition types and couplings one can derive the remaining two

evolution equations of neutral atom populations:

$$\begin{aligned}\dot{\rho}_{J_{1s}^{nd},J_{1s}^{nd}}(t) =& -\Gamma\rho_{J_{1s}^{nd},J_{1s}^{nd}}(t) - \mathrm{Im}\left(R^{Q}_{J_{1s}^{nd},0}(t)\rho_{0,J_{1s}^{nd}}(t) - 2\sum_{J'} R^{z}_{J_{1s}^{nd},J_{2p}^{\prime nd}}(t)\rho_{J_{1s}^{\prime nd},J_{1s}^{nd}}(t)\right)\\ \dot{\rho}_{J_{2p}^{nd},J_{2p}^{nd}}(t) =& -2\,\mathrm{Im}\,R^{z}_{J_{2p}^{nd},K_{1s}^{nd}}(t)\rho_{K_{1s}^{nd},J_{2p}^{nd}}(t).\end{aligned} \tag{5.2.29}$$

Note, that we have not defined a sum convention here: All appearing sums are explicitly written down. Therefore, K is the specific angular momentum of the $1s^1nd^{m+1}$ excited state, not a sum or an arbitrary value.

Let us next derive the time evolution of the non-diagonal components of the density matrix describing the coherences in the system. By plugging in 5.2.20 to the time derivative equation 5.2.22 and using the definition of the density matrix elements we obtain

$$\begin{aligned}\dot{\rho}_{J_i^a,0}(t) =& -iE^{\mathcal{T}}(t)\left[\rho_0(t)e^{i\omega_{ai}t}\mathcal{T}_{J_i^a,0} - \sum_{j,J'}\rho_{J'^a_j,0}(t)e^{i\omega_{ji}t}\mathcal{T}_{J_i^a,J'^a_j}\right]\\ &-\frac{\Gamma_i}{2}\rho_{J_i^a,0}(t) + iE^{\mathcal{T}}(t)\sum_{j,b,J'}\rho_{J_i^a,J_j'^b}(t)e^{i\omega_{bj}t}\mathcal{T}_{J_j'^b,0}.\end{aligned} \tag{5.2.30}$$

Similar to before, we plug in the electric field 5.2.6, invoke the rotating wave approximation and use the definition of the generalized Rabi frequencies to obtain:

$$\begin{aligned}\dot{\rho}_{J_i^a,0}(t) =& -\frac{\Gamma_i}{2}\rho_{J_i^a,0}(t) - iR^{\mathcal{T}}_{J_i^a,0}(t)\rho_0(t) + i\sum_{j,J'}R^{\mathcal{T}}_{J_i^a,J'^a_j}(t)\rho_{J'^a_j,0}(t)\\ &+ i\sum_{j,b,J'}R^{\mathcal{T}}_{J_j'^b,0}(t)\rho_{J_i^a,J_j'^b}(t).\end{aligned} \tag{5.2.31}$$

Again, by denoting $a = nd$ and $i = 1s$ plus checking the specified system for the correct couplings of the states one obtains

$$\begin{aligned}\dot{\rho}_{J_{1s}^{nd},0}(t) =& -\frac{1}{2}\left[\Gamma + \sigma_{1s}J_a\right]\rho_{J_{1s}^{nd},0}(t) - \frac{i}{2}R^{Q}_{J_{1s}^{nd},0}(t)\rho_0(t)\\ &+ i\sum_{J'}R^{z}_{J_{1s}^{nd},J_{2p}^{\prime nd}}(t)\rho_{J_{2p}^{\prime nd},0}(t) + \frac{i}{2}\sum_{n}R^{Q}_{J_{1s}^{nd},0}(t)\rho_{J_{1s}^{nd},J_{1s}^{nd}}(t),\end{aligned} \tag{5.2.32}$$

where we have again added the ionization loss term. Repeating the preceding calcu-

lations for the rest of the coherences one ends up with the following set of equations:

$$\begin{aligned}
\dot{\rho}_{J_{1s}^{nd},K_{2p}^{n'd}}(t) =& -\Gamma\rho_{J_{1s}^{nd},K_{2p}^{n'd}}(t) - \frac{i}{2}R^{Q}_{J_{1s}^{nd},0}(t)\rho_{0,K_{2p}^{n'd}}(t) \\
&+ i\sum_{J'} R^{z}_{J_{1s}^{nd},J'^{nd}_{2p}}(t)\rho_{J'^{nd}_{2p},K_{2p}^{n'd}}(t) + iR^{z}_{J_{1s}^{n'd},K_{2p}^{n'd}}(t)\rho_{J_{1s}^{nd},K_{1s}^{n'd}}(t), \\
\dot{\rho}_{J_{1s}^{nd},J_{1s}^{n'd}}(t) =& -\Gamma\rho_{J_{1s}^{nd},J_{1s}^{n'd}}(t) - \frac{i}{2}R^{Q}_{J_{1s}^{nd},0}(t)\rho_{0,J_{1s}^{n'd}}(t) + \frac{i}{2}R^{Q}_{0,J_{1s}^{n'd}}(t)\rho_{J_{1s}^{nd},0}(t) \\
&+ i\sum_{J'} R^{z}_{J_{1s}^{nd},J'^{nd}_{2p}}(t)\rho_{J'^{nd}_{2p},J_{1s}^{n'd}}(t) - i\sum_{J'} R^{z}_{J'^{n'd}_{2p},J_{1s}^{n'd}}(t)\rho_{J_{1s}^{nd},J'^{n'd}_{2p}}(t), \\
\dot{\rho}_{J_{2p}^{nd},J'^{n'd}_{2p}}(t) =& \, iR^{z}_{J_{2p}^{nd},K_{1s}^{nd}}(t)\rho_{K_{1s}^{nd},J'^{n'd}_{2p}}(t) + iR^{z}_{K_{1s}^{n'd},J'^{n'd}_{2p}}(t)\rho_{J_{2p}^{nd},K_{1s}^{n'd}}(t).
\end{aligned} \tag{5.2.33}$$

Together with the equation 5.2.32 these equations define the time evolution of the coherences of the neutral atoms or molecules in the system. Let us next take a look at the competing processes and the evolution of ionic density matrix.

5.2.2 Competing processes

We have now derived the equations describing the actual RIXS process, but as mentioned, there are multiple competing processes as due to the relatively wide band gap of the SASE pulse. We shall address these competing processes here. As explained earlier, the X-ray flux is divided into two parts, the one above the K-edge J_a and the one below J_b. Both of these parts cause competing processes, one of the most notable being the 1s core ionization of the atoms or molecules in the sample due to the part above the K-edge, and the subsequent evolution of the ions due to the part below. There are other ionization channels too but we shall assume that they won't give rise to a population significant enough to merit a whole time evolution analysis and are only incorporated into the theory as loss terms similarly as before. Further, these ionization channels won't give rise to the filling of a 1s core hole, and therefore the emission of a photon in the energy region we are interested in.

Before moving on to the mathematical derivations explained above, let us mention another obvious and important competing process due to the below K-edge

part of the flux, which is of course, the dipole RIXS process, which is actually always stronger over the quadrupolar RIXS. We shall, however, not write down the equations for this process, since it can be easily incorporated into the theory by performing calculations analogous to the previous section and simply interchanging the quadrupole transitions for the dipole counterparts, which should be easy in the presented generalized formalism. Dipole transitions are considered more carefully for example in [69]. If we were going to do simulations, or especially experiments, we would have to include the dipole transitions in order to obtain reasonable results, but for now, we will acquiesce with stating that generally quadrupole transitions are some twenty to hundred times weaker than dipole transitions [48]. Since the theories for describing the different transitions are analogous, we expect the spectral features from the different transitions to have the same relative intensities as their corresponding transition strengths. Therefore comparing transition dipole and quadrupole elements 5.2.27 should yield some quantitative information about the expected ratio between the spectral intensities of the corresponding features. As current XFELs offer no possibility of discriminating between the two transitions via extremely accurate energy selection, one is most likely forced to consider the dipole transitions as a competing process when ever considering the quadrupole RIXS. There are also experimental methods to improve the detection of quadrupole transitions utilizing the geometry of the sample, polarization etc. [47, 48, 76].

Here we shall consider the 1s ionization and subsequent time evolution of the singly core ionized atoms in the model system, giving the possibility to estimate the influence of the filling of the core hole according to 5.2.2 on the final spectrum. We will show how to derive the ionization cross sections within our theoretical framework, notice however, that the evolution of the ionic density matrix elements is due to the part of electric field flux below the K-edge and that the electric field associated with that evolution is governed by the familiar equation 5.2.7. The polarization

5.2.8 in the wave equation evolves due to the neutral atoms as shown in the previous section whereas the evolution due to ions is covered in the following. The part of the electric field flux above the K-edge is fully governed by

$$\frac{\partial J_a(t)}{\partial y} = -\rho_0(t) N \sigma_{tot} J_a(t), \tag{5.2.34}$$

where N is the particle density and σ_{tot} is the total photoionization cross section. This equation is only connected to the rest of the equations via the ground state population and describes the attenuation of the the flux due to photoabsorption.

The analysis of the evolution of density matrix elements is similar to what we did before, apart from the definition of the density matrix elements. This time we shall start out by defining the reduced density matrix $\rho^+(t)$ for the ions [43, 69, 77]:

$$\rho^+_{J_i,K_j}(t) = \sum_a \alpha_{J_i^a}(t) {\alpha_{K_j^a}}^*(t), \tag{5.2.35}$$

where the index of the occupied virtual orbital disappears as we are describing excitations to the continuum. The time derivative is given by

$$\dot{\rho}^+_{J_i,K_j}(t) = \sum_a \dot{\alpha}_{J_i^a}(t) {\alpha_{K_j^a}}^*(t) + \alpha_{J_i^a}(t) {\dot{\alpha}_{K_j^a}}^*(t). \tag{5.2.36}$$

First focusing on the diagonal elements, we notice again that the above time derivative can be written as

$$\dot{\rho}^+_{J_i,J_i}(t) = 2 \sum_a \mathrm{Re}[\dot{\alpha}_{J_i^a}(t) {\alpha_{J_i^a}}^*(t)]. \tag{5.2.37}$$

Notice, that since we are interested in the densities of ionic states, the relevance of the orbital where the electron ends up after excitation, or ionization, disappears. Therefore, we can simplify the theory a bit by investigating hole densities rather than the densities of states labelled with the composite index J_i^a. Thus, we can now plug in the time derivatives 5.2.19 and treat the indices as hole identifiers in order to obtain the evolution equation for the diagonal density matrix elements. Let us

derive the evolution of singly 1s-ionized atoms for example:

$$\begin{aligned}\dot{\rho}^{+}_{1s,1s}(t) = &-2\,\mathrm{Im}\sum_a E^{\mathcal{T}}(t)\left[\alpha_0(t)e^{i\omega_{a,1s}t}\mathcal{T}_{a,1s} - \sum_j \alpha^a_j(t)e^{i\omega_{j,1s}t}\mathcal{T}_{1s,j}\right]\alpha^{a\,*}_{1s}(t)\\ &-\Gamma_{1s}\sum_a \alpha^a_{1s}(t)\alpha^{a\,*}_{1s}(t).\end{aligned} \tag{5.2.38}$$

By using the definition of the reduced density matrix elements and doing some simple manipulations we obtain

$$\begin{aligned}\dot{\rho}^{+}_{1s,1s}(t) = &-2\,\mathrm{Im}\sum_a E(t)\alpha_0(t)\alpha^{a\,*}_{1s}(t)e^{i\omega_{a,1s}t}\mathcal{T}_{a,1s}\\ &-\Gamma_{1s}\rho^{+}_{1s,1s}(t) + 2\,\mathrm{Im}\sum_j R^{z}_{1s,j}(t)\rho^{+}_{j,1s}(t),\end{aligned} \tag{5.2.39}$$

where we use the definition of the generalized Rabi frequencies 5.2.26 again. Notice that we are only dealing with dipole coupling here. Now the second line is in the final form coherent with the earlier formulae, whereas the first row needs some manipulations in order to take the final form describing the 1s-ionization.

Let us show that the first term in the above reduces to the 1s-ionization cross section. The term is somewhat tricky since it contains the time dependent expansion coefficients $\alpha^a_{1s}(t)$ and $\alpha_0(t)$ plus other terms depending on the virtual orbital a, therefore it cannot simply be reduced by some definition as we have done so far. We can, however, rewrite the time dependent coefficient $\alpha^a_{1s}(t)$ by formally solving it from the second equation in 5.2.19, from which we obtain by integration:

$$\alpha^{a\,*}_{1s}(t) = i\int_{-\infty}^{t} dt' e^{\frac{\Gamma_{1s}}{2}(t'-t)}E(t')\left(\alpha^*_0(t')e^{i\omega_{1s,a}t'}z_{1s,a} - \sum_j \alpha^{a*}_j(t')e^{i\omega_{1s,j}t'}z_{1s,j}\right). \tag{5.2.40}$$

Plugging this into the first term in 5.2.39 yields

$$\begin{aligned}2\,\mathrm{Re}\Bigg[E(t)\alpha_0(t)\sum_a e^{i\omega_{a,1s}t}z_{a,1s}\int_{-\infty}^{t} dt' e^{\frac{\Gamma_{1s}}{2}(t'-t)}E(t')\\ \times\left(\alpha^*_0(t')e^{i\omega_{1s,a}t'}z_{1s,a} - \sum_j \alpha^{a*}_j(t')e^{i\omega_{1s,j}t'}z_{1s,j}\right)\Bigg],\end{aligned} \tag{5.2.41}$$

where a similar $\alpha^a_j(t)^*$ term appears again. This last term however produces a rapidly oscillating contribution to the absorption rate as the sum $\sum_a$ extends over

the continuum. Such fast oscillating terms can be neglected here as they are blurred out by the characteristic time scale of the ionization time evolution anyhow [70]. Discarding the last term and plugging in the electric field 5.2.6 plus invoking the rotating wave approximation gives

$$\mathrm{Re}\left[E(t)\alpha_0(t)\sum_a |z_{a,1s}|^2 \int_{-\infty}^{t} dt' \mathcal{E}(t')\alpha_0^*(t') e^{\frac{\Gamma_{1s}}{2}(t'-t)} e^{i\omega_{1s,a}(t'-t)} e^{-i\omega_0 t'}\right]. \tag{5.2.42}$$

Here a non-trivial integral over time appears where the integrand contains a function with no definite form multiplied by an exponential – there is a work around however. The sum over a in front of the integral sums over the exponential term of form $\exp[i\omega_{1s,a}(t'-t)]$ in the integral. If we assume that the a dependent coefficients $|z_{a,1s}|^2$ are nearly constant, which is reasonable at high ω_0, the sum over the exponential can be viewed as an effective Dirac delta function with respect to $(t'-t)$ [70] centering the contribution of the integral strongly around $t'=t$. Consequently, we evaluate $\mathcal{E}(t')\alpha_0^*(t')$ at $t'=t$ and extract it out of the integral. The rest of the integral can now be computed regularly:

$$\begin{aligned} &2\,\mathrm{Re}\left[E(t)|\alpha_0(t)|^2 \sum_a |z_{a,1s}|^2 \mathcal{E}(t) e^{-i\omega_0 t} \int_{-\infty}^{t} dt' e^{\frac{\Gamma_{1s}}{2}(t'-t)} e^{i\omega_{1s,a}(t'-t)} e^{-i\omega_0(t'-t)}\right] \\ &= 2\,\mathrm{Re}\left[E(t)\rho_0(t)\sum_a |z_{a,1s}|^2 \frac{\mathcal{E}(t)e^{-i\omega_0 t}}{i(\omega_{1s,a}-\omega_0)+\frac{\Gamma_{1s}}{2}}\right], \end{aligned} \tag{5.2.43}$$

where we use the definition of the neutral atom density matrix 5.2.21 to write $\rho_0(t)$. Next we plug in the electric field 5.2.6 for the remaining $E(t)$, take the real part of the result and average over the period of the radiation field $(2\pi/\omega_0)$ yielding

$$\rho_0(t)\mathcal{E}^2(t)\sum_a |z_{a,1s}|^2 \frac{\frac{\Gamma_{1s}}{2}}{(\omega_{1s,a}-\omega_0)^2+\frac{\Gamma_{1s}^2}{4}}. \tag{5.2.44}$$

This is not yet a very informative result, at least intuitively. We can rewrite the Lorentzian (or Cauchy) distribution in the sum as a Dirac delta [50], in the limit of very small Auger core hole life times Γ_{1s}:

$$\delta(x-x_0) = \lim_{\epsilon\to 0}\frac{1}{\pi}\frac{\epsilon}{(x-x_0)^2+\epsilon^2}. \tag{5.2.45}$$

Therefore, according to standard scattering theory [26, 31], we identify the sum as the total 1s photoionization cross section. By writing the square of electric field in terms of the flux of the field and plugging this result back into 5.2.39 along with correct constants we finally obtain:

$$\dot{\rho}^{+}_{1s,1s}(t) = \sigma_{1s}(\omega_0) J_a \rho_0(t) - \Gamma_{1s}\rho^{+}_{1s,1s}(t) + 2\,\mathrm{Im}\sum_j R^{z}_{1s,j}(t)\rho^{+}_{j,1s}(t), \tag{5.2.46}$$

where the cycle averaged flux is given by

$$J(t) = \frac{c}{8\pi\omega_0}\mathcal{E}^2(t). \tag{5.2.47}$$

Note, that in here the ionization is a source term and that only the flux above K-edge produces 1s core ionized ions. Via analogous steps one derives the equation for the 2p ionized atom:

$$\dot{\rho}^{+}_{2p,2p}(t) = \sigma_{2p}(\omega_0)\left[J_a + J_b\right]\rho_0(t) + 2\,\mathrm{Im}\, R^{z}_{1s,2p}(t)\rho^{+}_{2p,1s}(t). \tag{5.2.48}$$

Here both parts of the flux can ionize as 2p ionization can occur at energies below K-edge too.

Let us next derive the evolution equation for coherences between 1s and 2p ionized atoms for completeness. The general time evolution of the ions is given by 5.2.36 which, by plugging in the time derivatives from 5.2.19, yields

$$\begin{aligned}\dot{\rho}^{+}_{1s,2p}(t) = &-\frac{\Gamma_{1s}}{2}\rho^{+}_{1s,2p}(t) + iE(t)\left[\sum_j \rho^{+}_{j,2p}(t)e^{i\omega_{j,1s}t}\mathcal{T}_{1s,j} - \sum_k \rho^{+}_{1s,k}(t)e^{-i\omega_{k,2p}t}\mathcal{T}_{2p,k}\right] \\ &- iE(t)\sum_a\left[\alpha_0(t)\alpha^{a}_{2p}{}^{*}(t)e^{i\omega_{a,1s}t}\mathcal{T}_{a,1s} - \alpha^{a}_{1s}(t)E(t)\alpha_0(t)e^{i\omega_{a,2p}t}\mathcal{T}_{k,2p}\right]\end{aligned} \tag{5.2.49}$$

after minor rearrangement and the usage of the definition 5.2.35 on the first line. Now we have a similar situation as before with the terms on the second line. Applying similar steps as above with $\rho^{+}_{1s,1s}(t)$ would, however, yield an oscillatory ionization cross section term with $\exp(i\omega_{1s,2p}t)$ dependence that would average out over the period of radiation. Thus, let us not waste our breath deriving these terms but

simply drop them straight away. Inserting the definition of the electric field 5.2.6 and invoking the rotating wave approximation once more allows us to rewrite the remaining equation in its final form in terms of Rabi frequencies 5.2.26:

$$\dot{\rho}^{+}_{1s,2p}(t) = -\frac{\Gamma_{1s}}{2}\rho^{+}_{1s,1p}(t) + i\sum_{j} R^{z}_{1s,j}(t)\rho^{+}_{j,2p}(t) - iR^{z}_{1s,2p}(t)\rho^{+}_{1s,1s}(t). \tag{5.2.50}$$

This concludes our derivation of the time evolution equations for the density matrices or Liouville-von Neumann equations for SRIXS, next, we will take a closer look at what we derived and what do these results mean.

5.2.3 Synopsis

The preceding two sections were full on derivation containing an overwhelming amount of formulae and results, therefore, let us next collect all the actual results together and try to give some intuitive explanation on their physical interpretation. We shall also discuss solving the equations shortly.

The ultimate goal of the theory is to predict the evolution of the electric field in the sample medium, thus enabling predicting spectra obtained by SRIXS. Electric field evolution is generally governed by the wave equation. In the beginning, however, the electric field flux was divided into two parts, the part above the K-edge J_a and the part below J_b, therefore, two equations were presented governing the evolution of the two parts, respectively:

$$\frac{\partial J_a(t)}{\partial y} = -\rho_0(t) N \sigma_{tot} J_a(t), \tag{5.2.51}$$

$$\frac{\partial \mathcal{E}_0}{\partial y} + \frac{1}{c}\frac{\partial \mathcal{E}_0}{\partial t} = -i\frac{2\pi N}{c\omega_0}\mathcal{P}. \tag{5.2.52}$$

The first equation simply describes the attenuation of the electric field flux J_a due to photoabsorption in the sample. Note that only the ground state population is assumed to be relevant here since it is practically the only population in the beginning and only single ionizations are considered here. The second equation

governs the evolution of the electric field below the K-edge. It is the result of applying slowly varying envelope approximation to the general wave equation (see appendix B). The first equation is directly coupled to the sample via the ground state population $\rho_0(t)$, whereas in the second equation the coupling is hidden in the polarization, defined here as:

$$\mathcal{P} = \sum_{i \neq j} \rho_{ij} \mathcal{T}_{ij} \omega_{ji} e^{i(\omega_{ji} - \omega_0)t} + \sum_{i \neq j} \rho^+_{ij} \mathcal{T}_{ij} \omega_{ji} e^{i(\omega_{ji} - \omega_0)t}. \tag{5.2.53}$$

Now, in order to solve for the electric field, and therefore the spectrum, from the equations 5.2.51 and 5.2.52 as the XFEL pulse passes through the sample, one needs to know how $\rho_{ij}(t)$ and $\rho^+_{ij}(t)$ evolve in time. Deriving this time evolution was the most important content of the previous two sections. Let us see the results of that derivation next.

We first derived the time evolution of the neutral atoms in the sample in the section 5.2.1. This derivation resulted in two sets of equations, one describing the evolution of populations (the diagonal elements of the density matrix) of states in neutral atoms, and one describing the evolution of coherences (off-diagonal elements). For population we obtained

$$\begin{aligned}
\dot{\rho}_0(t) =& -\left[\sigma_{1s} J_a + \sigma_v (J_b + J_a)\right] \rho_0(t) - \mathrm{Im} \sum_n R^Q_{0, J^{nd}_{1s}}(t) \rho_{J^{nd}_{1s}, 0}(t), \\
\dot{\rho}_{J^{nd}_{1s}, J^{nd}_{1s}}(t) =& -\Gamma_{1s} \rho_{J^{nd}_{1s}, J^{nd}_{1s}}(t) - \mathrm{Im} \left(R^Q_{J^{nd}_{1s}, 0}(t) \rho_{0, J^{nd}_{1s}}(t) - 2 \sum_{J'} R^z_{J^{nd}_{1s}, J'^{nd}_{2p}}(t) \rho_{J'^{nd}_{1s}, J^{nd}_{1s}}(t) \right), \\
\dot{\rho}_{J^{nd}_{2p}, J^{nd}_{2p}}(t) =& -2\, \mathrm{Im}\, R^z_{J^{nd}_{2p}, K^{nd}_{1s}}(t) \rho_{K^{nd}_{1s}, J^{nd}_{2p}}(t).
\end{aligned} \tag{5.2.54}$$

These three equations tell us how the populations of the respective states evolve as the electric field interacts with the matter. Most of the terms here are not fully intuitively interpretable to the naked eye as many of them depend on coherences, and are therefore the result of complicated processes. We can, however, easily see how the 1s and valence ionizations deplete the ground state in the first term of the first equation, and that on the second line the first term describes losses due to

spontaneous, irrelevant de-excitations, such as Auger decay. As far as interpreting the rest of the terms goes, the Rabi frequency $R^{\mathcal{T}}_{ij}(t)$ (see 5.2.26) contains a transition operator, therefore, the indices of the Rabi frequency reveal the coupling which contribution to the population the term describes. In order to solve this set of equations one needs to know about the evolution of the coherences. To that end, we derived the following set of equations describing coherences:

$$
\begin{aligned}
\dot{\rho}_{J^{nd}_{1s},0}(t) =& -\frac{1}{2}\left[\Gamma_{1s}+\sigma_{1s}J_a\right]\rho_{J^{nd}_{1s},0}(t) - \frac{i}{2}R^{Q}_{J^{nd}_{1s},0}(t)\rho_0(t) \\
&+ i\sum_{J'} R^{z}_{J^{nd}_{1s},J'^{nd}_{2p}}(t)\rho_{J'^{nd}_{2p},0}(t) + \frac{i}{2}\sum_{n} R^{Q}_{J^{nd}_{1s},0}(t)\rho_{J^{nd}_{1s},J^{nd}_{1s}}(t), \\
\dot{\rho}_{J^{nd}_{1s},K^{n'd}_{2p}}(t) =& -\Gamma_{1s}\rho_{J^{nd}_{1s},K^{n'd}_{2p}}(t) - \frac{i}{2}R^{Q}_{J^{nd}_{1s},0}(t)\rho_{0,K^{n'd}_{2p}}(t) \\
&+ i\sum_{J'} R^{z}_{J^{nd}_{1s},J'^{nd}_{2p}}(t)\rho_{J'^{nd}_{2p},K^{n'd}_{2p}}(t) + iR^{z}_{J^{n'd}_{1s},K^{n'd}_{2p}}(t)\rho_{J^{nd}_{1s},K^{n'd}_{1s}}(t), \qquad (5.2.55) \\
\dot{\rho}_{J^{nd}_{1s},J^{n'd}_{1s}}(t) =& -\Gamma_{1s}\rho_{J^{nd}_{1s},J^{n'd}_{1s}}(t) - \frac{i}{2}R^{Q}_{J^{nd}_{1s},0}(t)\rho_{0,J^{n'd}_{1s}}(t) + \frac{i}{2}R^{Q}_{0,J^{n'd}_{1s}}(t)\rho_{J^{nd}_{1s},0}(t) \\
&+ i\sum_{J'} R^{z}_{J^{nd}_{1s},J'^{nd}_{2p}}(t)\rho_{J'^{nd}_{2p},J^{n'd}_{1s}}(t) - i\sum_{J'} R^{z}_{J'^{n'd}_{2p},J^{n'd}_{1s}}(t)\rho_{J^{nd}_{1s},J'^{n'd}_{2p}}(t), \\
\dot{\rho}_{J^{nd}_{2p},J'^{n'd}_{2p}}(t) =& \, iR^{z}_{J^{nd}_{2p},K^{nd}_{1s}}(t)\rho_{K^{nd}_{1s},J'^{n'd}_{2p}}(t) + iR^{z}_{K^{n'd}_{1s},J'^{n'd}_{2p}}(t)\rho_{J^{nd}_{2p},K^{n'd}_{1s}}(t).
\end{aligned}
$$

The same description as above pretty much applies here too. We have three de-excitation loss terms with Γ_{1s} in the first three equations and one ionization loss term due to 1s ionization in the first equation. The rest of the terms are contributions from photoinduced couplings between the states and form rather complicated dynamics for the system. The equations 5.2.54 and 5.2.55 effectively contain the information about the SRIXS process.

As explained before, we did not include the fully dipolar RIXS to our model this time, but did however take into account for the stimulated fluorescence from the singly 1s ionized atoms. This is an important competing process as it causes the emission of photons in the same frequency domain as the actual SRIXS process we are interested in. Luckily, the ions have considerably fewer, less complicated states

than the neutral atoms, therefore evolving according to

$$\begin{aligned}
\dot{\rho}^+_{1s,1s}(t) &= \sigma_{1s} J_a \rho_0(t) - \Gamma_{1s}\rho^+_{1s,1s}(t) + 2\,\mathrm{Im}\sum_j R^z_{1s,j}(t)\rho^+_{j,1s}(t), \\
\dot{\rho}^+_{2p,2p}(t) &= \sigma_{2p}\left[J_a + J_b\right]\rho_0(t) - 2\,\mathrm{Im}\, R^z_{1s,2p}(t)\rho^+_{2p,1s}(t), \\
\dot{\rho}^+_{1s,2p}(t) &= -\frac{\Gamma_{1s}}{2}\rho^+_{1s,2p}(t) + i\sum_j R^z_{1s,j}(t)\rho^+_{j,2p}(t) - iR^z_{1s,2p}(t)\rho^+_{1s,1s}(t).
\end{aligned} \tag{5.2.56}$$

Here the first two equations describe the evolution of the populations and the last the coherences between the states. Note that due to the splitting of the 2p orbital to $2p_{1/2}$ and $2p_{3/2}$ the index $2p$ here contains both of these cases. Similar to before we identify the ionization and de-excitation loss terms here.

As one can easily see the equations collected here are not solvable by pen and paper, thus, in order to solve the emitted electric field after the sample we have to resort to a numerical solution. This is, however, beyond the scope of this theoretical review, but let us quickly describe the idea. In principle obtaining a solution is straightforward. The equations are solved step by step in a simulation-like method where each time step advances the position within the sample at the speed of light. The density matrices $\rho(t)$ and $\rho^+(t)$ are solved from the equations 5.2.54, 5.2.55 and 5.2.56 in every step and the electric field is updated according to 5.2.51 and 5.2.52. The initial electric field, i.e. the SASE pulse, is modeled as chaotic noise with gaussian statistics [78, 79], whereas the density matrices initially only display ground state population, i.e. $\rho_0 = 1$ and all other elements are zero including all the elements of $\rho^+(t)$.

5.3 Experimental overview

We have described traditional RIXS experiments in the section 4.2, and that gives a nice reference of a typical spectroscopical experimental setting, but SRIXS experiments are somewhat different. Thus, we shall give a quick overview on some aspects of the stimulated RIXS experiment in the light of the previous sections. While dis-

cussing the X-ray sources, we have shortly described an X-ray free electron lasers in the section 4.2.2, where it was explained that XFELs produce extremely intense X-ray pulses using SASE and that the spectrum of such a source resembles chaotic noise. In the section 5.1.1 it was mentioned that this complicates the experiments somewhat, and here we shall attend to that problem by introducing a couple of possible solutions. The obvious solution relies on developing better XFELs capable of producing tunable, stable and reproducible pulses, preferably with some predictable lineshape. Such devices should be able to control pulse duration, frequency and delay between pulses, further, it would be convenient to be able to control relative phases between pulses [6, 22]. One can rather confidently say that such devices are just a matter of time since in the extreme ultraviolet range seeded FELs have demonstrated these qualities [80, 81]. As we know, however, the current XFELs produce radiation through SASE and the qualities are far from this. The radiation is coherent in the transverse direction but not in the longitudinal, in other words, the level of spatial coherence can be high but the temporal and spectral coherence is low [6, 53]. The spiky random structure in spectral and temporal domains is

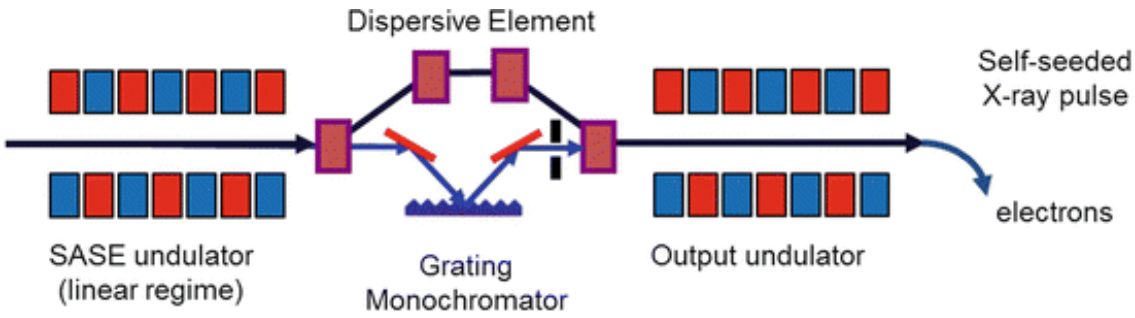

Figure 5.3: Schematic of a self-seeded SASE. The first undulator from the left produces a standard SASE pulse. The electrons and the radiation are separated and the radiation is monochromatized. The monochromatized beam will act as a seed for the SASE as the electrons and the beam are guided to the second undulator producing a high intensity narrow band X-ray spectrum. Adapted here from [82] with the permission from Springer.

demonstrated in the figure 4.6 in section 4.2.2. Recent advancements include methods for producing a couple of pulses with somewhat tunable separation and reducing the number of intensity spikes considerably [83, 84], these pulses nevertheless have at least an underlying SASE structure and are not reproducible. Self-seeded SASE is a likely candidate to resolve all of these issues in the future [85]. We shall not delve into this concept beyond the illuminating schematic 5.3 where the principle of two undulators and monochromatizing the X-ray beam while separated from the electrons is presented. Such a device would be able to deliver considerably more convenient pulse properties.

Along with the randomness of the SASE spectrum the absence of reproducibility is also a large complication in XFEL based spectroscopy. This leads us to the second solution of the SASE problem. A solution that is already at hand and can be used with the current XFELs relies on statistics and careful data analysis. By looking at the XFEL spectra 4.6 one might quickly think that it is impossible to obtain spectroscopic data with such a source. Throw in the fact that the pulses cannot be reproduced and despair is not far. It turns out, however, that high quality spectra can be obtained with XFEL radiation. The spiky structure of the XFEL spectrum is utilized in the sense that each of the intensity peaks can be thought as a narrow band pulse driving a scattering process, since peaks are narrow, high resolution is achieve in a statistical sense. Even though the band width of the spectrum of the whole pulse covers all the transition energies as depicted in 5.1.1 (c), a single SASE shot can be thought as bunch of narrow band pulses at separate energies. Performing covariance analysis [86] over a large set of recorded spectra a high resolution spectrum, analogous to narrow band source spectrum, can be obtained [5,69]. The resolution of the final spectrum is then determined by the peak width of the SASE spectrum. This method obviously requires that a large number of spectra are recorded, it is however, not a problem since current XFELs already have repetition

rates of dozens of hertz [23, 52]. This shows that current XFELs can be used for at least simple SRIXS experiments and encourages to invest more effort in developing data analysis tools.

The experimental setup of a currently realizable SRIXS experiment itself is rather straightforward. As explained in 5.2, the SRIXS experiment is assumed one dimensional, unlike traditional RIXS experiment, because of the population inversion channel required for the amplification by stimulation. Therefore the experimental scheme resembles more an X-ray absorption experiment than a traditional RIXS setup: The XFEL pulse is focused into the sample and the spectrometer is placed behind the sample straight on the beam path. In the experiment [23] a flat-field grazing incidence spectrometer with an X-ray CCD detector was used. The SRIXS spectrum of a single shot is recorded as the difference of the incoming and transmitted X-ray spectra, thus, X-ray optics for measuring the incoming and transmitted spectra at the same time would facilitate faster, more accurate measurements, but is not mandatory [23]. Such beam splitter would be placed between the source and the sample so that a part of the incoming beam could be diverted to second spectrometer separate from the one behind the sample.

5.3.1 Potential first samples

Even though this is work describes stimulated RIXS in a very general level, it is always illuminating to introduce possible samples and speculate on the additional information the method at hand could yield. Of course, one must immediately recognise the fact that the first experiment performed should, and will, be a proof of concept type measurement with no aim of extracting actual useful scientific data. This type of experiment could, for instance, focus on detecting the weak quadrupole pre-K-edge 1s-3d resonance in atomic neon instead of dipole transition [23, 69]. This would encourage more complicated experiments and the evolution on to transition

metals where quadrupole transitions act as a direct probe of the 3d valence orbitals in the hard X-ray range. Let us quickly review few realistic, relatively simple examples of types of transition metal samples where SRIXS utilizing quadrupole transitions could yield useful complementary information to traditional methods.

Strongly correlated materials exhibit numerous interesting and useful properties, such as high temperature superconductivity, colossal magnetoresistance and metal-insulator transitions, that still lack a detailed explanation. Many transition metal oxides fall into this class of materials and are therefore under intense research. A useful method for investigating the valence energy levels of these materials are the dd-excitations, which are sensitive to the local coordination. These excitations change only the occupation of the 3d orbital and can be directly investigated via soft X-ray techniques, such as RIXS or X-ray absorption spectroscopy [87], using the L-edge and nearby dipole allowed resonances, or via hard X-rays using the K-edge and the 1s-3d quadrupolar transitions. Soft X-ray spectra are loaded with information due to strong 2p-3d interaction causing multiplet effects and thus also complicated to analyze. Furthermore, bulk sensitivity, better resolution and better penetration make hard X-rays a candidate worth considering for such studies, even though K-edge resonances are relatively weaker. In [47] Huotari et al. consider dd-excitations utilizing hard X-ray RIXS on Ni K-edge in NiO discovering strong quadrupole character of the pre-peak and accurately determining the crystal field parameters of the electronic structure using novel synchrotron based methods. In experiments such as this being able to enhance the quadrupole transition coupling significantly via SRIXS could open up new possibilities and allow even more accurate determination of electronic structure utilizing the high energy resolution obtainable by SRIXS. Conversely to the discussion by Huotari et al. on the possibility of using their method in high pressure sample environments, SRIXS could be especially useful allowing measurements in dilute samples with weak quadrupole coupling.

Another aspect also briefly discussed by Huotari et al. is the structural geometry and coordination of the material structure around the transition metal centre. In the anti-ferromagnetic NiO a rhombohedral distortion from perfect cubic structure is present under the Néel temperature (523 K) which can also be observed in the pre-edge structure obtained by RIXS [47, 88]. The analysis of X-ray absorption near edge structure (XANES) [87] pre-edge structures along with related transition metal coordination complexes and bulk oxides are discussed more generally by de Groot et al. in [76]. They present a comprehensive guide to the analysis of pre-edge structures in transition metal coordination complexes where different symmetries have different levels of 3d and 4p orbitals mixing leading to variations in the pre-edge structure. For instance, octahedral complexes exhibit only 1s-3d quadrupole transitions, whereas in tetrahedral complexes the metal 3d and 4s states mix locally if the inversion symmetry is broken leading to more a pronounced pre-edge as dipole coupling is also allowed. Bulk transition metal oxides, on the other hand, may behave similarly to coordination complexes when they can be described with a local model, which is the case for divalent oxides, whereas trivalent and tetravalent oxides display non-local orbital mixing in addition to the local mixing. These examples clearly show that the pre-peak structure contains abundant information on the electron structure in the form of different levels of dipole and quadrupole characters. Therefore being able to measure the pre-edge structure more accurately and being able to separate between the dipole and quadrupole characters [48] of the pre-edge even more precisely would be useful in transition metal related research. Traditional RIXS provides useful complementary information to XANES pre-edge structures allowing a more detailed analysis. Stimulated RIXS offers potentially even more resolving power and energy resolution, further, it allows the detection of formerly undetectable quadrupole transitions thus facilitating the separation of dipole and quadrupole characters of the pre-peak.

6. Conclusions

We set out to give a comprehensive and self-contained theoretical introduction to stimulated resonant inelastic X-ray scattering. The goal was to achieve this without any substantial previous knowledge of stimulated RIXS, nonlinear X-ray spectroscopy, or even traditional RIXS, making the present work accessible for anyone the with basic understanding of quantum physics and spectroscopy. The second objective of this work, perhaps for the more advanced reader, was to give an initial nudge in the direction of realizing SRIXS in transition metals with high X-ray energies utilizing quadrupole transitions.

In regards of the first objective the reader was reminded of the basics of many-particle quantum mechanics in the very beginning of this work. A more involved description suitable for representing quantum mechanical states in atoms and molecules, the configuration interaction method, was also presented right after the basics. Next, the matter-radiation interaction was investigated physically and as a result the relevant Hamiltonian describing both the electromagnetic field and matter separately as well as their interaction was derived. In the sense of perturbation theory, the most important result was, of course, the interaction Hamiltonian as it mediates all the processes investigated here. As often in physics, approximations are required here too, thus, the dipole and quadrupole approximations to the interaction Hamiltonian were derived. Following the introductory chapters, the traditional theory describing RIXS was carefully presented and the scattering cross section derived.

We embedded the traditional Kramers-Heisenberg approach with the configuration interaction singles theory interpreting the RIXS process in the light of single particle excitations giving us the same fundamental physical interpretation as used later on in the theoretical considerations of stimulated RIXS. After the theoretical considerations we take a look at the basics of RIXS experiment by first introducing the concept of a RIXS plane visualizing the information obtainable by RIXS followed by an overview of X-ray sources and detectors.

Once the basics and the introduction to RIXS was complete, we moved on to the actual topic: stimulated RIXS. In the beginning of chapter 5 we introduce the basic idea in an intuitive description without any mathematical detail in order to lead the reader, especially one without any previous knowledge of nonlinear spectroscopy, to the subject. We further present several possible pulse schemes that could be used to realize SRIXS experiments including the current state of the art SASE pulses in order to give a depiction of what is possible now and what could be achieved in the future with this method. After the intuitive introduction to SRIXS we proceeded to a detailed derivation of the Maxwell-Liouville-von Neumann equations governing the evolution of both the electromagnetic field and the density matrix elements. This theoretical model is, for the first time, considered up to quadrupole order. The obtained set of equations is not solved within this work since a meaningful solution requires relatively involved computational efforts, rather, this is hoped to act as a foundation to future computational work. Finally we conclude the chapter to an experimental remark, same as the traditional RIXS chapter, but this time we focus more on the problematic nature of the SASE pulses of the current XFELs introducing possible solutions via future development of XFELs and novel data analysis tools. Since quadrupole transitions have not been considered in SRIXS so far, we end with a short view of possible transition metal samples where SRIXS could provide complementary information to X-ray absorption or traditional RIXS.

Considering the goals set for the work in the light of this recap, we can say that it fulfills them. This work assumes only the minimum previous knowledge of the field, yet it delivers a full theoretical description all the way to the cutting edge, even proceeding slightly beyond the previous considerations. Even though mainly theoretical, it also manages to give an overlook on the experimental side on the level any, even the most hardcore, theorist should know. As this work is an introduction to the field, the most advanced theoretically possible applications of SRIXS have not been thoroughly discussed, but rather left on the level of a notion for the interested reader. Future research in the field is offers a wide array of possibilities both theoretically and experimentally. Considering the capabilities of current XFELs even the one dimensional theory offers a variety of experimental possibilities, first and foremost being the experimental detection of stimulated quadrupole transitions in a proof of concept type experiment. Following a successful proof of concept an experiment on a scientifically relevant transition metal sample becomes topical. Theoretically at least the expansion to three dimension is something to look forward in the future, not to dismiss comprehensive computational studies.

A. Quantized Electric and Magnetic Fields

Let us calculate exact representations for the free quantized electric and magnetic fields for a reference. The quantized vector potential describing the electromagnetic field is given by 3.1.17, thus, as shown in the section 3.1, we can calculate the fields as:

$$\begin{aligned}\hat{\boldsymbol{E}}(\boldsymbol{x}) &= -\alpha\frac{\partial}{\partial t}\sum_{\boldsymbol{k},\lambda}\sqrt{\frac{2\pi}{V\omega_{\boldsymbol{k}}\alpha^2}}\left[\hat{a}_{\boldsymbol{k},\lambda}\boldsymbol{\epsilon}_{\boldsymbol{k},\lambda}e^{-i(\omega_{\boldsymbol{k}}t-\boldsymbol{k}\cdot\boldsymbol{x})}+\hat{a}^{\dagger}_{\boldsymbol{k},\lambda}\boldsymbol{\epsilon}^{*}_{\boldsymbol{k},\lambda}e^{i(\omega_{\boldsymbol{k}}t-\boldsymbol{k}\cdot\boldsymbol{x})}\right] \\ &= i\sum_{\boldsymbol{k},\lambda}\sqrt{\frac{2\pi\omega_{\boldsymbol{k}}}{V}}\left[\hat{a}_{\boldsymbol{k},\lambda}\boldsymbol{\epsilon}_{\boldsymbol{k},\lambda}e^{-i(\omega_{\boldsymbol{k}}t-\boldsymbol{k}\cdot\boldsymbol{x})}-\hat{a}^{\dagger}_{\boldsymbol{k},\lambda}\boldsymbol{\epsilon}^{*}_{\boldsymbol{k},\lambda}e^{i(\omega_{\boldsymbol{k}}t-\boldsymbol{k}\cdot\boldsymbol{x})}\right],\end{aligned} \tag{A.0.1}$$

$$\begin{aligned}\hat{\boldsymbol{B}}(\boldsymbol{x}) &= \nabla\times\hat{\boldsymbol{A}}(\boldsymbol{x}) \\ &= i\sum_{\boldsymbol{k},\lambda}\sqrt{\frac{2\pi}{V\omega_{\boldsymbol{k}}\alpha^2}}\left[\hat{a}_{\boldsymbol{k},\lambda}\left(\boldsymbol{k}\times\boldsymbol{\epsilon}_{\boldsymbol{k},\lambda}\right)e^{-i(\omega_{\boldsymbol{k}}t-\boldsymbol{k}\cdot\boldsymbol{x})}-\hat{a}^{\dagger}_{\boldsymbol{k},\lambda}\left(\boldsymbol{k}\times\boldsymbol{\epsilon}^{*}_{\boldsymbol{k},\lambda}\right)e^{i(\omega_{\boldsymbol{k}}t-\boldsymbol{k}\cdot\boldsymbol{x})}\right].\end{aligned} \tag{A.0.2}$$

Note that here we have written the time dependence explicitly.

B. Slowly Varying Envelope Approximation

Slowly varying envelope approximation effectively states that higher order derivatives in the wave equation can be neglected. If ω_0 and $\boldsymbol{k}$ are the frequency and wave vector of the carrier wave for the signal $E(t, \boldsymbol{r})$, we can write the electric field in the standard form:

$$E(t, \boldsymbol{r}) = \mathcal{E}_0(t, \boldsymbol{r}) e^{i(\boldsymbol{k}\cdot\boldsymbol{r} - \omega_0 t)} + \mathcal{E}_0^*(t, \boldsymbol{r}) e^{-i(\boldsymbol{k}\cdot\boldsymbol{r} - \omega_0 t)}. \tag{B.0.1}$$

In the slowly varying envelope approximation one assumes that the complex envelope $\mathcal{E}_0(t, \boldsymbol{r})$ varies slowly in time and space, thus implying:

$$\left|\nabla^2 \mathcal{E}_0(t, \boldsymbol{r})\right| \ll |\boldsymbol{k} \cdot \nabla \mathcal{E}_0(t, \boldsymbol{r})| \quad \text{and} \quad \left|\partial_t^2 \mathcal{E}_0(t, \boldsymbol{r})\right| \ll |\omega_0 \partial_t \mathcal{E}_0(t, \boldsymbol{r})|. \tag{B.0.2}$$

Therefore the wave equation in vacuum (no polarization term) becomes

$$\begin{aligned} \nabla^2 E(t, \boldsymbol{r}) - \frac{1}{c^2} \frac{\partial^2 E(t, \boldsymbol{r})}{\partial t^2} &= 0 \\ (\nabla^2 \mathcal{E}_0) + 2i\boldsymbol{k} \cdot \nabla \mathcal{E}_0 + \frac{1}{c^2} \frac{\partial^2 \mathcal{E}_0(t, \boldsymbol{r})}{\partial t^2} + \frac{2i\omega_0}{c^2} \frac{\partial \mathcal{E}_0}{\partial t} - (k^2 - \frac{\omega_0^2}{c^2}) \mathcal{E}_0 &= 0 \\ \boldsymbol{k} \cdot \nabla \mathcal{E}_0 + \frac{\omega_0}{c^2} \frac{\partial \mathcal{E}_0}{\partial t} &= 0 \end{aligned} \tag{B.0.3}$$

Where we have dropped the second derivatives according to slowly varying envelope approximation and chosen the $\boldsymbol{k}$ and ω_0 to satisfy the dispersion relation:

$$k - \frac{\omega_0}{c} = 0$$

References

1 Nobel prize in physics. https://www.nobelprize.org/prizes/uncategorized/the-nobel-prize-in-physics-1901-2000-2. Accessed: 2020-03-25.

2 European XFEL home page. https://www.xfel.eu/. Accessed: 2020-02-15.

3 FLASH home page. https://flash.desy.de/. Accessed: 2020-02-28.

4 LCLS home page. https://lcls.slac.stanford.edu/. Accessed: 2020-02-28.

5 Victor Kimberg and Nina Rohringer. Stochastic stimulated electronic x-ray raman spectroscopy. *Structural Dynamics*, 3(3):034101, 2016.

6 Nina Rohringer. X-ray raman scattering: a building block for nonlinear spectroscopy. *Philosophical Transactions of the Royal Society A: Mathematical, Physical and Engineering Sciences*, 377(2145):20170471, 2019.

7 Wolfgang Demtröder. *Laser Spectroscopy 2: Experimental Techniques*. Springer Berlin Heidelberg, Berlin, Heidelberg, 2015.

8 Lin X. Chen. Probing transient molecular structures in photochemical processes using laser-initiated time-resolved x-ray absorption spectroscopy. *Annual Review of Physical Chemistry*, 56(1):221–254, 2005. PMID: 15796701.

9 Ch. Bressler et al. Femtosecond xanes study of the light-induced spin crossover dynamics in an iron(ii) complex. *Science*, 323(5913):489–492, 2009.

10 Wenkai Zhang et al. Tracking excited-state charge and spin dynamics in iron coordination complexes. *Nature*, 509(7500):345–348, 2014.

11 Ph. Wernet et al. Orbital-specific mapping of the ligand exchange dynamics of fe(co)5 in solution. *Nature*, 520(7545):78–81, 2015.

12 M. Beye, Ph. Wernet, C. Schüßler-Langeheine, and A. Föhlisch. Time resolved resonant inelastic x-ray scattering: A supreme tool to understand dynamics in solids and molecules. *Journal of Electron Spectroscopy and Related Phenomena*, 188:172 – 182, 2013. Progress in Resonant Inelastic X-Ray Scattering.

13 A. Pietzsch et al. Towards time resolved core level photoelectron spectroscopy with femtosecond x-ray free-electron lasers. *New Journal of Physics*, 10(3):033004, mar 2008.

14 B. K. McFarland et al. Ultrafast x-ray auger probing of photoexcited molecular dynamics. *Nature Communications*, 5(1):4235, 2014.

15 Luuk J. P. Ament et al. Resonant inelastic x-ray scattering studies of elementary excitations. *Rev. Mod. Phys.*, 83:705–767, Jun 2011.

16 Akio Kotani and Shik Shin. Resonant inelastic x-ray scattering spectra for electrons in solids. *Rev. Mod. Phys.*, 73:203–246, Feb 2001.

17 Pieter Glatzel and Uwe Bergmann. High resolution 1s core hole x-ray spectroscopy in 3d transition metal complexes—electronic and structural information. *Coordination Chemistry Reviews*, 249(1):65 – 95, 2005. Synchrotron Radiation in Inorganic and Bioinorganic Chemistry.

18 Faris Gel'mukhanov and Hans Ågren. Resonant x-ray raman scattering. *Physics Reports*, 312(3):87 – 330, 1999.

19 Igor V. Schweigert and Shaul Mukamel. Probing valence electronic wave-packet dynamics by all x-ray stimulated raman spectroscopy: A simulation study. *Phys. Rev. A*, 76:012504, Jul 2007.

20 Yu Zhang, Jason D. Biggs, Niranjan Govind, and Shaul Mukamel. Monitoring long-range electron transfer pathways in proteins by stimulated attosecond broadband x-ray raman spectroscopy. *The Journal of Physical Chemistry Letters*, 5(21):3656–3661, 2014. PMID: 25400875.

21 Daniel Healion et al. Entangled valence electron–hole dynamics revealed by stimulated attosecond x-ray raman scattering. *The Journal of Physical Chemistry Letters*, 3(17):2326–2331, 2012. PMID: 23755318.

22 Markus Kowalewski, Kochise Bennett, Konstantin E. Dorfman, and Shaul Mukamel. Catching conical intersections in the act: Monitoring transient electronic coherences by attosecond stimulated x-ray raman signals. *Phys. Rev. Lett.*, 115:193003, Nov 2015.

23 Clemens Weninger et al. Stimulated electronic x-ray raman scattering. *Phys. Rev. Lett.*, 111:233902, Dec 2013.

24 N. Rohringer et al. *X-Ray Lasers 2014: Proceedings of the 14th International Conference on X-Ray Lasers*, volume 169. 01 2016.

25 Thomas Kroll et al. Stimulated x-ray emission spectroscopy in transition metal complexes. *Phys. Rev. Lett.*, 120:133203, Mar 2018.

26 J.J. Sakurai. *Advanced Quantum Mechanics*. Always learning. Pearson Education, Incorporated, 1967.

27 A.L. Fetter and J.D. Walecka. *Quantum Theory of Many-particle Systems*. Dover Books on Physics. Dover Publications, 2003.

28 C. David Sherrill and Henry F. Schaefer. The configuration interaction method: Advances in highly correlated approaches. volume 34 of *Advances in Quantum Chemistry*, pages 143 – 269. Academic Press, 1999.

29 Attila Szabo and Neil S. Ostlund. *Modern Quantum Chemistry: Introduction to Advanced Electronic Structure Theory*. Dover Publications, Inc., first edition, 1996.

30 L.I. Schiff. *Quantum Mechanics*. International series in pure and applied physics. McGraw-Hill, 1955.

31 Robin Santra. Concepts in x-ray physics. *Journal of Physics B: Atomic, Molecular and Optical Physics*, 42(2):023–001, Dec 2008.

32 J. D. Jackson. From lorenz to coulomb and other explicit gauge transformations. *American Journal of Physics*, 70(9):917–928, 2002.

33 Gregory S. Adkins. Feynman rules of coulomb-gauge qed and the electron magnetic moment. *Phys. Rev. D*, 36:1929–1932, Sep 1987.

34 Winfried Schülke. *Electron Dynamics by Inelastic X-Ray Scattering*. Oxford University Press, Jan 2007.

35 Nina Rohringer. Introduction to the theory of x-ray matter interaction, 2018.

36 S L Prunty. A primer on the theory of thomson scattering for high-temperature fusion plasmas. *Physica Scripta*, 89(12):128001, nov 2014.

37 Joseph Berkowitz. 1 - introduction. In Joseph Berkowitz, editor, *Atomic and Molecular Photoabsorption*, pages 1 – 7. Academic Press, London, 2002.

38 J.P. Glusker, M. Lewis, and M. Rossi. *Crystal structure analysis for chemists and biologists*. Methods in stereochemical analysis. VCH, 1994.

39 Marlan O. Scully and M. Suhail Zubairy. *Quantum Optics*. Cambridge University Press, 1997.

40 P. A. M. Dirac. *The Principles of Quantum Mechanics*. Clarendon Press, 1930.

41 L. Schwartz. Sur l'impossibilité de la multiplications des distributions. *C. R. Acad. Sci.*, 239:847–848, 1954.

42 James D Bjorken and Sidney David Drell. *Relativistic quantum mechanics*. International series in pure and applied physics. McGraw-Hill, New York, NY, 1964.

43 Karl Blum. *Density matrix theory and applications; 3rd ed.* Springer Series on Atomic Optical and Plasma Physics. Springer, Berlin, 2012.

44 Pieter Glatzel, Marcin Sikora, and Marcos Fernández-García. Resonant x-ray spectroscopy to study k absorption pre-edges in 3d transition metal compounds. *Eur. Phys. J. Special Topics*, 169:207–214, 03 2009.

45 P. Eisenberger, P. M. Platzman, and H. Winick. X-ray resonant raman scattering: Observation of characteristic radiation narrower than the lifetime width. *Phys. Rev. Lett.*, 36:623–626, Mar 1976.

46 P. Bunker. *Molecular Symmetry and Spectroscopy*. Elsevier Science, 2012.

47 Simo Huotari, Tuomas Pylkkänen, György Vankó, Roberto Verbeni, Pieter Glatzel, and Giulio Monaco. Crystal-field excitations in nio studied with hard x-ray resonant inelastic x-ray scattering at the nik

edge. *Physical Review B, Condensed Matter and Materials Physics*, 78(4):041102(R), 7 2008.

48 G. Dräger, R. Frahm, G. Materlik, and O. Brümmer. On the multipole character of the x-ray transitions in the pre-edge structure of fe k absorption spectra. an experimental study. *physica status solidi (b)*, 146(1):287–294, 1988.

49 Pieter Glatzel, Uwe Bergmann, Junko Yano, Hendrik Visser, John H. Robblee, Weiwei Gu, Frank M. F. de Groot, George Christou, Vincent L. Pecoraro, Stephen P. Cramer, and Vittal K. Yachandra. The electronic structure of mn in oxides, coordination complexes, and the oxygen-evolving complex of photosystem ii studied by resonant inelastic x-ray scattering. *Journal of the American Chemical Society*, 126(32):9946–9959, Aug 2004.

50 Yutian Li and R. Wong. Integral and series representations of the dirac delta function. *Communications on Pure and Applied Analysis*, 7:229–247, 03 2008.

51 Anatoly Shabalin. *Coherent X-ray diffraction studies of mesoscopic materials*. PhD thesis, 02 2016.

52 Deutsches elektronen-synchrotron (DESY) home page. http://www.desy.de/. Accessed: 2020-02-15.

53 J Feldhaus, J Arthur, and J B Hastings. X-ray free-electron lasers. *Journal of Physics B: Atomic, Molecular and Optical Physics*, 38(9):S799–S819, apr 2005.

54 Claudio Pellegrini and Joachim Stöhr. X-ray free-electron lasers—principles, properties and applications. *Nuclear Instruments*

and Methods in Physics Research Section A: Accelerators, Spectrometers, Detectors and Associated Equipment, 500(1):33 – 40, 2003. NIMA Vol 500.

55 N.B. Brookes et al. The beamline id32 at the esrf for soft x-ray high energy resolution resonant inelastic x-ray scattering and polarisation dependent x-ray absorption spectroscopy. *Nuclear Instruments and Methods in Physics Research Section A: Accelerators, Spectrometers, Detectors and Associated Equipment*, 903:175 – 192, 2018.

56 M. Moretti Sala et al. A high-energy-resolution resonant inelastic X-ray scattering spectrometer at ID20 of the European Synchrotron Radiation Facility. *J Synchrotron Radiat*, 25(Pt 2):580–591, Mar 2018.

57 T. H. MAIMAN. Stimulated optical radiation in ruby. *Nature*, 187(4736):493–494, August 1960.

58 Nina Rohringer et al. Atomic inner-shell x-ray laser at 1.46 nanometres pumped by an x-ray free-electron laser. *Nature*, 481(7382):488–491, 2012.

59 Nina Rohringer and Richard London. Atomic inner-shell x-ray laser pumped by an x-ray free-electron laser. *Phys. Rev. A*, 80:013809, Jul 2009.

60 Victor Kimberg, Song Bin Zhang, and Nina Rohringer. X-ray lasing in the CO molecule. *Journal of Physics B: Atomic, Molecular and Optical Physics*, 46(16):164017, aug 2013.

61 Robert W. Boyd. *Nonlinear Optics, Third Edition*. Academic Press, Inc., USA, 3rd edition, 2008.

62 R. Soto and Oxford University Press. *Kinetic Theory and Transport Phenomena*. Oxford master series in condensed matter physics. Oxford University Press, 2016.

63 Victor Kimberg et al. *Faraday Discuss.*, 194:305–324, 2016.

64 M. G. Raymer and J. Mostowski. Stimulated raman scattering: Unified treatment of spontaneous initiation and spatial propagation. *Phys. Rev. A*, 24:1980–1993, Oct 1981.

65 O. Larroche, D. Ros, A. Klisnick, A. Sureau, C. Möller, and H. Guennou. Maxwell-bloch modeling of x-ray-laser-signal buildup in single- and double-pass configurations. *Phys. Rev. A*, 62:043815, Sep 2000.

66 Chul Min Kim, Karol A. Janulewicz, and Jongmin Lee. Pulse buildup from noise and intrinsic polarization of plasma-based x-ray lasers. *Phys. Rev. A*, 84:013834, Jul 2011.

67 Yu-Ping Sun, Ji-Cai Liu, Chuan-Kui Wang, and Faris Gel'mukhanov. Propagation of a strong x-ray pulse: Pulse compression, stimulated raman scattering, amplified spontaneous emission, lasing without inversion, and four-wave mixing. *Phys. Rev. A*, 81:013812, Jan 2010.

68 Jhih-An You, Jan Marcus Dahlström, and Nina Rohringer. Attosecond dynamics of light-induced resonant hole transfer in high-order-harmonic generation. *Phys. Rev. A*, 95:023409, Feb 2017.

69 Clemens Weninger and Nina Rohringer. Stimulated resonant x-ray raman scattering with incoherent radiation. *Phys. Rev. A*, 88:053421, Nov 2013.

70 Nina Rohringer and Robin Santra. Strongly driven resonant auger

effect treated by an open-quantum-system approach. *Phys. Rev. A*, 86:043434, Oct 2012.

71 John David Jackson. *Classical electrodynamics*. Wiley, New York, NY, 3rd ed. edition, 1999.

72 Nina Rohringer and Robin Santra. Multichannel coherence in strong-field ionization. *Phys. Rev. A*, 79:053402, May 2009.

73 Victor Kimberg and Nina Rohringer. Amplified x-ray emission from core-ionized diatomic molecules. *Phys. Rev. Lett.*, 110:043901, Jan 2013.

74 Nina Rohringer, Ariel Gordon, and Robin Santra. Configuration-interaction-based time-dependent orbital approach for ab initio treatment of electronic dynamics in a strong optical laser field. *Phys. Rev. A*, 74:043420, Oct 2006.

75 Takeshi Sato, Takuma Teramura, and Kenichi L. Ishikawa. Gauge-invariant formulation of time-dependent configuration interaction singles method. *Applied Sciences*, 8(3), 2018.

76 Frank de Groot, György Vankó, and Pieter Glatzel. The 1s x-ray absorption pre-edge structures in transition metal oxides. *Journal of Physics: Condensed Matter*, 21(10):104207, feb 2009.

77 Jani Lukkarinen and Herbert Spohn. Not to normal order—notes on the kinetic limit for weakly interacting quantum fluids. *Journal of Statistical Physics*, 134(5-6):1133–1172, Feb 2009.

78 S. Krinsky and R. L. Gluckstern. Analysis of statistical correlations and intensity spiking in the self-amplified spontaneous-emission free-electron laser. *Phys. Rev. ST Accel. Beams*, 6:050701, May 2003.

79 A. Singer, U. Lorenz, F. Sorgenfrei, N. Gerasimova, J. Gulden, O. M. Yefanov, R. P. Kurta, A. Shabalin, R. Dronyak, R. Treusch, V. Kocharyan, E. Weckert, W. Wurth, and I. A. Vartanyants. Hanbury brown–twiss interferometry at a free-electron laser. *Phys. Rev. Lett.*, 111:034802, Jul 2013.

80 E. Roussel et al. Multicolor high-gain free-electron laser driven by seeded microbunching instability. *Phys. Rev. Lett.*, 115:214801, Nov 2015.

81 David Gauthier et al. Generation of phase-locked pulses from a seeded free-electron laser. *Phys. Rev. Lett.*, 116:024801, Jan 2016.

82 Gianluca Geloni. *Self-Seeded Free-Electron Lasers*, pages 161–193. Springer International Publishing, Cham, 2016.

83 A. Marinelli et al. High-intensity double-pulse x-ray free-electron laser. *Nature Communications*, 6(1):6369, 2015.

84 Alberto A. Lutman et al. High-power femtosecond soft x rays from fresh-slice multistage free-electron lasers. *Phys. Rev. Lett.*, 120:264801, Jun 2018.

85 Svitozar Serkez. Self-seeding xfels: Operation principle and challenges. *Synchrotron Radiation News*, 29(3):10–14, 2016.

86 L. J. FRASINSKI, K. CODLING, and P. A. HATHERLY. Covariance mapping: A correlation method applied to multiphoton multiple ionization. *Science*, 246(4933):1029–1031, 1989.

87 F. de Groot and A. Kotani. *Core Level Spectroscopy of Solids*. Advances in Condensed Matter Science. CRC Press, 2008.

88 T. Eto, S. Endo, M. Imai, Y. Katayama, and T. Kikegawa. Crystal structure of nio under high pressure. *Phys. Rev. B*, 61:14984–14988, Jun 2000.